UNVEILING THE SUBAQUEOUS SPECTACLE OF

DYNAMIC TURBIDITY CURRENT – MINIBASIN INTERACTIONS

AN ABSTRACT

SUBMITTED ON THE TWENTY-SECOND OF JULY 2O24

TO THE DEPARTMENT OF EARTH AND ENVIRONMENTAL SCIENCES

IN PARTIAL FULLFILMENT OF THE REQUIREMENTS

OF THE SCHOOL OF SCIENCE AND ENGINEERING

OF TULANE UNIVERSITY

FOR THE DEGREE

OF

DOCTOR OF PHILOSOPHY

BY

J. Kevin Reece

APPROVED: ______________________

Kyle M. Straub, PhD
Director

____

Cynthia J. Ebinger, PhD

Mead Allison Digitally signed by Mead Allison Date: 2024.07.25 11:04:42

____

Mead A. Allison, PhD

____

Robert M. Dorrell, PhD

ABSTRACT

Minibasins, large seafloor depressions that develop on mobile substrates, significantly impact turbidity current dynamics and serve as repositories of Earth's history and geofluid reservoirs. Field-scale studies are limited due to their remote locations and the sporadic occurrence of turbidity currents, making experimentation essential for advancing our understanding. This thesis quantifies interactions between turbidity currents and minibasins, emphasizing the need to characterize internal flow dynamics in three dimensions, and the geometric scales and nested complexity of minibasins. To accomplish this, I characterize both the statistics of minibasin bathymetry in a salt province at the regional margin scale and quantify turbidity current interactions at the basin spatial scale through three-dimensional, 3-D, physical experimentation. Findings include that hydraulically ponded turbidity currents circulate with both a vertical and horizontal component and that the strength and style of circulation is a function of the influx of flow to a minibasin. The influx rate controls the run-up height of a flow onto the distal slope and establishes the concentration of sediment that enters circulation cells, which is subsequently distributed basin wide. This run-up also controls the height that sediment onlaps against minibasin side walls. Circulation cells feature an upwelling component at their core that reduces the trapping efficiency of minibasins and directly impacts the capture of particles with low settling velocities. This 3-D experimental campaign highlights distinctions from theory developed from 2-D experiments, which include a reduced sediment trapping capacity of minibasins, extended time required to achieve flow equilibrium conditions, and a strong 3-D topographic influence on internal turbidity current structure. Results suggests that minibasin filling deposits have greater heterogeneity than suggested in prior 2-D studies, which impacts our interpretation of the quality of geofluid reservoirs they house and influences the interpretation of their stratigraphic records. Results also suggest that minibasins on the upper continental slope are less efficient at storing particulate organic carbon and microplastics than previously thought. The regional analysis reveals that the thickness of a salt substrate is a major factor controlling the spatial density of minibasins on the seafloor and the complexity of minibasins. Self-organization of the seafloor, through depression development, is quantified by Pareto power-law parameters that characterize the distribution of minibasin spatial scales. Results of this analysis include enhanced weight in the tails of distributions describing depressions geometries over regions of thick salt substrates, which suggest enhanced self-organization of depressions.

UNVEILING THE SUBAQUEOUS SPECTACLE OF

DYNAMIC TURBIDITY CURRENT – MINIBASIN INTERACTIONS

A DISSERTATION

SUBMITTED ON THE TWENTY-SECOND OF JULY 2O24

TO THE DEPARTMENT OF EARTH AND ENVIRONMENTAL SCIENCES

IN PARTIAL FULLFILMENT OF THE REQUIREMENTS

OF THE SCHOOL OF SCIENCE AND ENGINEERING

OF TULANE UNIVERSITY

FOR THE DEGREE

OF

DOCTOR OF PHILOSOPHY

BY

J. Kevin Reece

APPROVED:

Kyle M. Straub, PhD
Director

Cynthia J. Ebinger, PhD

Mead Allison Digitally signed by Mead Allison Date: 2024.07.25 11:05:10 -04'00'

Mead A. Allison, PhD

Robert M. Dorrell, PhD

ACKNOWLEDGEMENTS

I extend my deepest gratitude to my Ph.D. advisor, Dr. Kyle M. Straub, whose unwavering guidance and boundless knowledge have been instrumental throughout my tenure at Tulane University. His mentorship in the Tulane Sediment Dynamics and Quantitative Stratigraphy Group has profoundly shaped my scientific journey. I am also indebted to my esteemed committee members, whose invaluable insights and constructive feedback have played a pivotal role in my development as a scientist. To my father, what a hell of a ride! I wouldn't have accomplished this endeavor without your continued support. This scientific journey will forever play a large part in shaping who I have yet to become, and this dissertation is dedicated to the women that I love: Emilia, Lynsey, and Myra.

TABLE OF CONTENTS

LIST OF TABLES

CHAPTER 3

CHAPTER 4

LIST OF FIGURES

CHAPTER 1

CHAPTER 2

CHAPTER 3

CHAPTER 4

CHAPTER 1

INTRODUCTION

Large seafloor depressions, often termed 'minibasins' [*Hudec et al.*, 2013], can have geometric scales sufficient to impact the depositional mechanics of sediment-laden density currents termed turbidity currents [*Menard Jr*, 1955; *Nasr-Azadani and Meiburg*, 2014] (Fig. 1), which are the principal sediment transport phenomena in deep marine environments [*Middleton*, 1993; *Piper and Normark*, 2009]. Turbidity currents were first discovered from their linkage to seabed infrastructure damage after a series of earthquakes in the early 20th century [*Heezen and Ewing*, 1952]. More recently, turbidity currents have been noted to play a vital role in Earth's organic carbon cycle [*Talling et al.*, 2024] and the transport of pollutants (e.g., microplastics) [*Kane and Clare*, 2019], both of which are impacted by turbidity current interactions with enclosed depressions, given that topographic features are shown to impact fluid flow and sediment transport fields [*Reece et al.*, 2024] (Fig. 1). Minibasins are large topographic depressions that have depths comparable, or in excess to, the thickness of turbidity currents, and have long been recognized as valuable repositories of Earth's history [*Hudec et al.*, 2009] and volumetrically substantial geofluid reservoirs [*Losh et al.*, 2002; *Prather et al.*, 2012; *Stricker et al.*, 2018]. Minibasins, which have a range of shapes, typically occur on passive continental margins with mobile substrates of salt or uncompacted shale [*Hudec and Jackson*, 2007; *Soto et al.*, 2021], and can trap and induce deposition from turbidity currents [*Ge et al.*, 2021; *Hudec et al.*, 2009; *Lamb et al.*, 2006] (Fig. 1). It is speculated that on slopes greater than 0.6°, turbidity currents often move as densimetric Froude supercritical ($Fr_D > 1$) flows, where inertial forces dominate over gravitational forces and sediment tends to be kept in suspension [*Hand*, 1974; *Komar*, 1971; *Sequeiros*, 2012; *Talling et al.*, 2015]. When transitioning to lower slopes or encountering adverse slopes (e.g., minibasins), it is hypothesized that flows transition to densimetric Froude subcritical ($Fr_D < 1$) and sediment tends to settle out of the flow [*Lamb et al.*, 2006]. The deposits of turbidity currents are termed turbidites [*Bouma*, 1964]. Hence, a correlation can be established between the geometry of turbidites contained within large depressions and the way turbidity currents interact with these specific confining topographic features. The definition of 'large' depressions introduces ambiguity, necessitating an exploration into the distribution of seafloor depression scales relative to the size of turbidity currents. Quantifying these depressions will also aid characterization of the accommodation available to store sediment on gravitationally active margins. For example, quantifying if most accommodation resides in many small depressions or in a few large depressions on a margin.

Amidst the changing dynamics of marine environments, it is important to highlight the growing global practice of sand mining [*Byrnes et al.*, 2004], which is possibly altering the frequency and size of turbidity currents. With sand mining activities increasing worldwide [*Gavriletea*, 2017], we expect marine landscapes to experience an increased frequency of turbidity current events. These changes have widespread consequences for sediment deposition patterns in deep marine environments, particularly affecting the transport of organic carbon and pollutants such as microplastics [*Pohl et al.*, 2020; *Talling et al.*, 2024]. As sand mining operations expand globally, it is imperative for the global community to evaluate the environmental impacts of sediment transport systems (e.g., turbidity currents and minibasins) to marine ecosystems [*Drazen et al.*, 2020]. Understanding the interactions between turbidity currents, minibasins, and sand mining sheds light on potential threats to marine ecosystems, highlighting the urgent need for global adoption of environmental management strategies for sand mining practices [*Leal Filho et al.*, 2021].

Minibasins are efficient sediment traps primarily because they can cause turbidity currents to collapse or hydraulically pond (Fig. 1). The latter process initiates when flows reflect off counter topographic slopes [*Dorrell et al.*, 2018; *Patacci et al.*, 2015; *Toniolo et al.*, 2007]. This can lead to a rapid spatial deceleration of flow to exceedingly low densimetric Froude conditions and the development of a placid flow interface with the overlying ambient fluid [*Dorrell et al.*, 2018; *Lamb et al.*, 2004; *Toniolo et al.*, 2006b; *Violet et al.*, 2005]. In 2-D experiments, this ponding process results in concentration profiles with limited stratification, which exists below a return flow. This flow structure results in tabular deposits that show limited thinning onto confining slopes [*Lamb et al.*, 2004; *Toniolo et al.*, 2006a]. Notably, 2-D minibasin experimental studies describe flow circulation patterns along a vertical plane, with a potential return flow positioned above the primary flow, which is directed down-margin [*Patacci et al.*, 2015]. The presence of circulation in 3-D minibasins remains uncertain, despite its potential implications for near-bed shear stress, sediment transport capacity, deposit heterogeneity, and ultimately minibasin sediment trapping potential, particularly for particulates with low settling velocities (i.e., organic carbon and microplastics).

Our understanding of field-scale turbidity current flow structure within minibasins remains limited due to the challenges presented by their remote and inaccessible locations, sporadic occurrences, and high flow shear stresses that can lead to monitoring equipment destruction (e.g., multibeam sonar, optical backscatter sensors, acoustic monitoring transponders, sediment traps, etc.) [*Clare et al.*, 2020; *Rotzien et al.*, 2022; *Talling et al.*, 2022]. Consequently, many advancements in our understanding of turbidity currents interacting with minibasins rely heavily on numerical and physical experimentation [*Bastianon*, 2018; *Bastianon et al.*, 2021; *Khan and Imran*, 2008; *Lamb et al.*, 2006; *Patacci et al.*, 2015; *Toniolo et al.*, 2006b; *Violet et al.*, 2005]. Many numerical models employ depth-average formulations to describe turbidity currents, mitigating the considerable computational resources needed to accurately simulate the extensive fluid and sediment transport fields [*Wahab et al.*, 2022]. These, depth average models are sometimes suitable for unconfined settings but have reduced predictive capacity in scenarios where vertical flow structure varies strongly in space and time, such as in minibasins [*Bastianon et al.*, 2021] (Fig. 1). Insights from 2-D flume experiments suggest a significant influence of minibasins on the fluid and sediment transport fields of turbidity currents [*Lamb et al.*, 2006; *Patacci et al.*, 2015; *Toniolo et al.*, 2006b]. While much can be learned from 2-D experiments, the intricate three-dimensional structure of minibasins necessitates some 3-D experimentation into flow processes within minibasins [*Patacci et al.*, 2015]. Some prior 3-D experimental exploration of turbidity current – minibasin interactions has occurred, these prior experiments had side wall slopes significantly greater than field systems and/or collected limited flow data to tie to deposit structure [*Maharaj*, 2012; *Violet et al.*, 2005]. Further, many prior physical experiments used quartz particles with grain sizes that are challenging to keep in suspension at laboratory scales [*Janocko et al.*, 2013; *Middleton*, 1993; *Sequeiros et al.*, 2009].

The focus of this thesis is on characterizing the size and shape of minibasins on gravity influenced margins and the quantification of turbidity current interactions with these depressions (Fig. 1). I seek to characterize turbidity current flow circulation within 3-D minibasins of varying planform shapes, with implications for the fluid and sediment transport fields, offering a new perspective beyond the insights from 2-D experimental observations. Specifically, results from a 3-D experimental campaign are compared to 2-D experiments to test earlier developed theory on how flows circulate in minibasins, the trapping potential of these depressions, time necessary to reach equilibrium flow conditions in these depressions, and the influence of minibasin shape on these interactions (Fig. 1). An additional component of this thesis explores the regional scale statistics of accommodation derived from salt diapirism on a passive continental margin in the northern Gulf of Mexico (GoM). This region was selected due to its widespread active salt tectonics and associated minibasins. A geospatial analysis and correlation to subsurface salt volumes allows distributions of total ponded accommodation scales and minibasin nested complexity to be generated. Variations in statistics of minibasin scales are found between subregions of the northern GoM and are attributed to thicknesses of the underlying mobile substrate, the Louann Salt. This unit has an average base of salt at 16 km below sea level [*Andrews*, 1960; *Hudec et al.*, 2013]. Further, a link between minibasin self-organization, based on characteristics of the distributions [*Colling et al.*, 2001], and the thickness of the Louann Salt is presented.

This thesis is composed of four chapters, three of which (Chapters 2-4) detailed hereafter, are written to delve into specifics and provide quantifiable results that span the scales over which turbidity currents interact with minibasins.

Chapter 2 "Circulation of hydraulically ponded turbidity currents and the filling of continental slope minibasins" unravels the influence of flow discharge into 3-D minibasins on the three-component velocity field, sediment concentration field, and resulting shapes of turbidites. To overcome previous scaling challenges encountered in laboratory settings, a novel experimental sediment mixture was developed. This mixture, consisting of higher density aluminum oxide and a deflocculant, addresses issues such as sediment suspension problems caused by flocculation of previously used silica-based sediments with relatively lower densities. The new sediment mixture reduces high rates of sediment deposition on proximal slopes upon flow entry into experimental minibasins by increasing the gravitational driving force of low volumetric concentration flows, while also keeping grain flocculation of fine-grained particles to a minimum. As a result, the aluminum oxide sediment mixture drives flows further into the experimental minibasins, from flows that have sediment concentrations comparable to those observed in natural systems. Here, the experimental setup uses circular minibasins with side wall slopes that fall within the field scale spectrum. Flow discharge is controlled by manipulating input flow width while keeping all other parameters constant, including flow height and mean influx velocity. This approach allows for minibasins to fully trap or partially confine flows, and as such spans the fill-to-strip-to-spill transition [*Badalini et al.*, 2000; *Beaubouef and Abreu*, 2006; *Beaubouef and Friedmann*, 2000; *Satterfield and Behrens*, 1990]. I quantify horizontal circulation cells, which are identified as the primary mechanism that distributes sediment throughout enclosed minibasins (Fig. 1). These circulation cells produce flow upwelling that can counteract the still fluid settling velocity of suspended sediment to the basin floor (Fig. 1). Thus, the magnitude of this upwelling relative to the still fluid sediment fall velocity impacts the trapping of particulates. I highlight that particulates with relatively low settling velocities, such as particulate organic carbon and microplastics, can therefore be preferentially expelled from minibasins by the upwelling flow.

Chapter 3 "Quantifying the interaction of turbidity currents with enclosed minibasin topography in three dimensions: A laboratory study" explores in more detail the complex interactions of turbidity currents with enclosed three-dimensional topography. Mobile substrates (e.g., uncompacted shales and salt) are the consequence of gravitational loading in sedimentary basins and have the potential for ductile deformation over geological timescales, generating depressions of a variety of scales [*Cohen and Hardy*, 1996; *Wiener et al.*, 2011]. Some of these depressions have dimensions substantial enough to influence the depositional mechanics of turbidity currents [*Dorrell et al.*, 2018; *Kneller and Buckee*, 2000; *Kneller and McCaffrey*, 1993; *Kneller and McCaffrey*, 1999; *Maharaj*, 2012]. This chapter details experimental results from a laboratory study that examines how changes in turbidity current influx and minibasin topographic basin aspect ratio influence the depositional mechanics of turbidity currents. Observations of flow conditions throughout minibasins, including flow evolution to equilibrium conditions and the time to reach this equilibrium, are covered (Fig. 1). When compared to results from prior 2-D studies, this chapter highlights: 1) a reduced minibasin sediment trapping capacity, 2) an extended time required for the system to reach equilibrium conditions, and 3) that minibasin planform aspect ratios impact the internal turbidity current structure, with near bed shear stress decreasing as minibasin length to width increases.

Chapter 4 "Quantifying the statistical organization of ponded accommodation resulting from salt dynamics along the northern Gulf of Mexico passive continental margin" provides a statistical analysis of a regional topographic response to underlying salt tectonics. Specifically, the chapter focuses on the quantification of distributions of minibasin spatial scales that indicate a varying degree of self-organization as a function of the thickness of the underlying mobile substrate. Further, I describe nested depressions that add topographic complexity to the seafloor and produce accommodation to store sediment. The amount of ponded accommodation, or space lying within three-dimensionally closed topographic lows on continental slopes is presented for the entire northern GoM margin. Distributions of geometric scale parameters are also constructed for subregions of the margin based upon seafloor surface drainage patterns [*Steffens et al.*, 2003]. These patterns are anticipated to correlate with thickness and depths of the Louann Salt, indicating differences in the self-organization of bathymetry. Further, this work quantifies a correlation between minibasin geometric size and nested complexity. This is done by leveraging variables that describe the power-law distribution of geometric parameters, including the distribution tail index (α). We find that tail indexes of depression relief, planar diameter, area, volume, and nested complexity inversely scale with the thickness of salt beneath subregions of the northern GoM, suggesting greater self-organization of bathymetry in regions underlain by thick salt deposits. Louann Salt thickness varies along strike of the continental slope with maximum salt thicknesses exceeding 4 km in the northern GoM's minibasin province, while significantly decreasing in salt thickness along the flanks of the minibasins province to less than 0.5 km of thickness before pinching out onto the Florida escarpment and Texas continental shelf [*Diegel et al.*, 1995; *Ko*, 2014]. Results show that much of the ponded accommodation in the northern GoM resides in relatively few large depressions that are of scale necessary to induce hydraulic ponding or the collapse of flows and can therefore enhance the trapping of sediment. This sediment trapping can then further drive salt evacuation until minibasins weld. This process of minibasins trapping turbidity currents, inducing sediment deposition, and subsiding into mobile salt substrates, influences the evolution of the northern GoM margin through time and the construction of substantial geofluid reservoirs.

LIST OF FIGURES

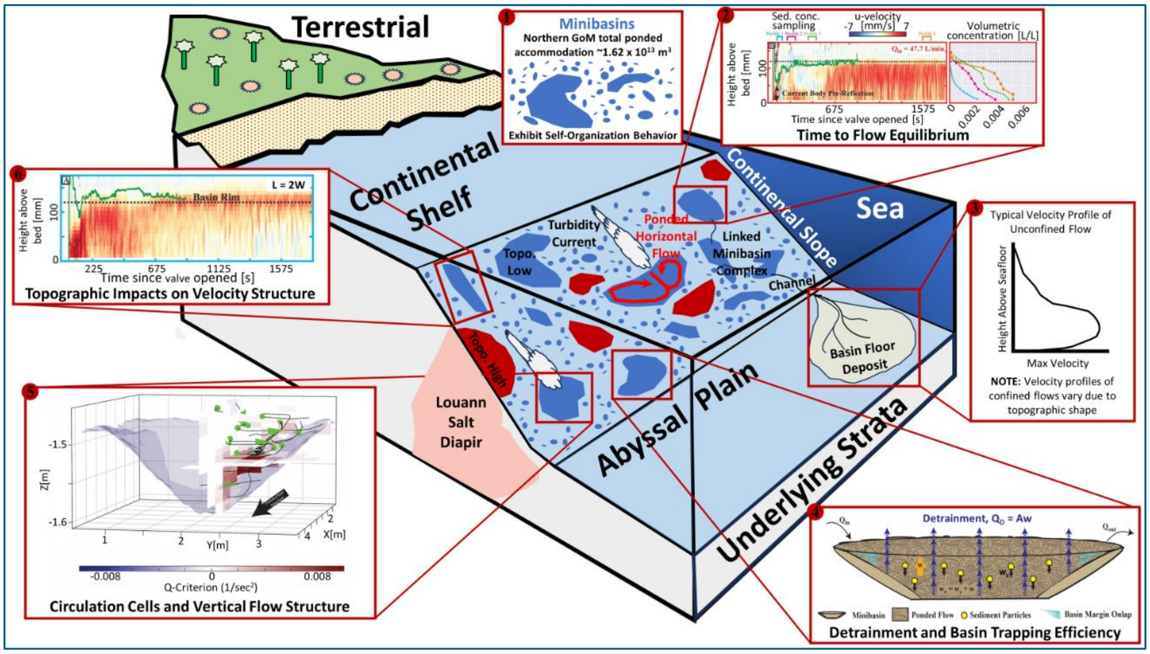

Figure 1. Schematic visualizing core concepts of minibasins, turbidity current flow, and sediment transport processes as a function of confined (i.e., minibasins) and unconfined (i.e., basin floor fan deposits) topography. Sub-panels include: 1) Minibasins – statistical analyses find total ponded accommodation and self-organization behavior in the northern GoM. 2) Time to Flow Equilibrium – time to reach flow equilibrium is far longer than previously theorized based upon experimental basin center conditions of u-velocity and sediment concentration profiles. 3) Velocity Profile of Unconfined Flow – unconstrained turbidity current flows have a typical u-velocity profile having maximum velocities approximately 1/3 the height of the flow above the bed. 4) Detrainment and Basin Trapping Efficiency – experimental results suggest that detrainment plays an important role in minibasins trapping efficiencies due to its limiting effect on sediment settling velocities to the bed, 5) Circulation Cells and Vertical Flow Structure – experimental results identify for the first time a vortical flow structure within ponded minibasins that distribute sediment throughout the minibasins and onto its sidewalls, with an upwelling velocity component much greater than sediment fall velocities to the bed, and 6) Topographic Impacts on Velocity Structure – experimental results capture unique changes in velocity profiles and shear along the bed as a function of a minibasin's planar geometry.

LIST OF REFERENCES

Andrews, D. (1960). The Louann Salt and its relationship to Gulf Coast salt domes, *Gulf Coast Association of Geological Societies Transactions*, **10**(1), 215-240.

Badalini, G., B. Kneller, and C. Winker (2000). Architecture and Processes in the Late Pleistocene Brazos-Trinity Turbidite System, Gulf of Mexico Continental Slope, *GCSSEPM, 20th Annual Research Conference Deep-Water Reservoirs of the World*, 16-34.

Bastianon, E. (2018). Numerical Modeling of Submarine Minibasin Flow and Morphodynamics, Ph.D. thesis, 152 pp., University of South Carolina, Columbia, South Carolina, USA.

Bastianon, E., E. Viparelli, A. Cantelli, and J. Imran (2021). 2D numerical simulation of the filling process of submarine minibasins: Study of deposit architecture, *Journal of Sedimentary Research*, ***91***(4), 399-414.

Beaubouef, R., and V. Abreu (2006). Basin 4 of the Brazos-Trinity slope system: Anatomy of the terminal portion of an intra-slope lowstand systems tract, *Gulf Coast Association of Geological Societies Transactions*, **56**(1), 39-49.

Beaubouef, R., and S. Friedmann (2000). High resolution seismic/sequence stratigraphic framework for the evolution of Pleistocene intra slope basins, western Gulf of Mexico: depositional models and reservoir analogs, *GCSSEPM, 20th Annual Research Conference Deep-Water Reservoirs of the World*, 40-60.

Bouma, A. (1964). Turbidites, in *Developments in sedimentology*, **3**(1), 247-256. Elsevier.

Bouma, and C. Hollister (1973). Part III. Deep Ocean Basin Sedimentation, 79-118.

Byrnes, M., R. Hammer, T. Thibaut, and D. Snyder (2004). Effects of sand mining on physical processes and biological communities offshore New Jersey, USA, *Journal of Coastal Research*, **20**(1), 25-43.

Clare, M., D. Lintern, K. Rosenberger, J. Hughes Clarke, C. Paull, R. Gwiazda, M. Cartigny, P. Talling, D. Perara, J. Xu, D. Parsons, R. Jacinto, and R. Apprioual (2020). Lessons learned from the monitoring of turbidity currents and guidance for fturue platform designs, *Geological Society London Special Publications*, **500** (1), 605-634.

Cohen, H., and S. Hardy (1996). Numerical modelling of stratal architectures resulting from differential loading of a mobile substrate, *Geological Society, London, Special Publications*, **100**(1), 265-273.

Colling, E., R. Alexander, and R. Phair (2001). Regional mapping and maturity modeling for the northern deep water Gulf of Mexico, in *Petroleum Systems of Deep-Water Basins-Global and Gulf of Mexico Experience*, R.H. Fillon, N.C. Rosen, P. Weimer, A. Lowrie, H. Pettingill, R.L. Phair, H.H. Roberts, H.H. van Hoom (Eds.), **21**(1), 87-110.

Diegel, F., J. Karlo, D. Schuster, R. Shoup, and P. Tauvers (1995). Cenozoic structural evolution and tectono-stratigraphic framework of the northern Gulf Coast continental margin, in *Salt Tectonics - A Global Perspective: AAPG Memoir*, M. P. A. Jackson, D. G. Roberts, and S. Snelson (Eds.), **65**, 109–151.

Dorrell, R., M. Patacci, and W. McCaffrey (2018). Inflation of Ponded, Particulate Laden Density Currents, *Journal of Sedimentary Research*, **88**(11), 1276-1282.

Drazen, J., C. Smith, K. Gjerde, S. Haddock, G. Carter, C. Choy, M. Clark, P. Dutrieux, E. Goetze, and C. Hauton (2020). Midwater ecosystems must be considered when evaluating environmental risks of deep-sea mining, *Proceedings of the National Academy of Sciences*, **117**(30), 17455-17460.

Gavriletea, M. (2017). Environmental impacts of sand exploitation. Analysis of sand market, *Sustainability*, **9**(7), 1-26.

Ge, Z., R. Gawthorpe, L. Zijerveld, and A. Oluboyo (2021). Spatial and temporal variations in minibasin geometry and evolution in salt tectonic provinces: Lower Congo Basin, offshore Angola, *Basin Research*, **33**(1), 594-611.

Hand, B. (1974). Supercritical flow in density currents, *Journal of Sedimentary Research*, **44**(3), 637-648.

Heerema, C., P. Talling, M. Cartigny, C. Paull, L. Bailey, S. Simmons, D. Parsons, M. Clare, R. Gwiazda, and E. Lundsten (2020). What determines the downstream evolution of turbidity currents?, *Earth and Planetary Science Letters, 532*, 116023.

Heezen, B., and W. Ewing (1952). Turbidity currents and submarine slumps, and the 1929 Grand Banks [Newfoundland] earthquake, *American Journal of Science*, **250**(12), 849-873.

Hudec, M., and M. Jackson (2007). Terra infirma: Understanding salt tectonics, *Earth-Science Reviews*, **82**(1-2), 1-28.

Hudec, M., M. Jackson, and F. Peel (2013). Influence of deep Louann structure on the evolution of the northern Gulf of Mexico, *AAPG bulletin*, **97**(10), 1711-1735.

Hudec, M., M. Jackson, and D. Schultz-Ela (2009). The paradox of minibasin subsidence into salt: Clues to the evolution of crustal basins, *Geological Society of America Bulletin*, **121**(1-2), 201-221.

Janocko, M., M. Cartigny, W. Nemec, and E. Hansen (2013). Turbidity current hydraulics and sediment deposition in erodible sinuous channels: laboratory experiments and numerical simulations, *Marine and Petroleum Geology*, **41**(1), 222-249.

Kane, I., and M. Clare (2019). Dispersion, accumulation, and the ultimate fate of microplastics in deep-marine environments: a review and future directions, *Frontiers in Earth Science*, **7**(1), 1-27.

Khan, S., and J. Imran (2008). Numerical investigation of turbidity currents flowing through minibasins on the continental slope, *Journal of Sedimentary Research*, **78**(4), 245-257.

Kneller, B., and C. Buckee (2000). The structure and fluid mechanics of turbidity currents: a review of some recent studies and their geological implications, *Sedimentology*, **47**(1), 62-94.

Kneller, B., and B. McCaffrey (1993). Modelling the effects of salt-induced topography on deposition from turbidity currents, *GCSSEPM, 16th Annual Research Conference Salt, Sediment, and Hydrocarbons*, 137-145.

Kneller, B., and W. McCaffrey (1999). Depositional effects of flow nonuniformity and stratification within turbidity currents approaching a bounding slope: Deflection, reflection, and facies variation, *Journal of Sedimentary Research*, **69**(5), 980-991.

Ko, J. (2014). Reviews of brown dense oil/gas system of the lower Smackover Formation in North Louisiana, U.S.A., *Journal of the Korean Society of Mineral and Energy Resources Engineers*, **51**(5), 729-749.

Komar, P. (1971). Hydraulic jumps in turbidity currents, *Geological Society of America Bulletin*, **82**(6), 1477-1488.

Lamb, M., T. Hickson, J. Marr, B. Sheets, C. Paola, and G. Parker (2004). Surging versus continuous turbidity currents: flow dynamics and deposits in an experimental intraslope minibasin, *Journal of Sedimentary Research*, **74**(1), 148-155.

Lamb, M., H. Toniolo, and G. Parker (2006). Trapping of sustained turbidity currents by intraslope minibasins, *Sedimentology*, **53**(1), 147-160.

Leal Filho, W., J. Hunt, A. Lingos, J. Platje, L. Vieira, M. Will, and M. Gavriletea (2021). The unsustainable use of sand: Reporting on a global problem, *Sustainability*, **13**(6), 3356.

Losh, S., L. Walter, P. Meulbroek, A. Martini, L. Cathles, and J. Whelan (2002). Reservoir fluids and their migration into the South Eugene Island Block 330 reservoirs, offshore Louisiana, *AAPG bulletin*, **86**(8), 1463-1488.

Maharaj, V. (2012). The effects of confining minibasin topography on turbidity current dynamics and deposit architecture, Ph.D. thesis, 608 pp., University of Texas, Austin, Texas, USA.

Menard Jr, H. (1955). Deep-sea channels, topography, and sedimentation, *AAPG Bulletin*, **39**(2), 236-255.

Middleton, G. (1993). Sediment deposition from turbidity currents, *Annual Reviews of Earth Sciences*, **21**(1), 89-114.

Nasr-Azadani, M., and E. Meiburg (2014). Turbidity currents interacting with three-dimensional seafloor topography, *Journal of Fluid Mechanics*, **745**(1), 409-443.

Patacci, M., P. Haughton, and W. Mccaffrey (2015). Flow behavior of ponded turbidity currents, *Journal of Sedimentary Research*, **85**(8), 885-902.

Piper, D., and W. Normark (2009). Processes that initiate turbidity currents and their influence on turbidites: a marine geology perspective, *Journal of Sedimentary Research*, **79**(6), 347-362.

Pohl, F., J. Eggenhuisen, I. Kane, and M. Clare (2020). Transport and burial of microplastics in deep-marine sediments by turbidity currents, *Environmental Science & Technology*, **54**(7), 4180-4189.

Prather, B. (2003). Controls on reservoir distribution, architecture and stratigraphic trapping in slope settings, *Marine and Petroleum Geology*, **20**(6-8), 529-545.

Prather, B., C. Pirmez, C. Winker, M. Deptuck, D. Mohrig, B. Van Hoorn, and R. Wynn (2012). Stratigraphy of linked intraslope basins: Brazos-Trinity system western Gulf of Mexico, in *Application of the principles of seismic geomorphology to continental-slope and base-of-slope systems: Case studies from seafloor and near-seafloor analogues: SEPM, Special Publication*, Bradford E. Prather, Mark E. Deptuck, David Mohrig, Berend Van Hoorn, Russell B. Wynn (Eds.), **99**(1), 83-109.

Rotzien, J., D. Woodruff, D. Adams, Y. Gan, and J. Minken (2022). Introduction to deepwater sedimentary systems, in *Deepwater Sedimentary Systems*, edited, pp. 1-49, Elsevier.

Satterfield, W., and E. Behrens (1990). A late Quaternary canyon/channel system, northwest Gulf of Mexico continental slope, *Marine Geology*, **92**(1-2), 51-67.

Sequeiros, O. (2012). Estimating turbidity current conditions from channel morphology: A Froude number approach, *Journal of Geophysical Research: Oceans*, **117**(1), 1-19.

Sequeiros, O., H. Naruse, N. Endo, M. Garcia, and G. Parker (2009). Experimental study on self-accelerating turbidity currents, *Journal of Geophysical Research: Oceans*, **114**(1), 1-26.

Soto, J., M. Heidari, and M. Hudec (2021). Proposal for a mechanical model of mobile shales, *Scientific Reports*, **11**(1), 23785.

Steffens, G., E. Biegert, H. Sumner, and D. Bird (2003). Quantitative bathymetric analyses of selected deepwater siliciclastic margins: receiving basin configurations for deepwater fan systems, *Marine and Petroleum Geology*, **20**(6-8), 547-561.

Stricker, S., S. Jones, N. Meadows, and L. Bowen (2018). Reservoir quality of fluvial sandstone reservoirs in salt-walled mini-basins: an example from the Seagull field, Central Graben, North Sea, UK, *Petroleum Science*, **15**(1), 1-27.

Talling, P., J. Allin, D. Armitage, R. Arnott, M. Cartigny, M. Clare, F. Felletti, J. Covault, S. Girardclos, and E. Hansen (2015). Key future directions for research on turbidity currents and their deposits, *Journal of Sedimentary Research*, **85**(2), 153-169.

Talling, P., M. Baker, E. Pope, S. Ruffell, R. Jacinto, M. Heijnen, S. Hage, S. Simmons, M. Hasenhündl, and C. Heerema (2022). Longest sediment flows yet measured show how major rivers connect efficiently to deep sea, *Nature Communications*, **13**(1), 4193.

Talling, P., S. Hage, M. Baker, T. Bianchi, R. Hilton, and K. Maier (2024). The global turbidity current pump and its implications for organic carbon cycling, *Annual Review of Marine Science*, **16**(1), 105-133.

Toniolo, H., M. Lamb, and G. Parker (2006a). Depositional turbidity currents in diapiric minibasins on the continental slope: formulation and theory, *Journal of Sedimentary Research*, **76**(5), 783-797.

Toniolo, H., G. Parker, and V. Voller (2007). Role of ponded turbidity currents in reservoir trap efficiency, *Journal of Hydraulic Engineering*, **133**(6), 579-595.

Toniolo, H., G. Parker, V. Voller, and R. Beaubouef (2006b). Depositional turbidity currents in diapiric minibasins on the continental slope: experiments—numerical simulation and upscaling, *Journal of Sedimentary Research*, **76**(5), 798-818.

Violet, J., B. Sheets, L. Pratson, C. Paola, R. Beaubouef, and G. Parker (2005). Experiment on turbidity currents and their deposits in a model 3D subsiding minibasin, *Journal of Sedimentary Research*, **75**(5), 820-843.

Wahab, A., D. Hoyal, M. Shringarpure, and K. Straub (2022). A dimensionless framework for predicting submarine fan morphology, *Nature Communications*, **13**(1), 7563.

Wiener, R., M. Mann, M. Angelich, and J. Molyneux (2011). Mobile shale in the Niger Delta: Characteristics, structure, and evolution, in *Shale Tectonics: AAPG Memoir*, L. Wood (Ed.), **93**(1), 145-161.

CHAPTER 2

Circulation of hydraulically ponded turbidity currents and the filling of continental slope minibasins

ABSTRACT

Natural depressions on continental margins termed minibasins trap turbidity currents, a class of sediment-laden seafloor density driven flow. These currents are the primary downslope vectors for clastic sediment, particulate organic carbon, and microplastics. Here, we establish a method that facilitates long-distance self-suspension of dilute sediment-laden flows, enabling study of turbidity currents with appropriately scaled natural topography. We show that flow dynamics in three-dimensional minibasins are dominated by circulation cell structures. While fluid rotation is mainly along a horizontal plane, inwards spiraling flow results in strong upwelling jets that reduce the ability of minibasins to trap particulate organic carbon, microplastics, and fine-grained clastic sediment. Circulation cells are the prime mechanism for distributing particulates in minibasins and set the geometry of deposits, which are often intricate and below the resolution of geophysical surveys. Fluid and sediment are delivered to circulation cells by turbidity currents that runup the distal wall of minibasins. The magnitude of runup increases with the discharge rate of currents entering minibasins, which influences the amount of sediment that is either trapped in minibasins or spills to downslope environs and determines the height that deposits onlap against minibasin walls.

INTRODUCTION

Density driven geophysical flows help sculpt the land- and sea-scape of Earth and other planetary bodies [*Babonneau et al.*, 2010; *Horvath et al.*, 2021; *Komatsu*, 2007;

Simpson, 1982; *Waltham et al.*, 2008;]. Turbidity currents, a class of gravity flows that gain excess density by suspension of sediment, are the primary particulate transport process on the slope of Earth's continental margins [*Talling et al.*, 2015]. These flows represent geohazards to submarine infrastructure [*Carter et al.*, 2014] and transport to the deep marine huge volumes of clastic sediment [*Talling et al.*, 2023a], particulate organic carbon [*Galy et al.*, 2007; *Masson et al.*, 2010; *Stetten et al.*, 2015; *Talling et al.*, 2023b], and microplastics [*Kane et al.*, 2020] in addition to dissolved nutrients and pollutants [*Almroth et al.*, 2009; *Kane et al.*, 2020]. Models of these flows often assume that the mechanics of sediment transport by turbidity currents are similar to rivers, but recent work highlights challenges in porting knowledge from rivers to the deep marine [*Fukuda et al.*, 2023]. For example, on their path down slope, turbidity currents encounter, interact with, and construct topography. Turbidity current interactions with topography can be quite complex and different than terrestrial flows, due to their relatively low contrast in density with sea water. Studies which explore the interaction of turbidity currents with submarine channels [*Abd El-Gawad et al.*, 2012; *Keevil et al.*, 2006; *Straub et al.*, 2008; *Talling et al.*, 2022], topographic slope-breaks [*Fernandez et al.*, 2014; *Nasr-Azadani and Meiburg*, 2014; *Sequeiros et al.*, 2009], and obstacles such as sea mounts [*Völker et al.*, 2008] document how subtle topography can warp the structure of the velocity and sediment concentration fields, impacting their sediment transport capacity. Possibly the most complex interactions develop when flows enter enclosed depressions. Depressions with depths comparable to, or significantly greater than, the heights of turbidity currents enhance deposition of particulates and are termed minibasins [*Mitchum Jr. et al.*, 1977].

Unfortunately, there is a lack of direct observations of field scale turbidity currents interacting with minibasins, primarily due to their: 1) relatively inaccessible locations, 2) unpredictable flow occurrences, and 3) high flow shear stresses that can destroy equipment [*Azpiroz-Zabala et al.*, 2017; *Khripounoff et al.*, 2003]. Development of theory in these settings has thus leveraged numerical and physical experiments [*Bastianon et al.*, 2021; *Brunt et al.*, 2004; *Toniolo et al.*, 2006a; *Traer et al.*, 2018; *Violet et al.*, 2005; *Wang et al.*, 2017]. Due to computational demands, many numerical models utilize depth-averaged flow parameters [Yang et al., 2019; Meiburg et al., 2015]. These models afford some insights in unconfined settings and help to define the link between fluid and sediment transport dynamics and the shape of submarine fans [*Wahab et al.*, 2022]. However, their depth-averaged formulations limit their applicability in settings where vertical flow properties vary strongly in space and time, such as in minibasins [*Bastianon et al.*, 2021; *Lamb et al.*, 2006; *Patacci et al.*, 2015]. In addition, while a few physical experiments document flow interactions with topography in three-dimensions, 3-D [*Maharaj*, 2012; *Soutter et al.*, 2021; *Violet et al.*, 2005], most physical experiments on turbidity current – minibasin interactions have been conducted in 2-D [*Lamb et al.*, 2004; *Pohl et al.*, 2020; *Spinewine et al.*, 2009; *Toniolo et al.*, 2006a; *Traer et al.*, 2018]. Further, most of these experiments utilize quartz particles with grain sizes that are difficult to keep in suspension at laboratory scales.

Minibasins are efficient traps of particulate material because they can induce hydraulic flow ponding, a process that initiates with the reflection of flows off confining topography. This triggers a rapid spatial flow deceleration to extremely low densimetric Froude, Fr_d, conditions and the formation of a placid flow transition with the overlying ambient fluid, decreasing the entrainment of ambient fluid into the current [*Lamb et al.*, 2004; *van Andel and Komar*, 1969]. Flow circulation within 2-D minibasins was documented along a vertical plane, with a return flow positioned above down-basin directed flow [*Patacci et al.*, 2015] (Fig. 1A). Below the return flow, ponding leads to concentration profiles with little vertical structure, as sediment lost to deposition is replaced from above with more sediment laden flow. This produces tabular deposits that do not rapidly thin against confining topography [*Lamb et al.*, 2004; *Toniolo et al.*, 2006a]. Previously it has been unclear if this style of circulation develops in 3-D minibasins. However, flow circulation in minibasins has implications for the near bed shear stress and sediment transport capacity, thus impacting the trapping potential of particulates.

Here, the influence of flow discharge into circular minibasins on the 3-component velocity field, structure of sediment concentration profiles, and resulting turbidite shape is studied. To accomplish this, a turbidity current mixture is developed that overcomes many past experimental scaling challenges. Further, turbidity currents are released into minibasins with scales that surpass prior experimental setups. This scale is sufficient to allow the geometry of experimental minibasins to resemble their field scale counterparts, while also trapping flows of sufficient thickness to allow for measurement of flow structure. Flow discharge is varied by adjusting input flow width, while keeping all other input conditions constant (flow height, mean inlet velocity, sediment concentration). The setup is designed to capture end members across a spectrum of complete flow trapping, stripping of the upper current, and focused discharge of the full flow to downslope environs (i.e., the fill-to-strip-to-spill transition) [*Badalini et al.*, 2000; *Beaubouef and Abreu*, 2006; *Beaubouef and Friedmann*, 2000; *Satterfield and Behrens*, 1990; *Winker*, 1996]. Lateral circulation cells are discovered and quantified, which are the primary process responsible for distributing sediment throughout minibasins. Further, these circulation cells link to upwelling flow that impacts sedimentation processes by countering the still fluid settling velocity of particles. This upwelling has particular importance for the trapping of particulates with low settling velocities (i.e., particulate organic carbon and microplastics).

RESULTS

Experimental Design

Turbidity currents were released into minibasins with a 3 m diameter. This scale is significantly greater than prior experimental campaigns that quantified the fluid dynamics of ponded flows (e.g., Bastianon [2018] where basin diameter = 1m with ~40% sidewall slopes and Maharaj [2012] where basin diameter = 0.5m with ~30% sidewall slopes). These prior experiments had minibasin side wall slopes that were significantly steeper than observed in nature, where slopes rarely exceed 14%. The steep slopes allowed minibasins to achieve significant depth with minimal planform diameter, which aided monitoring of flows that had thicknesses comparable to minibasin relief. The circular minibasin in this study had a 10% sidewall slope and a 0.12 m depth. Dimensionless ratios characterizing minibasin topography, including side wall slope, fall within distributions generated from 2,324 depressions extracted from the Bureau of Ocean and Energy Management's bathymetric dataset of the northern Gulf of Mexico [*BOEM*, 2017]. Sustained turbidity currents were delivered to the rim of minibasins for 30 minutes. Input flows had densimetric Froude numbers of 1.1, were 48 mm thick, and had an excess density of 2.9%.

Many turbidity current physical experiments use quartz sediment [*Bastianon*, 2018; *Lamb et al.*, 2004; *Patacci et al.*, 2015; *Violet et al.*, 2005], which is difficult to keep in suspension at laboratory scale, even those in the fine silt size range. To overcome this, some studies add salt to enhance the driving gravitational force and production of turbulence [*Cantelli et al.*, 2011; *Sequeiros et al.*, 2010; *Straub et al.*, 2008]. This is rationalized by equating the dissolved salt with washload, a fraction of the sediment load that bypasses a reach with limited to no bed interaction. Use of salt would not mimic field scale processes of turbidity current interaction with minibasins that can trap flows and all their sediment. To overcome prior experimental limitations, a slurry recipe was developed, composed of 1% aluminum oxide sediment (particle density of 3950 kg/m^3 and median particle diameter of 14 μm) and a deflocculant mixture containing calcium carbonate and sodium hexametaphosphate (SHMP) that was used to inhibit amalgamation of fine scale particles. The high-density aluminum oxide sediment produces significant excess density from low volumetric sediment concentrations, generating swifter, more turbulent flows [*Fukuda et al.*, 2023]. This allows transport of particles to greater distances prior to deposition.

Three experiments were performed, each composed of two flow events, and are referred to as the low-flux, mid-flux, and high-flux experiments. The range of input discharge results in flows that span the fill (low-flux) to strip (mid-flux) to spill (high-flux) spectrum. During the first event a 3-component velocity profile timeseries was collected at minibasin center for the duration of the flow using a Pulse Coherent Acoustic Doppler Profiler (PCADP), in addition to sediment concentration profiles collected after equilibrium conditions were reached. During the second event, velocity profiles were collected after equilibrium conditions were reached at a set of positions covering the river-left side of the minibasins. Topography was mapped with a displacement laser before and after each experiment.

Minibasin Center Conditions

Equilibrium velocity conditions at minibasin center are estimated by averaging profiles collected from the first flow of each experiment over the duration that concentration profiles were collected. Here, *u*, *v*, and *w* refer to the velocity components in the down-basin, cross-basin, and vertical directions, respectively. For comparison, *u* profiles at minibasin center are normalized by the maximum down system velocity of a profile, u_{max} (Fig. 2A). Profiles collected from unconfined flows typically have a velocity maximum at a height that is between 10-35% of the total flow height [*Altinakar et al.*, 1996; *Sequeiros et al.*, 2010; *Talling et al.*, 2023a]. In contrast, the flow structure from the confined conditions herein display significantly elevated velocity maxima. The low-flux condition has the most complicated velocity structure, with low velocities in the lower third of the flow, peak velocities in the middle third and a rapid velocity reduction in the upper third of the flow. The mid and high-flux conditions are less stratified and have peak velocities just below the minibasin rim elevation.

Sediment concentration profiles are compared following normalization by near bed conditions, C_{nb} (Fig. 2B). The low-flux experiment, which was the most contained within the minibasin, is the most stratified. The mid and high-flux conditions are well mixed in the lower two-thirds of the elevations contained within the minibasin. Sediment concentrations then rapidly decrease to near zero values approaching the rim elevation.

Evolution of Down Minibasin Velocity

Experiments had differences in discharge, controlled by initial flow width, that generated different minibasin floor velocity due to varying lateral flow expansion (Fig. 2C) between experiments. All experiments show a rapid spatial deceleration in u_{max} with distance into the minibasin, as flow ponded triggering a rapid increase in flow height and decrease in densimetric Froude number. Minibasin floor velocities are used to estimate flow runup onto the distal minibasin wall. The magnitude of runup is estimated by:

$$\Delta z = \frac{\rho_c u_{max}^2}{(\rho_c - \rho_a) 2g}, \qquad \text{[EQ. 1]}$$

where ρ_c and ρ_a are current and ambient fluid densities and g is gravitational acceleration [*Dorrell et al.*, 2018; *Straub et al.*, 2008]. Here, ρ_c is estimated from measurements of sediment concentration. Use of Eq. 1 results in estimates of 3.9, 9.5, and 27.8 mm of runup for the low, mid, and high flux experiments, respectively. Finally, it is noted that measurements of u_{max} above the downstream minibasin rim (Fig. 2C) indicate that the experiments captured the fill-to-strip-to-spill transition. The low-flux experiment (characterizing the "fill" end member) has near zero u_{max} above the distal rim, which ticks up to ~15 mm/s for the mid-flux ("strip") condition and reaches ~35 mm/s for the high-flux ("spill") condition.

Circulation Cells

Overhead imagery (Supplementary Movies 1-4) and velocity measurements covering the river left hand side of the minibasins (Figs. 3&4) captures paired fluid circulation cells spawned from the current interaction with the distal slope. These cells are visualized by first calculating streamlines from velocity measurements, which capture horizontal gathering of flow into the center of the circulation cells and strong upwelling flow at the cell center (Fig. 3). The circulation cells span the full extent of the ponded flow, which surrounds an inlet flow region defined by high Fr_d and turbulent flow conditions [*Lamb et al.*, 2004]. The inlet flow conditions do not cover the full width of the minibasins, and therefore these circulation structures control sediment transport and delivery over the majority of the minibasin area. Fluid movement through minibasins are characterized using vector maps of the temporally averaged depth integrated fluid flux in the down and cross basin directions:

$$q_u = \int_0^H u dz, \qquad \text{[EQ. 2A]}$$

$$q_v = \int_0^H v dz, \qquad \text{[EQ. 2B]}$$

where *H* represents the current height, estimated with the integral length scale [*Ellison and Turner*, 1959] (Fig. 4A). Temporal averaging was done over the duration that the PCADP sampled each site. When vectors are scaled by input discharge, the structure of the discharge field is remarkably similar across experiments, hinting towards the universal importance of these circulation cells for the sediment transport dynamics that control minibasin infilling across the fill-to-strip-to-spill spectrum. High fluxes down the proximal slope efficiently deliver fluid and sediment to the center of minibasins. Down basin depth integrated fluxes then rapidly decrease going up the distal minibasin slope as fluid is routed into circulation cells. Due to the inlet flow entering the center of the minibasin in these experiments, the cells are laterally offset and positioned over the lower lateral slope.

Gradients in the velocity field of the confined flow describe local fluid stretching (strain) and rotation (vorticity), which are quantified at all sample points. From Dubief and Delcayre [2000], the horizontal strain rate tensor is calculated from the symmetric part of the velocity gradient tensor as:

$$S = \tfrac{1}{2}[(\delta u/\delta x) + (\delta v/\delta y)], \qquad \text{[EQ. 3]}$$

and the horizontal vorticity is calculated from the asymmetric part of the velocity gradient tensor as:

$$\Omega = \tfrac{1}{2}[(\delta v/\delta x) - (\delta u/\delta y)], \qquad \text{[EQ. 4]}$$

where x and y are down and cross basin locations, respectively. Strength of rotation relative to the lateral strain rate of the fluid is quantified using the Q-criterion, Q:

$$Q = \tfrac{1}{2}\left(\left||\Omega|\right|^2 - \left||S|\right|^2\right). \qquad \text{[EQ. 5]}$$

Positive Q indicates local vorticity exceeds shear (strain rate tensor), and negative values represent areas where strain rate dominates the 3-D flow field [*Dubief and Delcayre*, 2000]. Here circulation with positive Q at the cell center is associated with upwelling fluid, a consequence of fluid mass conservation. This 3-D flow pattern controls sediment transport and deposition. Here, results from the high-flux condition are presented, which are similar in structure (but different in magnitude) to the other experiments (Fig. 4). Maps of Q at various minibasin depths highlight that the centers of the circulation cells have vorticity that exceeds the strain rate (Fig. 4D-E). While Q values indicate whether vorticity or strain rate is larger at a point, they do not inform on the fractional difference of the two. This can be estimated with the kinematic vorticity number [*Dubief and Delcayre*, 2000]:

$$\Omega_k^* = \frac{||\Omega||}{||S||}. \qquad \text{[EQ. 6]}$$

Vorticity, strain rate, and the *w* velocity component near the center of the circulation cell are determined for all heights in the minibasin. The center of this cell laterally migrates away from minibasin center with increasing water depth (Fig. 3). Near the center of the vortex, Ω^*_k ranges between 2 to 75, suggesting limited fluid stretching during rotation (Fig. 4B). This is associated with a profile of the *w* velocity component with upwards directed flow that considerably exceeds the still sediment fall velocity, w_s, of the median grain size introduced to the basin (0.5 mm/s) and the vertical detrainment velocity (Fig. 4C). This upwelling flow will influence sediment settling velocities as a function of the grain size distribution, leading to enhanced trapping potential of coarse clastic particles, relative to particulate organic carbon and microplastics that have low settling velocities. However, the profile has considerable structure with significant upwards directed flow in the lower third of the current, which reduces to near zero in the middle of the flow. This reduction might be linked to low vertical shear at the u_{max} elevation [*Islam and Imran*, 2010]. The top third of the flow again is defined by upwelling that exceeds w_s.

Minibasin Margin Onlap

Sedimentation patterns are characterized using isopach maps, calculated by differencing initial and final topography for an experiment. As a different total volume of sediment was released into the basin for each experiment, due to different flow discharges, deposition is normalized by the mean deposit thickness over the flat minibasins floor, D^* (Fig. 5A-C). While the structure of the concentration profiles at minibasin center might suggest similar gradients in deposition with distance up minibasin slopes, stark differences are observed between experiments in the deposit taper against slopes. Most of the sediment released into the low-flux experiment is contained within the minibasin, with deposit thickness at the minibasin rim only 10% of minibasin center thickness. In contrast, deposit thickness at the rim elevation exceeds 50% of minibasin center thickness for the high-flux experiment, highlighting the spilling nature of this experiment. Excluding data from the proximal slope that was covered by inlet flow conditions, the rate of thinning up minibasin slopes is quantified by binning measurements of normalized deposit thickness by elevation above minibasin center, with 1 mm tall bins. Bin averaged data generate an average onlapping profile that is a function of normalized minibasin elevation, equal to elevation above minibasin center / minibasin depth, z^* (Fig. 5D). These profiles detail the rate of thinning, which is quantified with an onlap index we developed, equal to the area underneath the curves in figure 5D:

$$I_o = \int_0^1 D^* dz^*. \qquad \text{[EQ. 7]}$$

Thus, sedimentation that does not change thickness up minibasin walls would yield an I_o of 1, while a linear decrease in sedimentation from minibasin center values to zero deposition on the minibasin rim would yield an I_o of 0.5. Here I_o values of 0.48, 0.58, and 0.72 are measured for the low, mid, and high flux experiments, respectively.

DISCUSSION

As some of the largest sediment transport processes on the Earth's surface, turbidity currents are critically important. Traversing the seafloor they are often subject to large topographic constraints, such as minibasins. While minibasins are present on many continental margins, the northern Gulf of Mexico is characterized by an extensive and exquisite minibasin province resulting from the movement of the Louann salt [*Hudec et al.*, 2013; *Steffens et al.*, 2003]. The complex topography resulting from this mobile substrate and the geofluid reservoirs housed in minibasin strata have led to several conceptual models for turbidity current-minibasin interactions [*Badalini et al.*, 2000; *Beaubouef and Friedmann*, 2000; *Pirmez et al.*, 2012; *Prather et al.*, 2012; *Winker*, 1996]. Many of these models were motivated by the Brazos-Trinity minibasin system in the northern Gulf of Mexico, which has been extensively studied through geophysical surveys and litho- and chrono-stratigraphic characterization of cores (experiments presented herein are not designed to simulate any one system and lab-field comparisons remain imperfect due to limitations in dynamic scaling methods [*Paola et al.*, 2009]). This system also motivated earlier 2-D physical experiments, but notable differences exist in the structure of strata filling Brazos-Trinity minibasins and the deposits of these 2-D physical experiments. Namely, results from the 2-D experiments suggest that ponded turbidity currents should have limited structure to their concentration profiles, either in the vertical or down basin sense [*Lamb et al.*, 2006; *Toniolo et al.*, 2006b]. As a result, sustained experimental flows resulted in deposits that blanketed topography, with limited thinning over confining topography. However, deposits in Brazos-Trinity minibasins, which are thought to be the product of equilibrated and sustained flows, rapidly thin onto minibasin slopes. Further, any apparent onlap of deposits up Brazos-Trinity minibasins slopes is argued to be the product of ongoing subsidence during the last episode of sediment delivery to this system [*Sylvester et al.*, 2015].

Formulations that relate slope to densimetric Froude number suggest inlet flows to many minibasins are near critical[65]. Utilizing this assumption, a comparison between the experiments described here and Brazos-Trinity Basin II is made. A portion of this minibasin's fill (Series 30) is interpreted as a ponded apron, suggesting possible hydraulic ponding conditions during deposition [*Prather et al.*, 2012]. These turbidites have grain sizes in the mud to very fine sand spectrum. In comparison, upscaled grain sizes introduced to the experiments using established methods [*Graf et al.*, 1971] (see extended methods) are equivalent to 73-81 μm quartz sediment in flows with a 1.8% volumetric sediment concentration, i.e. similar to those delivered to Basin II. A comparison of the ratio of input current discharge to flow trapping potential, Q^*, is also made for Basin II and the experiments described herein (Fig. 5). Input discharge to Basin II is calculated assuming critical Fr_d conditions and estimates of flow heights and widths from the geometry of the self-formed and aggradational channel entering Basin II (see extended methods). The flow trapping potential is estimated during Series 30 as the product of minibasin area and suspended sediment settling velocity [*Lamb et al.*, 2006]. The area of Basin II at this time is estimated from published isopach maps [*Prather et al.*, 2012], while settling velocities are calculated for the range of scaled grain sizes detailed above. This results in a possible range for Q^* between 0.11 – 0.16. In the experiments Q^* is equal to 0.25, 0.5, and 1.0, for the low, mid, and high flux conditions, respectively. As Q^* decreased for the physical experiments, the onlap index also decreased. Carrying the near linear experimental trend between these variables to the values of Q^* estimated for Brazos-Trinity Basin II, while acknowledging the limited number of experimental conditions explored, would yield an onlapping index of between only 0.44 – 0.46.

The link between Q^* and the onlap index is hypothesized to be through the magnitude of flow runup onto distal minibasin slopes. Sediment not lost due to upwelling, flow stripping, and/or spilling ultimately gets deposited within the minibasin. Deflection of flow running up the distal slope routes sediment laden flow over the lateral minibasin slopes, resulting in deposition throughout the minibasin (Fig. 1B). It is highlighted that normalized sediment concentration profiles at minibasin center are similar for the three experimental conditions, but the onlap index, I_o, varies greatly between experiments (Fig. 5). However, a comparison of Δz resulting from runup to the onlap index (Eq. 7) yields a near linear trend (Fig. 5E). This suggests that the magnitude of runup on the distal minibasin slope sets the amount of sediment delivered to circulation cells, which then distribute sediment minibasin wide. The theory behind this prediction might therefore explain the limited amount of onlap of turbidites onto Brazos-Trinity minibasin slopes, which has been frequently noted [*Badalini et al.*, 2000; *Prather et al.*, 2012]. This result also supports arguments that some of the apparent onlap noted in the ponded apron fill of Basin II might be the result of active subsidence during deposition [*Sylvester et al.*, 2015].

A key finding of this study is the new observation of paired circulation cells resulting from turbidity currents interacting with minibasin topography (Supplementary Movies 1-4, Fig. 1B & 3-4). Velocities within these circulation cells vary as a function of input discharge. However, their structure, following normalization, is remarkably similar over the fill-to-strip-to-spill spectrum (Fig. 4A). This structure is setup during the initial traverse of the turbidity current front, which does not fill the full minibasin width (Supplementary Movies 1-4). Reflection off the distal slope results in return flow along lateral minibasin slopes. This same structure is observed during equilibrium conditions, where inlet flow sends dye into the minibasin center with minimal widening until it reflects laterally when running up the distal slope (Supplementary Movies 1-4).

Prior 2-D experiments highlighted circulation in minibasins along a vertical plane [*Patacci et al.*, 2015] (Fig. 1A). During equilibrium conditions, return flow is not observed at the center of the minibasin (Fig. 2). This suggests the ability of currents to laterally expand and setup circulation along a horizontal plane suppresses the development of circulation along a vertical plane. As a result, sediment charged flow that cannot escape over the distal rim is directed to and deposited on the lateral slopes.

Study of circulation cells in flows has a long history in sedimentology, including controlling the formation of river meanders [*Einstein*, 1926] and bedform development

[*Gilbert and Murphy*, 1914]. Here, the centers of minibasin circulation cells have positive Q-criterion indicating the importance of lateral fluid rotation in ponded turbidity currents. The gathering of flow towards the center of cells (Fig. 3) drives upwelling with vertical fluid velocities that exceed the still fluid settling velocity of sediment introduced to the minibasins (Figs. 3&4C). However, vertical velocity profiles suggest sediment entering the lower portions of the vortex might not be able to transit to the flow top. This likely creates a sediment trap that enhances sediment concentrations until the flow wanes and sediment rains to the bed. This could be the reason for the thick deposits offset either side of minibasin center in the high-flux experiment (Fig. 5C), with a counter argument being that extension of high velocity flow into the minibasin center reduced deposition rates over the minibasin floor, relative to slopes. However, sediment entering the vortex in the upper third of the flow likely can escape the flow top, reducing basin sediment trapping potential relative to theory generated from 2-D minibasin experiments [*Lamb et al.*, 2006]. Thus, circulation cells likely play a significant role in the fractionation of particulates, pollutants, and nutrients. This preferential expulsion of low settling velocity particulates likely enhances flow stripping, which has previously been linked to coarsening of proximal intraslope fans [*Jobe et al.*, 2017]. Specifically, in a linked system of minibasins, the ability for proximal minibasins to act as a sink for microplastics and particulate organic carbon, which have low settling velocities, may be significantly reduced.

The development of circulation cells and the magnitude of flow runup as a function of influx have additional potential implications for models of the temporal evolution of linked minibasins[47,48], such as the Brazos-Trinity system. Specifically, during the early filling of minibasins, development of circulation cells likely enhances the flux of sediment delivered to downslope minibasins. However, the enhanced export of fines due to the upwelling at the center of circulation cells might mean that the early fill of distal minibasins is finer than proposed by models that did not include circulation cells [*Badalini et al.*, 2000; *Winker*, 1996]. Our results also highlight that even in minibasins with significant focused flow spilling over a down-basin rim (i.e., the high-flux experiment), circulation cells develop along the lateral margins of minibasins. This circulation develops in relatively quiescent and ponded flow, in comparison to a core of higher velocity and more turbulent flow that extends from the basin inlet to distal sill. This suggests strong lateral fining in minibasin fill during time periods of focused spilling of flow to down slope minibasins.

Finally, the vertical flow structure captured in these experiments, which is the result of flow ponding and the development of circulation cells, differs strongly from unconfined turbidity currents [*Altinakar et al.*, 1996; *Sequeiros et al.*, 2010]. Development of rules and theory emanating from 3-D experiments will aid future development of layer-averaged models of turbidity currents interacting with complicated topography. Specifically, they offer test data to develop shape functions [*Dorrell et al.*, 2014] for velocity and sediment concentration structure that could be used for improving the performance of layer average models.

METHODS

Expanded Experimental Methods

Experiments were performed in a 6 x 4 x 2.2 m basin. Circular minibasins were carved into 300 μm sand on a raised platform within the experimental basin that was surrounded by moats to limit current reflections off the larger experimental basin side walls. Minibasins had a diameter of 3 m, 10% sidewall slopes, and a 0.12 m depth.

Minibasins were submerged in room temperature fresh water with 0.69 m of water above the minibasin rim. Turbidity currents released into the experimental basin gained excess density through suspension of aluminum oxide sediment in room temperature water with a deflocculant that consisted of calcium carbonate and sodium hexametaphosphate. The experiments used 4 grams of deflocculant for every liter of fluid. The mass in the deflocculant was 21% calcium carbonate and 79% sodium hexametaphosphate. Volumetric sediment concentration was 1% with D_5, D_{25}, D_{50}, D_{75}, D_{95} of 6, 11, 14, 17, and 24 µm, respectively. Input flux was 24, 47.7, and 96.9 l/min with corresponding entrance slots that were 65, 130, and 260 mm wide for the low, mid, and high flux experiments, respectively.

The three-component velocity field was measured using A 2 MHz Nortek pulse coherent acoustic doppler profiler (PCADP). The PCADP was attached to a robotic arm on a measurement carriage suspended above the experimental basin. This carriage can move instruments to locations within the experimental basin with a 1 mm precision. The PCADP measures the velocity field once per second in a series of 8mm tall bins beneath the probe. A profile of sediment concentrations at equilibrium conditions was collected 26 – 27.5 min into each experiment. The sediment concentration profile was collected with a system of ten siphons vertically stacked with 15 mm spacings and positioned at minibasin center 10 mm above the sediment interface. Following fluid evaporation, extracted sediment mass was measured to generate concentration measurements at basin center. Three cameras fixed above the experimental basin capture in high spatial resolution the evolving flow field at 0.25 Hz through the entirety of each flow event. These images were used to make time lapse videos of the experiments. A zero-offset Keyance laser, contained in a waterproof casing, submerged below the water line was used for measuring topography over a 5 mm by 5 mm grid with a 0.25 mm vertical resolution. Isopachs were generated from differencing initial topographic scans before each flow event and from post-flow scans.

Comparison and Scaling with Brazos-Trinity Minibasin II

Following established methods, we scale our experimental conditions to field conditions. We focus this endeavor on flows of the scale that filled Brazos-Trinity Minibasin II. We emphasize that our experiments were not designed to simulate any one field site and that established engineering scaling methods carry limitations [*Paola et al.*, 2009]. As such, the scaling presented here is only intended to guide how experimental results might be applied to the interpretation of field scale minibasins. We apply a dynamic scaling protocol that assumes similarity between the model (experiment) and prototype (field) systems and focuses on the densimetric Froude number, equal to:

$$Fr_d = \frac{\bar{u}}{\sqrt{RgCH}}, \qquad \text{[EQ. 8]}$$

where $\bar{u}$ is the mean current velocity, R is the submerged specific gravity of sediment, g is gravitational acceleration, C is the volumetric sediment concentration, and H is the current height. We set $Fr_{d(\mathrm{model})} = Fr_{d(\mathrm{prototype})}$, which with the rules defined in Graf [1971], under the constraint of constant reduced gravity (i.e., RgC), and a geometric scale factor, λ, results in the following relationships:

$$u_p = \lambda^{1/2} u_m, \qquad w_{s,p} = \lambda^{1/2} w_{s,m}. \qquad \text{[EQ. 9a,b]}$$

We measured a 30 m deep self-formed and aggradational feeder channel to Basin II using the BOEM bathymetry [*BOEM*, 2017] map, suggesting input flow heights between 30-45 m [*Mohrig and Buttles*, 2007]. Given this range and the height of our experimental input flows, we apply a range geometric scale factors between 600-900, which yield estimates of input u_p between 3.2 – 3.9 m/s and $w_{s,p}$ between 3.85 x 10^{-3} – 4.71 x 10^{-3} m/s. This range in settling velocities can be converted to a quartz particle diameter using the Ferguson and Church method [*Ferguson and Church*, 2004] and suggests a prototype quartz sediment in transit between 73-81 μm, similar to the ponded apron fill of Basin II [*Prather et al.*, 2012].

We also estimate a ratio of an input flow discharge to minibasin flow trapping potential for both our experiments and Brazos-Trinity Basin II. We estimate the discharge delivered to Basin II as the product of our estimated flow velocity, flow depth, and flow width. Flow width is estimated from a measured feeder channel width of 225 m and again we explore a range of flow heights and associated flow velocities, as outlined above, which yields a range of input minibasin discharges between $2.2 \times 10^4 – 4.0 \times 10^4$ m^3/s. Next, we estimate the minibasin flow trapping potential as the product of the still fluid sediment settling velocity and the minibasin planform area [*Lamb et al.*, 2006]. We use our prototype settling velocities and an area of Basin II equal to 5.2×10^7 m^2, estimated from the area of Series 30 deposition within Basin II [*Prather et al.*, 2012]. This yields a plausible range of flow trapping potential between $2 \times 10^5 – 2.5 \times 10^5$ m^3/s. This then yields a range in the ratio of input flux to minibasin flow trapping potential between 0.11 – 0.16 for Basin II. This same ratio was between 0.25 – 1.0 for our suite of experiments. While not an identical match, the experimental conditions are within an order of magnitude of estimated field conditions, supporting our assertion that circulation cells are also important for distributing sediment in field scale minibasins.

LIST OF FIGURES

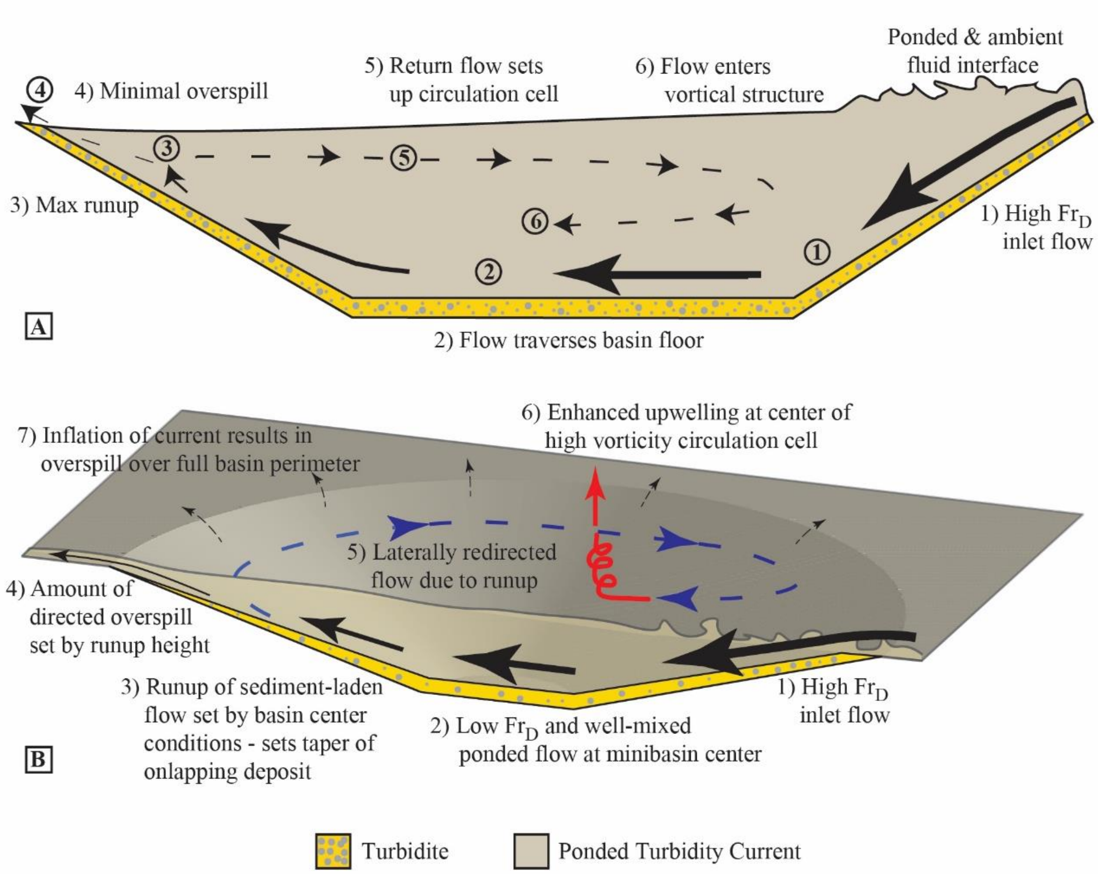

Figure 1. Schematics of turbidity current – minbasin interactions. A) 2-D and B) 3-D schematics of circulation cell development inside topographically enclosed minibasins.

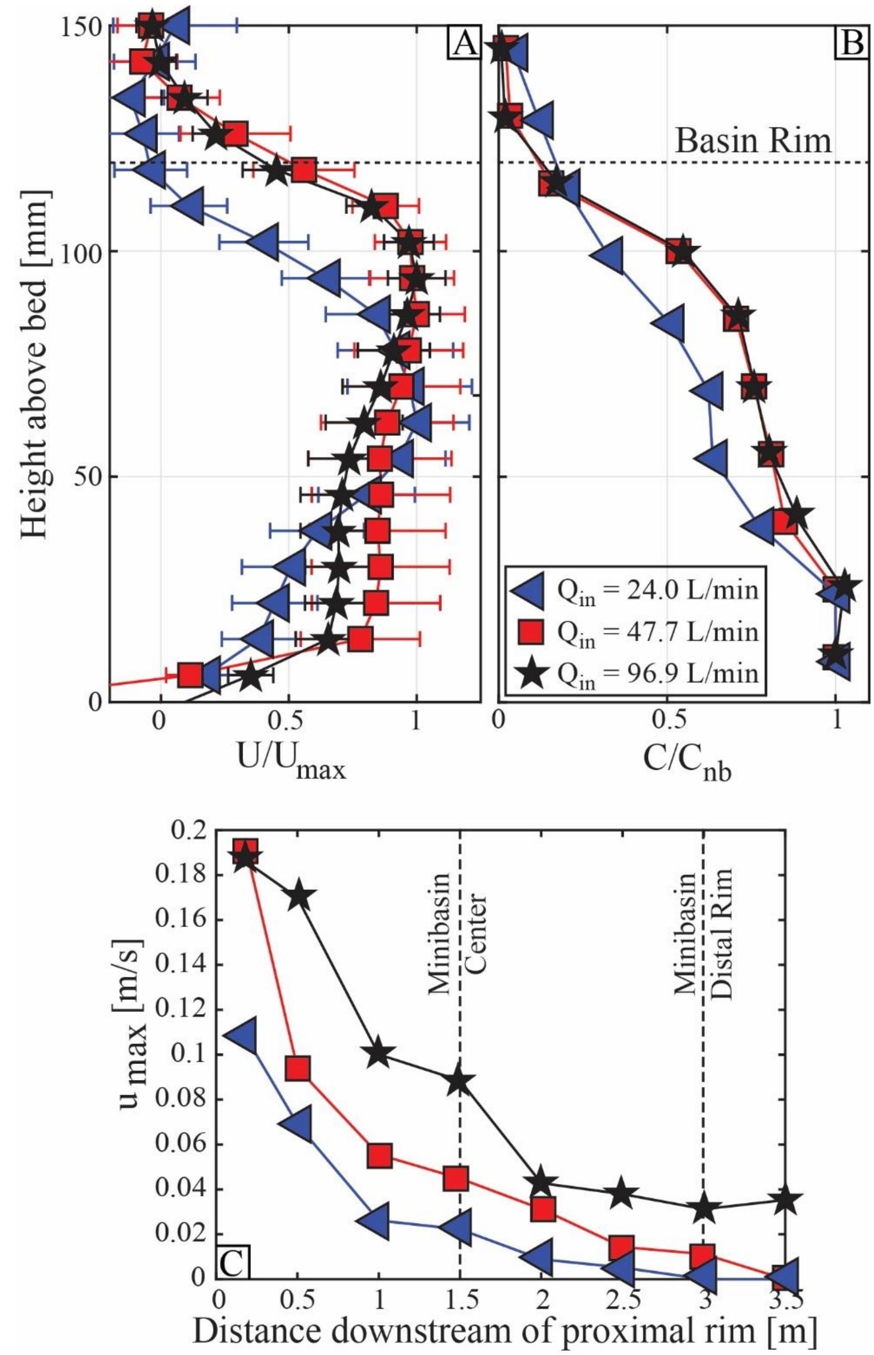

Figure 2. Fluid and sediment transport fields at minibasin center. Velocity and concentration measurements at minibasin center and flow evolution along the down basin traverse. A-B) Profiles at minibasin center normalized by the maximum velocity in a profile and near bed sediment concentration, respectively. C) Measurements of the maximum velocity along the basin bisect line.

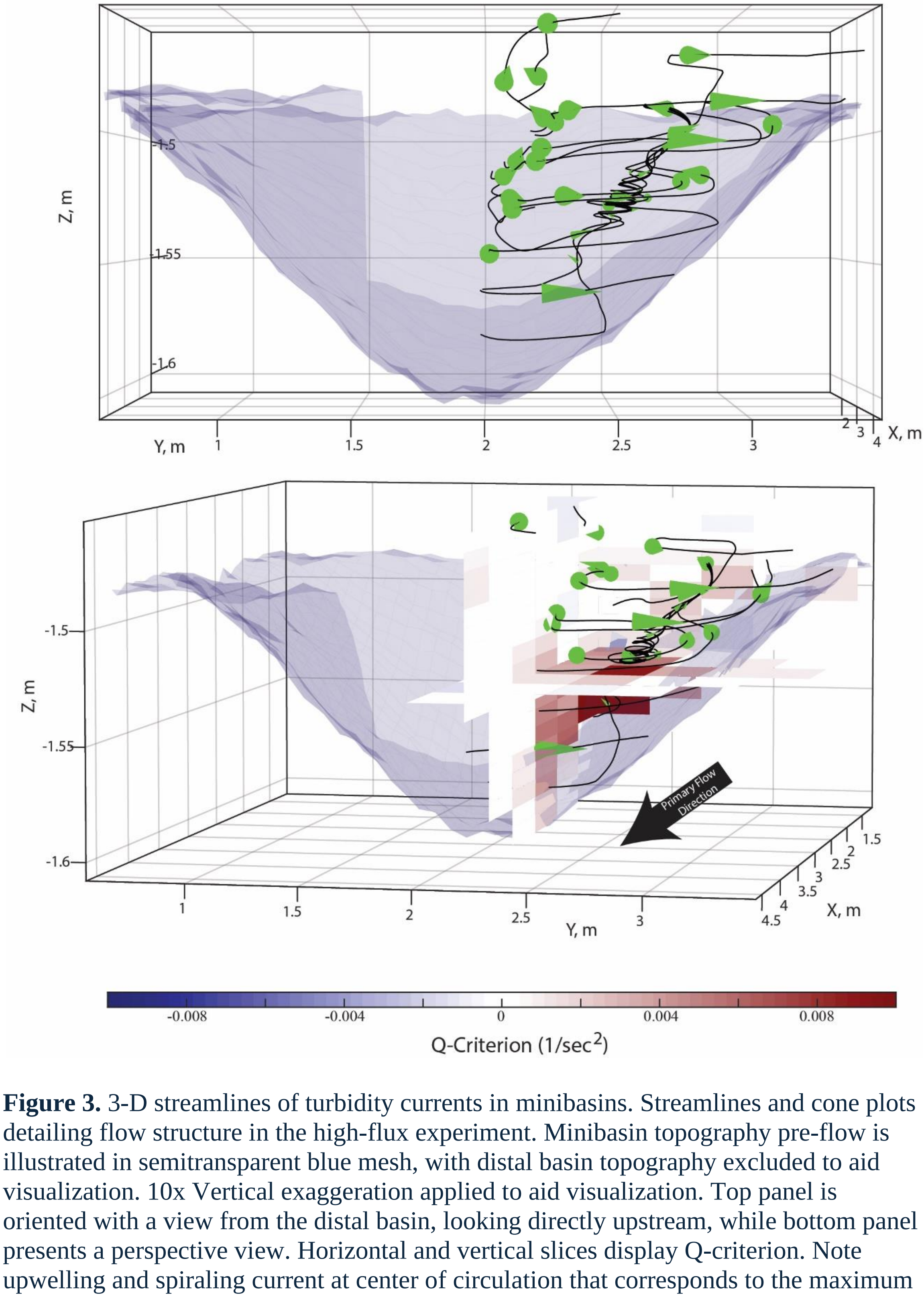

Figure 3. 3-D streamlines of turbidity currents in minibasins. Streamlines and cone plots detailing flow structure in the high-flux experiment. Minibasin topography pre-flow is illustrated in semitransparent blue mesh, with distal basin topography excluded to aid visualization. 10x Vertical exaggeration applied to aid visualization. Top panel is oriented with a view from the distal basin, looking directly upstream, while bottom panel presents a perspective view. Horizontal and vertical slices display Q-criterion. Note upwelling and spiraling current at center of circulation that corresponds to the maximum Q-criterion values.

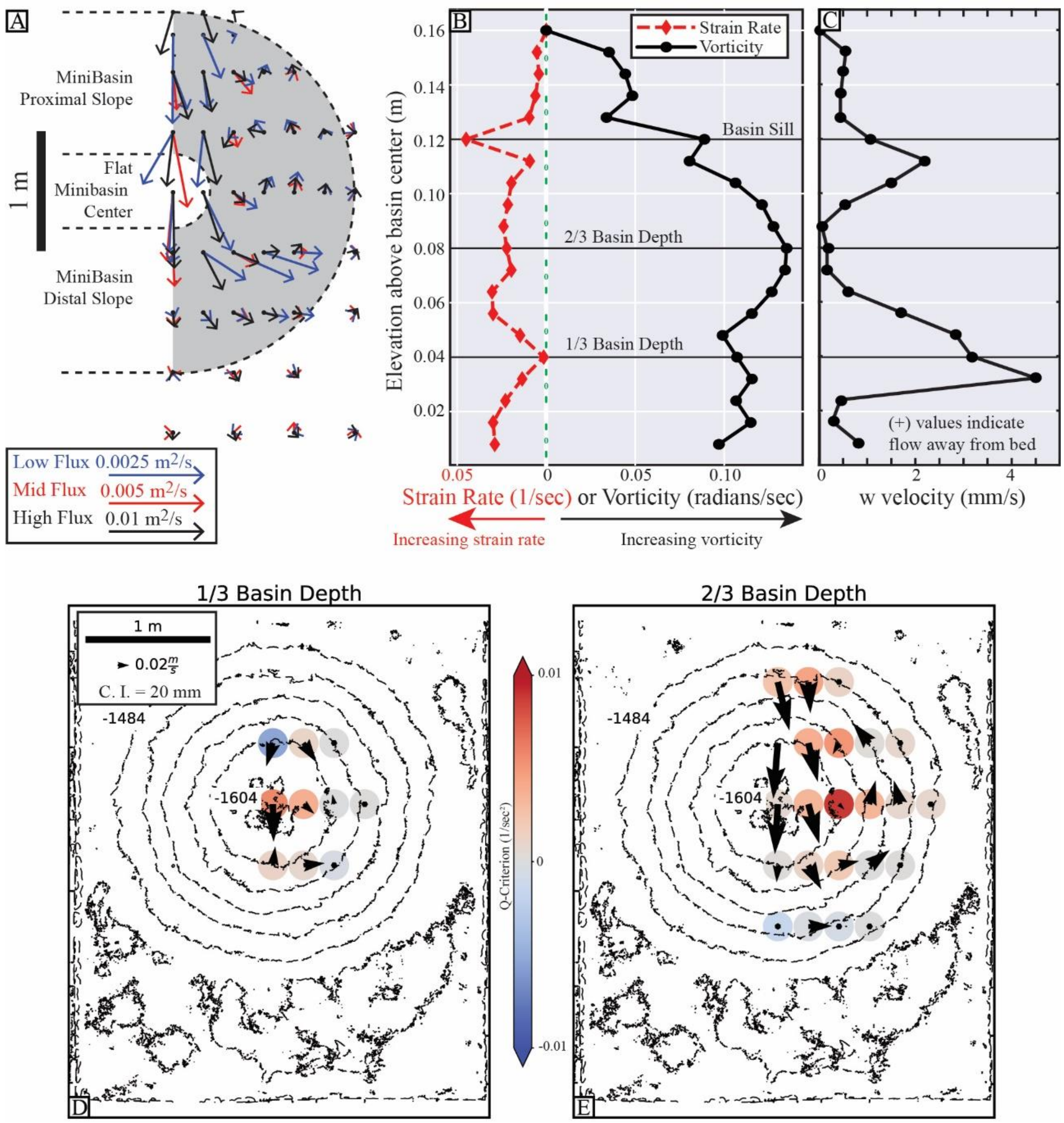

Figure 4. Characterization of minibasin three-dimensional velocity field. A) Vector field of the depth integrated fluid flux with primary flow direction from top to bottom of map. B) Magnitude of flow strain rate and vorticity and C) w component of velocity as a function of elevation above floor of minibasin and lateral position following center of circulation cell, which migrates away from basin center with increasing flow height, as defined by the maximum Q-criterion. C-D) Measurements of Q-criterion (colored dots) for the high-flux experiment along depth slices. Quivers show the u and v velocity components on each depth slice. Contours represent pre-flow topography.

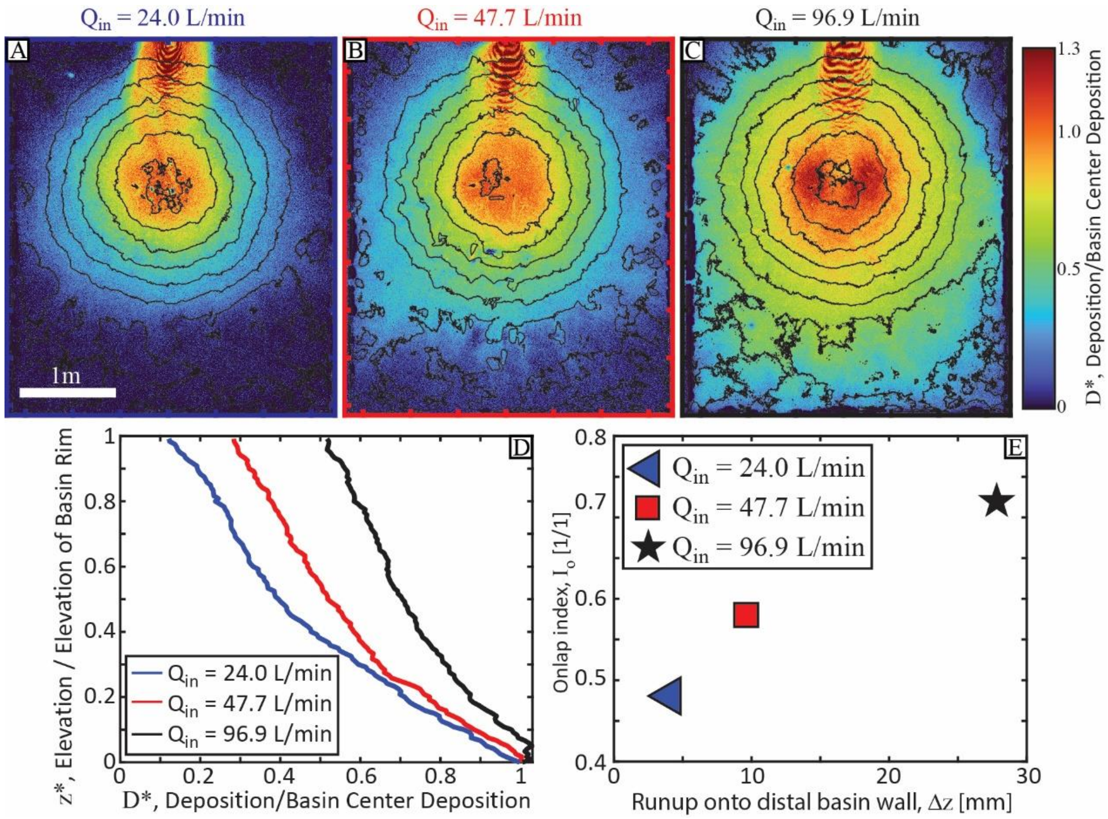

Figure 5. Linking flow fields to sediment deposition. A-C) Sediment isopach maps normalized by minibasin center conditions. Contours represent initial minibasin topography. Primary flow direction in all maps is from top to bottom. D) average sediment deposition profile up minibasin slopes. E) Cross-plot of estimated distal minibasin wall flow runup to onlap index.

SUPPLEMENTARY INFORMATION

Movie S1: Overhead time-lapse of the first flow event in the low-flux experiment (TDWB-21-2). Video shown at 24 times actual speed with frames separated by 4 sec. Tick marks on edge of video occur every 1.0 m.

Link: https://static-content.springer.com/esm/art%3A10.1038%2Fs41467-024-46120-2/MediaObjects/41467_2024_46120_MOESM3_ESM.mov

Movie S2: Overhead time-lapse of the first flow event in the mid-flux experiment (TDWB-21-4). Video shown at 24 times actual speed with frames separated by 4 sec. Tick marks on edge of video occur every 1.0 m.

Link: https://static-content.springer.com/esm/art%3A10.1038%2Fs41467-024-46120-2/MediaObjects/41467_2024_46120_MOESM4_ESM.mov

Movie S3: Overhead time-lapse of the second flow event in the high-flux experiment (TDWB-21-3). Video shown at 24 times actual speed with frames separated by 4 sec. Tick marks on edge of video occur every 1.0 m.

Link: https://static-content.springer.com/esm/art%3A10.1038%2Fs41467-024-46120-2/MediaObjects/41467_2024_46120_MOESM5_ESM.mov

Movie S4: Overhead time-lapse of all three experiments with timing of frames synced to the opening of the valve at the beginning of an experiment that initiated delivery of a slurry to the basin. Video shown at 24 times actual speed with frames separated by 4 sec. Tick marks on edge of video occur every 1.0 m.

Link: https://static-content.springer.com/esm/art%3A10.1038%2Fs41467-024-46120-2/MediaObjects/41467_2024_46120_MOESM6_ESM.mov

ACKNOWLEDGEMENTS

Support from grants to Reece from The Geological Society of America, American Association of Petroleum Geology, and by SEPM, Society for Sedimentary Geology; grants to Straub from The Tulane Carol Lavin Bernick Fund, ExxonMobil, The U.S. - Israel Energy Center funded through the Binational Industry Research and Development Foundation; and grants to Dorrell by the UK Natural Environment Research Council NE/S014535/1.

AUTHOR CONTRIBUTIONS

J.K.R. and K.M.S. conceived the initial idea of the study. R.M.D. developed the experimental sediment mixture. J.K.R. and K.M.S. lead the development of experimental matrix with input from R.M.D. Experimental protocol designed by K.M.S. with input from J.K.R. Experiments were run by J.K.R. with help from K.M.S. All authors contributed to the data analysis and interpretations. J.K.R. wrote the initial draft of the manuscript with edits and additional contributions provided by K.M.S. and R.M.D.

LIST OF REFERENCES

Abd El-Gawad, S., A. Cantelli, C. Pirmez, D. Minisini, Z. Sylvester, and J. Imran (2012). Three-dimensional numerical simulation of turbidity currents in a submarine channel on the seafloor of the Niger Delta slope. *Journal of Geophysical Research: Oceans* **117**.

Almroth, E., A. Tengberg, J. Andersson, S. Pakhomova, and P. Hall (2009). Effects of resuspension on benthic fluxes of oxygen, nutrients, dissolved inorganic carbon, iron and manganese in the Gulf of Finland, Baltic Sea. *Continental Shelf Research* **29**, 807-818.

Altinakar, M., W. Graf, and E. Hopfinger (1996). Flow structure in turbidity currents. *Journal of Hydraulic Research* **34**, 713-718.

Azpiroz-Zabala, M., M. Cartigny, P. Talling, D. Parsons, E. Sumner, M. Clare, S. Simmons, C. Cooper, and E. Pope (2017). Newly recognized turbidity current structure can explain prolonged flushing of submarine canyons. *Science advances* **3**, e1700200.

Babonneau, N., B. Savoye, M. Cremer, and M. Bez (2010). Sedimentary architecture in meanders of a submarine channel: detailed study of the present Congo turbidite channel (Zaiango project). *Journal of Sedimentary Research* **80**, 852-866.

Badalini, G., B. Kneller, and C. Winker in *Deep-Water Reservoirs of the World: Gulf Coast Section SEPM Foundation, 20th Annual Bob F. Perkins Research Conference* (eds Paul Weimer *et al.*) 16-34 (2000).

Bastianon, E. (2018). *Numerical Modeling of Submarine Minibasin Flow and Morphodynamics* PhD thesis, University of South Carolina.

Bastianon, E., E. Viparelli, A. Cantelli, and J. Imran (2021). 2D numerical simulation of the filling process of submarine minibasins: Study of deposit architecture. *Journal of Sedimentary Research* **91**, 399-414.

Beaubouef, R. and V. Abreu (2006). Basin 4 of the Brazos-Trinity slope system: Anatomy of the terminal portion of an intra-slope lowstand systems tract. *Gulf Coast Association of Geological Societies Transactions* **56**, 39-49.

Beaubouef, R. and S. Friedmann in *Deep-Water Reservoirs of the World: Gulf Coast Section SEPM Foundation, 20th Annual Bob F. Perkins Research Conference* (eds Paul Weimer *et al.*) 40-60 (2000).

BOEM. Northern GoM Deepwater Bathymetry Grid from 3D Seismic [Data file]. Retrieved from https://www.boem.gov/oil-gas-energy/mapping-and-data/map-gallery/northern-gom-deepwater-bathymetry-grid-3d-seismic. (2017).

Brunt, R., W. McAffrey, and B. Kneller (2004). Experimental modeling of the spatial distribution of grain size developed in a fill-and-spill mini-basin setting. *Journal of Sedimentary Research* **74**, 438-446.

Cantelli, A., C. Pirmez, S. Johnson, and G. Parker (2011). Morphodynamic and Stratigraphic Evolution of Self-Channelized Subaqueous Fans Emplaced by Turbidity Currents. *Journal of Sedimentary Research* **81**, 233-247, doi:Doi 10.2110/Jsr.2011.20.

Carter, L., R. Gavey, P. Talling, and J. Liu (2014). Insights into submarine geohazards from breaks in subsea telecommunication cables. *Oceanography* **27**, 58-67.

Dorrell, R., S. Darby, J. Peakall, E. Sumner, D. Parsons, and R. Wynn (2014). The critical role of stratification in submarine channels: implications for channelization and long runout of flows. *Journal of Geophysical Research: Oceans* **119**, 2620-2641.

Dorrell, R., M. Patacci, and W. McCaffrey (2018). Inflation of ponded, particulate laden density currents. *Journal of Sedimentary Research* **88**, 1276-1282.

Dubief, Y., and F. Delcayre (2000). On coherent-vortex identification in turbulence. *Journal of turbulence* **1**, 1-22.

Einstein, A. (1926). The cause of the formation of meanders in the courses of rivers and of the so-called Baer's law. *Die Naturwissenschaften* **14**, 223-224.

Ellison, T., and J. Turner (1959). Turbulent entrainment in stratified flows. *Journal of Fluid Mechanics* **6**, 423-448.

Ferguson, R. I., and M. Church (2004). A simple universal equation for grain settling velocity. *Journal of Sedimentary Research* **74**, 933-937.

Fernandez, R., A. Cantelli, C. Pirmez, O. Sequeiros, and G. Parker (2014). Growth patterns of subaqueous depositional channel lobe systems developed over a basement with a downdip break in slope: laboratory experiments. *Journal of Sedimentary Research* **84**, 168-182.

Fukuda, S., M. de Vet, E. Skevington, E. Bastianon, R. Fernandez, X. Wu, W. McCaffrey, H. Naruse, D. Parsons, and R. Dorrell (2023). Inadequacy of fluvial energetics for describing gravity current autosuspension. *Nature Communications* **14**, 2288.

Galy, V., C. France-Lanord, O. Beyssac, P. Faure, H. Kudrass, and F. Palhol (2007). Efficient organic carbon burial in the Bengal fan sustained by the Himalayan erosional system. *Nature* **450**, 407-410.

Gilbert, G., and E. Murphy (1914). *The transportation of debris by running water*. Washington, D.C.: US Government Printing Office.

Graf, W. (1971). *Hydraulics of sediment transport*. Littleton, CO:Water Resources Publications.

Horvath, D., P. Moitra, C. Hamilton, R. Craddock, and J. Andrews-Hanna (2021). Evidence for geologically recent explosive volcanism in Elysium Planitia, Mars. *Icarus* **365**, 114499.

Hudec, M., M. Jackson, and F. Peel (2013). Influence of deep Louann structure on the evolution of the northern Gulf of Mexico Salt Influence. *AAPG bulletin* **97**, 1711-1735.

Islam, M., and J. Imran (2010). Vertical structure of continuous release saline and turbidity currents. *Journal of Geophysical Research: Oceans* **115**, C08025.

Lamb, M., T. Hickson, J. Marr, B. Sheets, C. Paola, and G. Parker (2004). Surging versus continuous turbidity currents: flow dynamics and deposits in an experimental intraslope minibasin. *Journal of Sedimentary Research* **74**, 148-155.

Lamb, M., H. Toniolo, and G. Parker (2006). Trapping of sustained turbidity currents by intraslope minibasins. *Sedimentology* **53**, 147-160.

Jobe, Z., Z. Sylvester, N. Howes, C. Pirmez, A. Parker, A. Cantelli, R. Smith, M. Wolinsky, C. O'Byrne, N. Slowey, and B. Prather (2017). High-resolution, millennial-scale patterns of bed compensation on a sand-rich intraslope submarine fan, western Niger Delta slope. *Bulletin* **129**, 23-37.

Kane, I., M. Clare, E. Miramontes, R. Wogelius, J. Rothwell, P. Garreau, and F. Pohl (2020). Seafloor microplastic hotspots controlled by deep-sea circulation. *Science* **368**, 1140-1145.

Keevil, G., J. Peakall, J. Best, and K. Amos (2006). Flow structure in sinuous submarine channels: Velocity and turbulence structure of an experimental submarine channel. *Marine Geology* **229**, 241-257.

Khripounoff, A., A. Vangriesheim, N. Babonneau, P. Crassous, B. Dennielou, and B. Savoye (2003). Direct observation of intense turbidity current activity in the Zaire submarine valley at 4000 m water depth. *Marine geology* **194**, 151-158.

Komatsu, G. (2007). Rivers in the Solar System: water is not the only fluid flow on planetary bodies. *Geography Compass* **1**, 480-502.

Maharaj, V. (2012). *The effects of confining minibasin topography on turbidity current dynamics and deposit architecture* PhD thesis, University of Texas at Austin.

Masson, D., V. Huvenne, H. De Stigter, G. Wolff, K. Kiriakoulakis, R. Arzola, and S. Blackbird (2010). Efficient burial of carbon in a submarine canyon. *Geology* **38**, 831-834.

Meiburg, E., S. Radhakrishnan, and M. Nasr-Azadani (2015). Modeling gravity and turbidity currents: computational approaches and challenges. *Applied Mechanics Reviews* **67**.

Mitchum Jr, R., P. Vail, and S. Thompson III in *Seismic Stratigraphy II: An Integrated Approach to Hydrocarbon Exploration* Vol. M 39 (eds Orville Roger Berg & Donald G. Woolverton) 53-62 (American Association of Petroleum Geologists, Tulsa, OK, U.S.A., 1977).

Mohrig, D., and J. Buttles (2007). Shallow channels constructed by deep turbidity currents. *Geology* **35**, 155-158.

Nasr-Azadani, M., and E. Meiburg (2014). Turbidity currents interacting with three-dimensional seafloor topography. *Journal of Fluid Mechanics* **745**, 409-443.

Paola, C., K. Straub, D. Mohrig, and L. Reinhardt (2009). The "unreasonable effectiveness" of stratigraphic and geomorphic experiments. *Earth -Science Reviews* **97**, 1-43.

Parker, G., M. Garcia, Y. Fukushima, and W. Yu (1987). Experiments on turbidity currents over an erodible bed. *Journal of Hydraulic Research* **25**, 123-147.

Patacci, M., P. Haughton, and W. Mccaffrey (2015). Flow behavior of ponded turbidity currents. *Journal of Sedimentary Research* **85**, 885-902.

Pirmez, C. *et al.* in *Application of the Principles of Seismic Geomorphology to Continental-Slope and Base-of-Slope Systems: Case Studies from Seafloor and Near-Seafloor Analogues* Vol. Special Publication 99 (eds B.E. Prather *et al.*) 111-143 (SEPM, 2012).

Pohl, F., J. Eggenhuisen, M. Cartigny, M. Tilston, J. de Leeuw, and N. Hermidas (2020). The influence of a slope break on turbidite deposits: an experimental investigation. *Marine Geology* **424**, 106160.

Prather, B., C. Pirmez, and C. Winker in *Application of the Principles of Seismic Geomorphology to Continental-Slope and Base-of-Slope Systems: Case Studies from Seafloor and Near-Seafloor Analogues* Vol. Special Publication 99 (eds B.E. Prather *et al.*) 83-109 (SEPM, 2012).

Satterfield, W., and E. Behrens (1990). A late Quaternary canyon/channel system, northwest Gulf of Mexico continental slope. *Marine Geology* **92**, 51-67.

Sequeiros, O., B. Spinewine, M. Garcia, R. Beaubouef, T. Sun, and G. Parker (2009). Experiments on wedge-shaped deep sea sedimentary deposits in minibasins and/or on channel levees emplaced by turbidity currents. Part I. Documentation of the flow. *Journal of Sedimentary Research* **79**, 593-607.

Sequeiros, O., B. Spinewine, R. Beaubouef, T. Sun, M. Garcia, and G. Parker (2010). Characteristics of velocity and excess density profiles of saline underflows and turbidity currents flowing over a mobile bed. *Journal of Hydraulic Engineering* **136**, 412-433.

Simpson, J. (1982). Gravity currents in the laboratory, atmosphere, and ocean. *Annual Review of Fluid Mechanics* **14**, 213-234.

Soutter, E., D. Bell, Z. Cumberpatch, R. Ferguson, Y. Spychala, I. Kane, and J. Eggenhuisen (2021). The influence of confining topography orientation on experimental turbidity currents and geological implications. *Frontiers in Earth Science* **8**, 540633.

Spinewine, B., O. Sequeiros, M. Garcia, R. Beaubouef, T. Sun, B. Savoye, and G. Parker (2009). Experiments on wedge-shaped deep sea sedimentary deposits in minibasins and/or on channel levees emplaced by turbidity currents. Part II. Morphodynamic evolution of the wedge and of the associated bedforms. *Journal of Sedimentary Research* **79**, 608-628.

Steffens, G., E. Biegert, H. Sumner, and D. Bird (2003). Quantitative bathymetric analyses of selected deepwater siliciclastic margins: receiving basin configurations for deepwater fan systems. *Marine and Petroleum Geology* **20**, 547-561.

Stetten, E., F. Baudin, J. Reyss, P. Martinez, K. Charlier, J. Schnyder, C. Rabouille, B. Dennielou, J. Coston-Guarini, and A. Pruski (2015). Organic matter characterization and distribution in sediments of the terminal lobes of the Congo deep-sea fan: Evidence for the direct influence of the Congo River. *Marine Geology* **369**, 182-195.

Straub, K., D. Mohrig, B. McElroy, J. Buttles, and C. Pirmez (2008). Interactions between turbidity currents and topography in aggrading sinuous submarine channels: A laboratory study. *Geological Society of America Bulletin* **120**, 368-385.

Sylvester, Z., A. Cantelli, and C. Pirmez (2015). Stratigraphic evolution of intraslope minibasins: Insights from surface-based model. *AAPG Bulletin* **99**, 1099-1129.

Talling, P., J. Allin, D. Armitage, R. Arnott, M. Cartigny, M. Clare, F. Felletti, J. Covault, S. Girardclos, and E. Hansen (2015). Key future directions for research on turbidity currents and their deposits, *Journal of Sedimentary Research*, **85**(2), 153-169.

Talling, P., M. Baker, E. Pope, S. Ruffell, R. Jacinto, M. Heijnen, S. Hage, S. Simmons, M. Hasenhündl, and C. Heerema (2022). Longest sediment flows yet measured show how major rivers connect efficiently to deep sea, *Nature Communications*, **13**(1), 4193.

Talling, P., M. Caretigny, E. Pope, M. Baker, M. Clare, M. Heijnen, S. Hage, D. Parsons, S. Simmons, C. Paull, and R. Gwiazda (2023a). Detailed monitoring reveals the nature of submarine turbidity currents. *Nature Reviews Earth & Environment*, 1-17.

Talling, P., S. Hage, M. Baker, T. Bianchi, R. Hilton, and K. Maier (2023b). The global turbidity current pump and its implications for organic carbon cycling. *Annual Review of Marine Science* **16**.

Toniolo, H., G. Parker, V. Voller, and R. Beaubouef (2006a). Depositional turbidity currents in diapiric minibasins on the continental slope: experiments—numerical simulation and upscaling, *Journal of Sedimentary Research*, **76**(5), 798-818.

Toniolo, H., M. Lamb, and G. Parker (2006b). Depositional turbidity currents in diapiric minibasins on the continental slope: formulation and theory, *Journal of Sedimentary Research*, **76**(5), 783-797.

Traer, M., A. Fildani, O. Fringer, T. McHargue, and G. Hilley (2018). Turbidity current dynamics: 1. Model formulation and identification of flow equilibrium conditions resulting from flow stripping and overspill. *Journal of Geophysical Research: Earth Surface* **123**, 501-519.

van Andel, T., and P. Komar (1969). Ponded sediments of the Mid-Atlantic Ridge between 22 and 23 North latitude. *Geological Society of America Bulletin* **80**, 1163-1190.

Violet, J., B. Sheets, L. Pratson, C. Paola, R. Beaubouef, and G. Parker (2005). Experiment on turbidity currents and their deposits in a model 3D subsiding minibasin, *Journal of Sedimentary Research*, **75**(5), 820-843.

Völker, D., T. Reichel, M. Wiedicke, and C. Heubeck (2008). Turbidites deposited on Southern Central Chilean seamounts: Evidence for energetic turbidity currents. *Marine Geology* **251**, 15-31 (2008).

Wahab, A., D. Hoyal, M. Shringarpure, and K. Straub (2022). A dimensionless framework for predicting submarine fan morphology, *Nature Communications*, **13**(1), 7563.

Waltham, D., K. Pickering, and V. Bray (2008). Particulate gravity currents on Venus. *Journal of Geophysical Research: Planets* **113**.

Wang, X., S. Luthi, D. Hodgson, D. Sokoutis, E. Willingshofer, and R. Groenenberg (2017). Turbidite stacking patterns in salt-controlled minibasins: insights from integrated analogue models and numerical fluid flow simulations. *Sedimentology* **64**, 530-552.

Winker, C. (1996). High-resolution seismic stratigraphy of a late Pleistocene submarine fan ponded by salt-withdrawal mini-basins on the Gulf of Mexico continental slope. Paper presented at the *Offshore Technology Conference*, Houston, TX.

Yang, S., Y. An, and Q. Liu (2019). A two-dimensional layer-averaged numerical model for turbidity currents. *Geological Society, London, Special Publications* **477**, 439-454.

CHAPTER 3

Quantifying the interaction of turbidity currents with enclosed minibasin topography in three dimensions: A laboratory study

ABSTRACT

The interplay between seafloor sediment-laden density-driven flows, turbidity currents, and topography helps shape continental margins. However, these interactions are poorly understood, especially those within enclosed depressions termed minibasins. Here novel experiments are presented that quantify fluid and sediment transport dynamics of scaled turbidity current minibasin interactions. For the first time, this study demonstrates that input flow discharge and minibasin length-to-width ratio are leading order controls on sediment trapping. Controls on flow dynamics are quantified by measuring the evolving velocity and sediment transport fields, and minibasin dimensions from bathymetry. Time for sustained flows to reach near equilibrium conditions in 3-D minibasins is much longer than proposed in previous, 2-D, studies. In all 3-D experiments, horizontal flow circulation is observed, but the strength of circulation reduces as the ratio of minibasin length-to-width increases, leading to stagnant or even upstream directed flow near the bed, lowering of near bed shear stresses, and more homogeneous deposits through a reduction in bed reworking. Finally, results detail that fluid detrainment from minibasins significantly reduces sediment fall velocities, severely lowering the sediment trapping efficiency for small or light particles. Results suggest downslope sediment transport and storage in minibasins is likely dominated by evolving flow conditions and basin aspect ratio that influence the fractionation and storage of fine

particulates (e.g., clays), nutrients (e.g., organic carbon) and pollutants (e.g., microplastics).

INTRODUCTION

The structure of many continental margins reflects a competition between the dynamics of mobile substrates [*Hudec and Jackson*, 2007; *Soto et al.*, 2021] and the processes that control sediment transport and deposition [*Mitchell et al.*, 2021; *Pirmez et al.*, 2000; *Prather*, 2003; *Straub and Mohrig*, 2009]. Here, mobile substrates include uncompacted shales [*Dinc et al.*, 2022; *van Rensbergen et al.*, 1999] and salt [*Hudec and Jackson*, 2007] that can undergo ductile deformation, or permanent deformation in a solid material without fracture, if overlain by a critical mass of overburden over geological time scales. The deformation process generates the rise of diapirs that produce depressions across a range of spatial scales at time scales of out to millions of years [*Massimi et al.*, 2007]. The time scale of diapirism bears similarity to that associated with the construction of submarine fans from turbidity currents, where deep-sea sedimentation is influenced by climate and tectono-morphologic controls [*Catuneanu*, 2019; *Talling et al.*, 2015; *Winkler and Gawenda*, 1999]. Some of these depressions are large enough to significantly influence the depositional mechanics of sediment-laden density currents termed turbidity currents [*Ge et al.*, 2020; *Pirmez et al.*, 2012; *Winker*, 1996], which are the primary mechanism for transporting sediment into deep marine settings [*Talling et al.*, 2015; *Talling et al.*, 2022]. For example, horizontal and vertical movement of the mobile Jurassic Louann Salt along the northern passive continental margin of the Gulf of Mexico (GoM) produced depressions with horizontal scales up to tens of kilometers and relief up to hundreds of meters that are often called minibasins [*Hudec et al.*, 2013] (Fig.

1). The geometries of turbidites clearly show that minibasins act as flow obstacles and impact depositional processes [*Beaubouef and Abreu*, 2006; *Prather et al.*, 2012]. Enhanced clastic deposition that occurs due to these obstacles results in economically important geofluid reservoirs [*Mohriak et al.*, 2012; *Stricker et al.*, 2018], and likely impacts the transport, deposition, and preservation of particulate organic carbon, and other nutrients for marine life, as well as microplastics.

In recent years, observations of turbidity currents at field scale have increased due to technological advances [*Pope et al.*, 2022a; *Talling et al.*, 2022; *Vendettuoli et al.*, 2019; *Xu et al.*, 2004]. These observations are revolutionizing our understanding of the fluid and sediment transport mechanics of turbidity currents and provide us with the ability to test theory developed largely from laboratory scale observations. However, we note that most active flow measurements come from settings with limited topographic complexity. We are unaware of any field scale active flow measurements that come from settings with adverse topographic slopes (i.e., slopes that oppose the regional direction of flow), due to mobile geological substrates. However, salt and shale diapirism on many margins create adverse slopes which should impact sediment transport via turbidity currents. These include minibasins resulting from a range of processes that can be found along passive margins of offshore Brazil [*Mohriak et al.*, 2012] and West Africa [*Ge et al.*, 2020], as well as in the eastern Mediterranean [*Mousouliotis et al.*, 2021; *Zucker et al.*, 2020] and North Sea [*Stricker et al.*, 2018]. We also highlight that along some margins mobile substrates produce adverse slopes, but not depressions enclosed in three dimensions (3-D); for example, shale ridges resulting from diapirism [*Prather*, 2003; *Soto et al.*, 2021; *Straub and Mohrig*, 2009]. Other adverse slope settings of interest to turbidity currents may include landslide dams in submarine channels that have recently been documented in the field and proposed to affect carbon and sediment fluxes to deep marine environments [*Pope et al.*, 2022b]. Geometries of turbidites (e.g., variations in thickness and planform aspect ratios) upstream of these types of features provide evidence that topographic features of similar scales act as flow obstacles and influence the depositional mechanics of turbidity currents.

Given the lack of active flow measurements in minibasins and upstream of features like shale ridges, current knowledge of turbidity current interactions with topographic obstacles leverages stratigraphic observations from cores [*Pirmez et al.*, 2012], well-logs [*Alexander and Flemings*, 1995], outcrops [*Marini et al.*, 2016; *Smith*, 2004], and seismic data [*Andresen et al.*, 2011; *Prather et al.*, 2012; *Winker*, 1996]. For example, the Brazos-Trinity system of linked minibasins offshore TX, U.S.A. (Fig. 1) is one of the most studied minibasin systems, with observations leading to several competing models for the progressive filling of minibasins [*Beaubouef and Abreu*, 2006; *Beaubouef*, 2004; *Pirmez et al.*, 2012; *Prather et al.*, 2012; *Winker and Booth*, 2000]. Suggested process based models include: 1) the fill-and-spill [*Winker*, 1996] model where upstream minibasins capture 100% of flow until reaching a spill point and then sending all flow to downstream basins and 2) the flow-stripping [*Badalini et al.*, 2000] model where upper portions of ponded flow in proximal basins can be stripped over confining sills (i.e., topographic highs of minibasin perimeters) and leak to down slope minibasins.

In addition to stratigraphic observations, development of theory has leveraged results from physical experiments performed at reduced scale [*Lamb et al.*, 2004; *Lamb et* *al.*, 2006; *Patacci et al.*, 2015; *Toniolo et al.*, 2006a] and numerical models [*Bastianon et al.*, 2021; *Sylvester et al.*, 2015]. We highlight a set of physical and numerical experiments performed to explore the temporal evolution, or changes over time, of turbidity currents interacting with enclosed minibasins and the trapping potential, or capacity to capture and retain sediment, of these minibasins [*Bastianon et al.*, 2021; *Lamb et al.*, 2004; *Lamb et al.*, 2006; *Patacci et al.*, 2015; *Toniolo et al.*, 2006a]. These were performed in narrow flumes meant to suppress 3-D flow dynamics or utilized 2-D numerical models that solve for down-system and vertical flow structure. Of importance to our study, we note the following observations and theory emanating from these studies. Firstly, the minibasin sediment trapping potential of incoming flows was theorized to equate to the product of the still fluid settling velocity (i.e., velocity at which particles fall through a fluid under quiescent conditions) of sediment in transport and the surface area of the minibasin [*Lamb et al.*, 2006; *Toniolo et al.*, 2006b]. Secondly, observations from experiments supported theory for sustained flow to estimate the time necessary for equilibrium flow conditions (i.e., conditions in which the fluid and sediment transport fields are statistically stationary in time) to be reached. Previously, this has been estimated as the time for a migrating bore, spawned from flow reflection off the distal minibasin wall, to traverse the length of ponded flow in a minibasin [*Lamb et al.*, 2004]. The speed of the bore was assumed to be equivalent to that of the buoyancy-driven shallow water wave, which arises from differences in fluid density. Application of this theory to field scale minibasins suggested that flows entering most minibasins need only be on the order of an hour to achieve equilibrium conditions. Finally, flume experiments identified the development of flow circulation cells, or patterns of fluid flow, in minibasins, with upstream directed flow riding above a lower layer directed down system [*Patacci et al.*, 2015]. However, these studies noted the likely importance of lateral flow expansion in the third dimension, which might influence flow evolution and depositional mechanics in enclosed minibasins. Thus, further investigation of 3-D minibasins is required [*Bastianon et al.*, 2021].

Some 3-D experiments have explored turbidity current-minibasin interactions. These include experiments focused on the architecture of turbidites deposited with ongoing subsidence, but limited velocity data to define flow parameters [*Violet et al.*, 2005] and a set of unpublished studies performed in minibasins of relatively small scale (minibasin width <= 1m) [*Bastianon*, 2018; *Maharaj*, 2012]. The relatively small minibasin widths and depths of these experiments made it difficult to capture the 3-D flow field. This is due to the sample bin width of many acoustic doppler velocimeters, which are more than several decimeters when positioned above minibasins that are of order one decimeter deep [*Maharaj*, 2012]). Further, minibasin side wall slopes in these experiments (between 27-70%) were significantly greater than observed in the field (generally <10%). This is problematic since fluid detrainment scales with ponded area. So, for a given volumetric flow influx rate, shallower sidewalls should result in a decrease to the thickness of deposits and the capability to pond flows [*Dorrell et al.*, 2018].

We present results from a suite of 3-D experiments performed at scales that allow measurement of the full flow field. Experiments were designed with critical dimensionless scales, (i.e., minibasin side wall slopes and minibasin width-to-depth ratios) that compare favorably to field scale minibasins. We aim to investigate how input flow conditions and initial topography affect the depositional mechanics of turbidity currents within enclosed minibasins, with hopes to improve our capacity to model transport and deposition of particulates (including organic carbon and microplastics) in these deep marine environments. To address this lack of understanding in a controlled manner, we designed two sets of experiments. The first set (discharge series) focused on variations in the volumetric discharge delivered to minibasins, with conditions ranging between those that resulted in near complete flow capture in minibasins to conditions that produced significant flow spilling over the distal minibasin rim. The second set of experiments explored how minibasin topography influences the evolution of turbidity currents, specifically the influence of minibasin length-to-width. In both sets of experiments, we explore three key issues:

1) The development of the flow field from initial traverse of a turbidity current across a minibasin to equilibrium conditions for sustained currents and especially the time necessary to reach flow equilibrium.
2) The ability of minibasins to capture input sediment.
3) The 3-D flow structure in minibasins, which impacts sediment transport capacity.

The results emphasize the importance of lateral flow development on the temporal evolution of turbidity currents and sediment trapping potential in minibasins.

EXPERIMENTAL SETUP

Minibasin and Input Flow Design

Our experimental design is motivated by the bathymetry of the northern GoM, specifically scales of depressions extracted from the Bureau of Ocean Energy Management's northern GoM bathymetry grid (12.19 m x 12.19 m cell size) generated from 3-D seismic surveys with an average horizontal resolution of roughly 15 m and an average depth error of 1.3% of water depth [*BOEM*, 2017]. We isolate our analysis to the Fill and Spill region defined in *Steffens et al.* [2003] (Fig. 1) and use standard ArcGIS hydrological toolsets [*Planchon and Darboux*, 2002; *Wang and Liu*, 2006] to identify all local depressions with planform areas more than 1 km^2. Depressions (n=2,324) have scales set by enclosed topography below the elevation of rims (i.e., spill points). We generate distributions for depression diameter-to-depth and depression length-to-width, where depression length is aligned with the regional down-dip flow direction (north-to-south) and width is measured perpendicular to this (Fig. 1B&C). Median depression diameter-to-depth is 145 and ranges from 14–3,400. These widths and depths indicate depression sidewall slopes between 0.1–14% (median = 1.4%). The median depression length-to-width ratio is 1.0 and ranges between 0.1–11.8.

We constructed minibasins within the Tulane University Deepwater Basin (Fig. 2), which is 6 m long, 4 m wide, and 2.2 m deep. Minibasins were carved into a deposit of 300 μm sand residing on a false floor surrounded on the lateral and distal sides by a 0.3 m wide moat with a drainage system to prevent current reflections off deepwater basin walls (Fig. 2). The grain size of the antecedent surface was too coarse (D_{50} ~0.3 mm) to be entrained or transported through saltation as bedload, thus any reworking observed (primarily occurring on the proximal minibasin slope) is associated with sediment deposited from the experimental turbidity currents. Given the constraint of the size of the experimental basin, minibasins were designed with an average diameter of 3 m. Minibasins were either circular in planform (discharge series) or elliptical (aspect ratio series), with all minibasins having a planform area of 7.06 m^2. Work presented here builds on the study of *Reece et al.* [2024], who used results from the discharge series to identify and quantify circulation cells aligned with a horizontal plane that were the result of turbidity currents interacting with circular minibasins. We set the depth of all minibasins to 0.12 m, resulting in a ratio of mean diameter to depth of 25. While on the low end of values observed in the GoM (Fig. 1B), this ratio yields minibasin depths great enough to contain turbidity currents with thicknesses that allow flow properties to be measured. Average minibasin side wall slopes were set at 10%, again on the high-end of measured values, but within the natural spectrum. These values allowed minibasins to have a flat center with an average diameter of 0.61 m. The aspect ratio series is defined by three experiments, with minibasin length-to-width values of 0.5, 1.0, and 2.0, which approximately correspond to the 10th, 50th, and 86th percentiles of the measured GoM depressions (Fig. 1C). After carving the minibasins, the deepwater basin was filled with freshwater to an elevation 0.69 m above the minibasin's rim elevation.

Experimental slurries were mixed in a 2350 L reservoir and pumped to a constant head tank before release into the deepwater basin through a momentum extraction box (457 mm x 610 mm x 762 mm) with an internal screen (0.476 cm diameter drilled holes off set with horizontal and vertical spacing of 0.476 cm) designed to reduce turbulence from currents delivered from the head tank. The exit point of the box was positioned on the lip of the minibasins, allowing turbidity currents to immediately descend into the depressions. Turbidity currents were composed of fresh water at room temperature mixed with aluminum oxide particles, which allows us to generate experiments more in line with behavior of natural systems at these laboratory scales, as opposed to prior silica-based sediment slurries that were inefficient at delivering sediment rich flows to the center of minibasins. Aluminum oxide has a density, ρ_s, of 3,950 kg/m^3; this high sediment density, relative to quartz, generates significant excess current density relative to the ambient fluid at low sediment concentrations [*Fukuda et al.*, 2023]. At experimental scale, the greater driving force supports enhanced flow velocity, production of turbulence, and thus sediment suspension. This helps to drive flows into the minibasins with minimum deposition on the proximal slopes. We performed a point count of 100 particles of the sediment with a 100x resolving microscope to characterize the size distribution of the sediment used in the experiments. This resulted in a *D*50 equal to 14 μm, which is 1 μm more than reported by the sediment manufacturer (Fig. 3). Flows were released into the basin with a volumetric concentration of 0.01, yielding a 2.95% excess density relative to the ambient fluid. A small amount of sodium hexametaphosphate and calcium carbonate (ratio 33:7) was added to the slurry to limit sediment flocculation, or the amalgamation of small particles into larger clumps of particles [Dorrell, R., personal communication, June 10, 2020]. Currents had an initial thickness of 48 mm, yielding a ratio of minibasin depth to initial flow height of 2.5. This ratio is poorly defined for field-scale systems and likely varies over several orders of magnitude. However, measurements from the Brazos-Trinity system, using the *BOEM* [2017] bathymetric map of the northern GoM, suggest our experimental ratio is within the distribution of field scale systems. Specifically, the present depth of Brazos-Trinity minibasin II is 83 m, while the main feeder channel to the minbasin is 38 m deep. A densimetric Froude Number, Fr_d, describes the relative ratio of inertial to gravitational forces in a flow and is equal to

$$Fr_d = \frac{\bar{u}}{\sqrt{RgCH_c}}, \qquad \text{[EQ. 1]}$$

where $\bar{u}$ is the depth averaged flow velocity, R is the submerged specific gravity of sediment, C is the sediment concentration, g is gravitational acceleration, and H_c is the flow thickness. Fr_d was set at 1.1 for all flows entering the experimental minibasins, based on estimates for field scale currents descending typical minibasin sidewall slopes [*Parker et al.*, 1987] and numerical experiments that link Fr_d to the morphology of minibasin filling fans [*Wahab et al.*, 2022].

Input flow discharge, Q_{in}, was designed to produce specific values of the fraction of sediment released that would be trapped in the minibasins. This was achieved using theory developed by *Lamb et al.* [2006] that predicts the fluid and sediment discharge for currents that deposit 100% of their sediment within a minibasin (i.e., 100% trapping capacity). Currents that deposit 100% of their sediment within a minibasin detrain, or vertically expel, fluid out of the top interface of the flow. In this framework, the maximum detrainment discharge, $Q_{d,max}$, for a minibasin can be estimated as

$$Q_{d,max} = w_s A, \qquad \text{[EQ. 2]}$$

where w_s is the terminal settling velocity of the median particle size in still fluid and A is the planform area of a minibasin. The discharge series had ratios of $Q_{in}/Q_{d,max}$ of 0.95, 0.47, and 0.23, corresponding to flows with Q_{in} equal to 24.0, 47.7, and 96.9 l/min, for the low-, mid-, and high- flux experiments, respectively. The duration of each experimental release was 1,800 sec (30 min). Thus, fluid volumes delivered into experiments, V_{in}, were 720, 1431, and 2907 l for the low-, mid-, and high- flux experiments, respectively. The input discharge values coupled with a mean flow velocity, set by the flow height and Fr_d condition, determined input flow width, yielding flows that were 65, 130, and 260 mm wide for the low-, mid-, and high- flux experiments, respectively. The range of $Q_{in}/Q_{d,max}$

in the discharge series suggested that all flows should deposit 100% of their sediment in the minibasins. However, as detailed below, the trapping efficiency of the minibasins was less than predicted from previous experimental studies. Thus, the specific values of Q_{in} explored were set, through observations in pilot experiments, to facilitate a deliberate transition through the flow filling (low-flux), striping (mid-flux), and spilling (high-flux) sequence. All flows in the aspect ratio series had Q_{in}:$Q_{d,max}$ equal to 0.47. This ratio used a Q_{in} of 47.7 l/min (V_{in} for the 30 min flow thus equaled 1431 l) and when coupled with a mean flow velocity, set the input flow width of 130 mm.

Data Collection

For each experimental condition two sustained turbidity currents were released into the basin. Initial basin topography was mapped with a 1 KHz long range Keyence displacement laser connected to a data logger. This laser was attached to a measurement carriage on top of the deepwater basin and could move in the three Cartesian directions. Mapping was performed with the laser positioned at a fixed vertical height for all experiments (Fig. 2). This system allowed topography to be gathered with a vertical precision less than 0.25 mm. Topography was gathered with x (downstream) and y (cross-stream) node spacing, or distance between measurement points in a grid, of 5 mm. Topography was also collected following each flow event, allowing the fraction of input sediment trapped in minibasins to be estimated.

Measurements of current velocity were collected using a Nortek Pulse-Coherent Acoustic Doppler Profiler (PCADP) connected to the measurement carriage. This device recorded profiles of the 3-component velocity field within 8 mm tall bins at 1 Hz, which is 1/6 the initial height of the incoming flow. The horizontal diameter of bins varied as a function of distance from the probe but were 0.32 m at the elevation of the minibasin rim and 0.44 m at the elevation of the minibasin floor. We limit our analysis of PCADP data to bins that were fully above the sediment surface. For each experimental condition, the PCADP was positioned over the center of the minibasin for the full duration of the first flow event (flow 1). During the second half of the second flow event (flow 2), the PCADP was deployed to locations on a horizontal grid that covered the river-left hand side of the basin. This grid contained between 27 – 48 nodes, depending on the experiment, and the PCADP was situated over each node for a duration of 25 seconds.

Measurements of suspended sediment concentrations were collected near the minibasin center during flow 1 of each experimental condition, immediately port-side of the PCADP sample cone. The siphon rack was positioned at a location just outside of the sample volume of the PCADP and removed from the basin during topographic mapping. Turbid flow samples came from a set of 10 vertically stacked siphons of 2 mm inner diameter, with 15 mm spacing between siphons and the basal siphon residing 10 mm above the minibasin floor. Approximately 500 mL of turbid flow was extracted with each siphon, from which a measurement of sediment concentration was made by evaporating off the fresh water. Four profiles of concentration were collected for each experiment. Each extraction took 75 seconds, with collection of each profile beginning 90, 210, 405, and 1,560 seconds into a flow event. The diameter and length of tubing used to extract samples resulted in a lag of 15-25 sec between fluid entering and exiting a siphon line.

Overhead images captured the evolution of the flow field for the duration of each experiment at a frequency of 0.25 Hz. To characterize the flow field in equilibrium conditions, a pulse of red dye was injected into the input current at 900 sec into each experiment. The volume of the dye was approximately 250 ml and the injection duration was approximately 2-3 seconds.

Finally, to measure the height of the turbid cloud a striped vertical rod was placed near minibasin center, but outside the PCADP measurement field on the starboard-side of the flat basin floor. Underwater video was collected with a GoPro camera positioned over the river left, or port-side, moat at a downstream distance aligned with minibasin center. The center of the field of view was positioned on the measurement rod, with the elevation of the camera just above the minibasin rim.

RESULTS

Observations of Current-Minibasin Interactions

We start by characterizing the temporal and spatial evolution of the experiments using overhead images and video stills from the GoPro camera. In each experiment, a turbidity current with a pronounced head descends from the entrance box to minibasin center, which is followed by a thinner current body (Fig. 4). We use a timeseries of frames from the GoPro video to quantify the height of the turbid cloud. This is done using a white color threshold applied over pixels that span the measurement rod (Figs. 5&6). As the flow fronts traversed the minibasins they widened but did not initially fill the full width of the minibasins (Fig. 2). When the current heads reached the distal minibasin slope, flow reflection generated an upstream migrating bore, or waves with a steep front that move rapidly upstream against the primary current; this inflated the turbid clouds at minibasin center to a thickness approximately equal to minibasin depths. These reflections propagate upstream, but also laterally, widening the flows. After the reflections reached the proximal minibasin slopes, the minibasins progressively filled with turbid flow. Apparent equilibrium conditions were eventually reached when input flow was balanced by a combination of clear water detrainment out of the top interface of a current, turbid flow overspilling the full perimeter of the minibasins and focused flow overtopping the distal minibasin rim. After this time, the top surface of the turbid clouds throughout much of the minibasins were placid, indicating low velocity flow with limited mixing with the above ambient fluid, except for a region that extended from the entrance box down the proximal slopes. These entrance flows had more pronounced turbulent mixing over a distance that scaled with the input flux and inversely with minibasin *L*/*W*. We use the terminology of *Lamb et al.* [2006] and separate the turbulent “inlet flow” from the more placid “ponded flow”. Overhead imagery suggests equilibrium flow conditions were reached within the first 900 ± 20 sec for all conditions. Note that we estimate an error in our interpretations from overhead imagery of ± 20 sec. This is estimated from the 4 second image collection increment and an ambiguity in differentiating characteristics like turbulence levels and flow color on individual images.

Flow Conditions at Minibasin Center

Next, we characterize the temporal evolution of conditions at minibasin center utilizing measurements of the velocity and sediment concentration fields (Figs. 5 & 6). Starting with velocity conditions, we focus on the magnitude of the down-basin, *u*, component. Velocity measurements collected with pulse-coherent acoustic doppler profiles have unknown uncertainties [*Shcherbina et al.*, 2018]. However, measurements of velocity, at a given flow elevation, during equilibrium conditions are generally consistent $\pm$ 2 mm/s. Some of these fluctuations are likely linked to flow turbulence and as such, suggest a measurement precision < 2 mm/s. The temporal evolution of velocity profiles in all experiments follows a general trend. First, profiles capture the propagation of thick current heads, relative to trailing current bodies, pre-reflection. Arrival of the upstream migrating bore is generally coincident with upstream directed flow for some period, but the location and duration of this return flow varies with Q_{in} and minibasin shape. This is followed by the development of near equilibrium velocity conditions in most experiments.

In the discharge series, the lowest Q_{in} experiment (Fig. 5A) had the shortest period of upstream directed flow, and this was contained in the lower portions of the flow (bottom 50 mm). Equilibrium velocity conditions appeared to be reached at minibasin center fairly rapidly during this experiment (~200$\pm$30 sec). Note that the associated error (i.e., $\pm$30 sec) is due to ambiguity with interpretations of turbulent flow oscillations observed in all collected datasets. The mid flux experiment (Fig. 5B) also had a duration where return flow was observed low in the flow (100-125$\pm$30 sec). This was followed with a period characterized by a lower layer of down-system directed flow and an upper layer characterized by a return flow (250-650$\pm$30 sec). Velocity conditions stabilize ~650$\pm$30 sec into this experiment. The high flux experiment (Fig. 5C) has a similar temporal evolution as the mid flux condition; however, return flow was never observed at the base of this flow and equilibrium conditions were reached ~400$\pm$30 sec into the experiment.

In the aspect ratio series, the $L = 2W$ experiment (Fig. 6A) has no significant upstream directed flow in the first half of the experiment. After the propagation of the current head and upstream migrating bore, we observe a period of high velocities, specifically high in the flow column (225-450±30 sec). After this a gradual evolution of the flow occurs for the remainder of the experiment, with velocities decreasing low in the flow and eventually flipping their orientation, resulting in a weak and pulsing return flow low in the current. Sitting above the return flow is a layer of down-system directed flow, with peak velocities near the elevation of the minibasin rim. The $L = 0.5W$ experiment (Fig. 6C) was characterized by the propagation of a current head and as expected, a short period of body flow before arrival of the reflection. This was followed by a period with reduced velocities near the bed and a return flow higher up. Velocity conditions stabilized ~400±30 sec into this experiment, with the full depth range characterized by down-system flow.

Next, we explore the evolving sediment concentration field. Our data captures the evolution of the concentration field over the first 500 seconds with three profiles and utilizes an additional 4th profile, collected 1,560 sec into each experiment, to characterize an assumed equilibrium field. In all experiments we observe stratified flow with sediment concentration decreasing with distance from the bed. Concentrations increase along with experimental run-time. Notably, the largest concentration increase occurs between the first and second measurement period, which roughly corresponds to before and after the arrival of the upstream migrating bore. While turbidity currents in all experiments had the same input concentration, concentrations measured at minibasin center increase with Q_{in} (Fig. 5). Concentrations are similar in the $L = 2W$ and circular experiments; however, the $L = 0.5W$ experiment has noticeably lower concentrations (Fig. 6). A comparison of profiles at time 3 (evolving flow) and 4 (~equilibrium), suggests that time to an equilibrium concentration field decreases with increasing Q_{in} (Fig. 5). Time to an equilibrium concentration field also appears to decrease as minibasins become short relative to their width (Fig. 6).

Planform Flow Evolution

Imagery acquired during dye releases aid characterization of equilibrium conditions (Fig. 7). The front of the dyed flow traverses the proximal minibasin slope with minimal widening. With further propagation into the minibasins a bifurcation of the dye front occurs, with dye eventually routed laterally into twin circulation cells and back to the proximal minibasin slope. Residence time of dye in the inlet flow was noticeably less than in ponded flow. To explore this, we calculate the average red color intensity, $\overline{r^*}$, of each pixel in the minibasin for the last 900 sec of each experiment. Using a technique similar to the Normalized Difference Vegetation Index (NDVI) measurement to identify vegetation in remote-sensing applications [*Esposito et al.*, 2018; *Tucker*, 1979], the red color intensity of an individual pixel is quantified as

$$r^* = \frac{R-B}{R+B}, \qquad \text{[EQ. 3]}$$

where R and B are values of the red and blue color bands of a pixel, which span 0-255. Maps of $\overline{r^*}$ help distinguish the inlet from ponded flow, which were separated by fairly sharp boundaries.

We observe that the downstream extent of inlet flow conditions scales with Q_{in}. For the highest flux condition, the inlet flow extends over the distal minibasin rim (Fig. 7C), suggesting focused discharge of sediment out of the minibasin, Q_{out}. The residence time of flow in the ponded regions appears to inversely scale with Q_{in}, as $\overline{r^*}$ values in the ponded flow decrease with increasing Q_{in}. In the aspect ratio series, the dye front rapidly widens to the full width of the minibasin in the $L = 2W$ experiment and thus the full areal extent of the minibasin is filled with red dye upon the front reaching the distal minibasin rim (Fig. 7D). Eventually, red dye is replaced with new white influx sweeping from proximal to distal regions; this is interpreted as an inlet flow that fills the full lateral extent of the proximal minibasin slope. In contrast, the dye front in the $L = 0.5W$ experiment descends into the minibasin with minimal widening, before a reflection that highlights prominent circulation cells (Fig. 7E). Like the circular minibasins, the $\overline{r^*}$ map highlights an inlet flow that extends nearly to minibasin center and strong ponding along lateral minibasin slopes.

Equilibrium Flow Conditions

We explore how input conditions and minibasin shape influence fluid and sediment transport properties after approximate equilibrium conditions are reached. Values are reported for equilibrium velocity, concentration, and key dimensionless numbers that describe the fluid and sediment transport fields. Measurements come from 1,560-1,640 sec into each experiment, when the fourth and last concentration profile was collected. Starting with the structure of the velocity field, we compare profiles at minibasin center that are normalized by the maximum velocity in each profile. In the discharge series (Fig. 8A), the mid and high flux experiments, excluding their obvious magnitudes, share similar flow structure. These flows have a rapid increase in velocity with distance from the bed and then maintain similar values for most of the flow height. Peak velocities in these experiments are found in the upper third of the flow. In contrast, the low discharge experiment has relatively low velocity in the lower third of the flow. Above this a pronounced high velocity region is observed in the middle third of the flow, before a decreasing trend is observed in the upper third of the minibasin. In all of these experiments the height of the velocity maximum, relative to the flow height, is elevated in comparison to unconfined flows, where the velocity maximum is typically at an elevation that is ~30% of the total flow height [*Sequeiros et al.*, 2010]. In the aspect ratio series (Fig. 8B), a clear trend is observed with increasing minibasin L/W. The $L = 2W$ experiment has low velocity values with limited structure up to the top third of the flow. Here, velocity values rapidly increase, reaching peak values near the elevation of the minibasin rim. This result is in line with quasi 2D studies performed in flumes that report extreme elevation of the u_{max}. For example, a study by *Sequieros et al.* [2009] in a pseudo-minibasin that was 9 m long and 0.45 m wide (i.e., L/W = 20) had a similar velocity profile as our L = 2W experiment. Moving to the circular and then the $L = 0.5W$ experiment, we see a trend of decreasing height of the velocity maximum and greater shear near the bed.

Next, we present concentration profiles, normalized by the near bed values, to explore differences in stratification between experiments (Fig. 8C-D). While significant differences exist in the velocity structure between experiments, we note that the normalized structure is remarkably similar in all experiments.

Characterization of Flow Structure and Competing Forces

We report several dimensionless numbers to characterize flow structure and competing forces in turbidity currents (Fig. 9). We start by calculating the ratio of the height of the velocity maximum, H_{umax} (Table 1), to the depth of the minibasin, D (Table 1), measured between the basin floor and sill. Low values of this ratio link to conditions with significant shearing of the flow near the bed and vice versa for high values. We note that measurements of the turbid cloud height obtained from analysis of the GoPro footage are similar to the depth of the minibasins, suggesting H_{umax}/D approximately equals H_{umax}/H_c. However, a portion of the top of the turbid cloud displays relatively stagnant flow. Given this, we follow established methods and use the integral length scale to estimate H_c as

$$H_c = \frac{\left(\int_0^\infty u dz\right)^2}{\int_0^\infty u^2 dz}. \qquad \text{[EQ. 4]}$$

This yields flow heights that are similar to, but always less than, minibasin depths (Table 1).

Experiment	H_{umax} (m)	H_c (m)	D (m)
Circular Mid-Flux	0.0766	0.1111	0.12
Circular Low-Flux	0.0692	0.0829	0.12
Circular High-Flux	0.0913	0.1170	0.12
Elongated L = 0.5W	0.0564	0.1027	0.12
Elongated L = 2W	0.1261	0.0772	0.12

Table 1. Measurements of the height of velocity maximum during equilibrium conditions (H_{umax}), turbidity current flow height estimated with integral length scale (H_c), and minibasin depth, measured from basin floor to sill (D).

In the discharge series, we observe a complex evolution of H_{umax}/D in the first 400 to 600 sec. This includes an initial rapid increase in H_{umax}/D to values between 0.5-0.9, followed by a period where peak velocity elevations fall to 0.2-0.5 of D. After this, H_{umax} again increased and equilibrated at values ranging between 0.5-0.8 of D. Evolution of H_{umax}/D is more complex in the aspect ratio series. The L/W = 2 experiment is characterized by an increase in H_{umax}/D over the first 380 sec to a value ~0.7. Between

380-580 sec H_{umax}/D drops and oscillates between 0.4-0.7 and then rapidly increases to a value greater than 1 for the remainder of the experiment. In contrast, H_{umax}/D rapidly increases in the first 200 sec of the L/W = 0.5 experiment before stabilizing at ~0.5.

Next, we report bulk Richardson numbers, Ri_B. This dimensionless number compares forces that work towards stable stratification of flows to forces that induce turbulent mixing and is equal to

$$Ri_B = \frac{1}{Fr^2} = \frac{RgCH_c}{\bar{u}^2}. \quad \text{[EQ. 5]}$$

Ri_B is calculated using timeseries of depth average concentration from our siphon system. In all experiments the current body pre-reflection has Ri_B less than 1, which corresponds to supercritical Fr_D, a flow condition where the flow velocity is greater than the shallow water wave speed. For the discharge series, Ri_B values rapidly increase after the arrival of the upstream migrating bore and then settle to an approximately steady value after ~600 $\pm$30 sec. For the aspect series, a similar temporal evolution of Ri_B was observed in the L = 0.5W experiment. The evolution of Ri_B in the L = 2W experiment was more complex; specifically due to the development of return flow in the second half of the experiment that resulted in unstable Ri_B, through singularities in Eq (5) when $\bar{u} \rightarrow 0$.

The Rouse number, p [*Rouse*, 1939], characterizes the capacity of currents to suspend sediment and is equal to

$$p = \frac{w_s}{ku^*}, \quad \text{[EQ. 6]}$$

where k is von Kármán's constant (~0.41), a dimensionless constant used in fluid dynamics, and u* is the shear velocity of the flow. Similar to *Altinakar et al.* [1996], we estimate $u*$ for turbidity currents by fitting an equation that describes the logarithmic increase in velocity above a bed for a shearing flow to our data

$$u(z) = \frac{u^*}{k} ln\left(\frac{z}{z_0}\right). \qquad \text{[EQ. 7]}$$

Specifically, we fit EQ. 7 to data from the lowest 4 velocity bins, which always reside below H_{umax}. The settling velocity, w_s, is calculated for particles in the flow using the *Ferguson and Church* [2004] method. In the discharge series p values rapidly stabilize just below 10^{-1} for the mid and high flux conditions. While the first half of the low flux condition follows a similar evolution, the second half of the experiment is characterized by oscillation in p with peaks up to ~0.7, suggesting a transition to sediment being transported lower in the flow. In the aspect ratio series, the $L = 0.5W$ experiment follows a similar trend to the high and mid flux experiments. Like the low flux experiment, the $L = 2W$ experiment displays oscillations in p, beginning ~600 sec into the experiment. Oscillations strengthen as this experiment progresses, reaching values greater than 1.

Dimensionless numbers that characterize the equilibrium fluid and sediment transport fields show clear gradients as a function of Q_{in} and minibasin L/W. We observe that the height of the velocity maximum, relative to minibasin depth, systematically increases as a function of Q_{in} and L/W (Fig. 10A), suggesting a systematic change in the shear profile near the bed. Bulk Richardson numbers in the discharge series indicate that the strength of stratification relative to turbulent mixing decreases as minibasin influx increases. In the aspect ratio series, Ri_B values show a strong positive correlation with increasing minibasin L/W; with extreme suppression of mixing in the $L = 2W$ experiment (Fig. 10B). With regard to sediment suspension capacity as measured through p, we note non-linear trends as a function of Q_{in} and minibasin L/W. Our low discharge and high L/W experiments have p values above 0.2, suggesting relatively lower suspension capacity, while all other experiments have similar p values, which are less than 0.07 (Fig. 10C).

Minibasin-Wide Flow Structure

At each site visited by the PCADP during the second half of flow 2, we calculate the temporally averaged depth integrated fluid flux in the x (u-velocity component) and y (v-velocity component) directions with z as the vertical direction

$$q_u = \int_0^{H_c} u dz, \quad \text{[EQ. 8A]}$$

$$q_v = \int_0^{H_c} v dz. \quad \text{[EQ. 8B]}$$

Temporal averaging was done over the duration that the PCADP sampled each site. We visualize these fields using vectors that scale with the direction and magnitude of flux (Fig. 11). As first highlighted in a study by *Reece et al.* [2024], we observe circulation cells where flow moving up distal minibasin slopes is directed laterally away from the minibasin center line. Minibasin slopes continue to affect the flow direction, resulting in circulating cells that include up-system directed flow along a portion of the lateral minibasin slopes. The center of these cells is laterally located away from minibasin center. When normalized by input flux, the shape of the circulation cells is remarkably similar in all experiments. To compare the shape of circulation cells in the aspect ratio series, we transform the location of our measurements into polar coordinates (Fig. 12). Viewing the flow field in polar coordinates reveals that the magnitude of current flux in the circulation cells is generally higher in the $L = 0.5W$, compared to the $L = 2W$

experiment. We quantify this difference by calculating the average horizontal flow circulation, Γ. From Stoke's Theorem, horizontal circulation within an area is calculated as the integral of vorticity within a closed contour. Here this is calculated for a discrete set of points as

$$\Gamma = \sum_{i=0}^{n} \overrightarrow{\Omega_i}\, A_b. \qquad \text{[EQ. 9]}$$

Where $\overrightarrow{\Omega_i}$ is the vertically averaged flow vorticity at a node *i*, calculated from the asymmetric part of the velocity gradient tensor as

$$\Omega = \tfrac{1}{2}[(\delta v/\delta x) - (\delta u/\delta y)], \qquad \text{[EQ. 10]}$$

and A_b is the discrete area associated with a velocity node (*x*-sample spacing times *y*-sample spacing). The horizontal circulation calculation is done for the closed contour defined by the basin bisect line and the river left rim of the minibasin (i.e., all *n* nodes that fall within each minibasin). As the sum of the areas of the measurement nodes and the rules used to define the closed contour are the same in all experiments, we can directly compare the strength of circulation induced by the length-to-width ratio of a minibasin. We calculate the circulation of the $L = 2W$ and $L = 0.5W$ experiments as 0.0027 and 0.0043 m^2/s, respectively.

Minibasin Sediment Trapping Capacity

Sequential maps of topography before and after each flow event allow us to quantify the fraction of sediment trapped in the minibasins (Figs. 13&14, Table 2)

$$F_S = \frac{V_{sediment,\ in\, minibasin}}{V_{sediment,\ in\, mapped\, region}} \qquad \text{[EQ. 11]}$$

This represents a maximum trapping fraction as some sediment delivered to the minibasins (flux delivered to the entrance box minus flux to deposition in the entrance box) spilled over the full perimeter of the minibasin rims and ended up in the basin drains. The first experiment performed was the high flux circular condition, which was designed with a sediment input flux near equal to the sediment trapping potential, calculated with the equation proposed by *Lamb et al.* [2006], EQ. 2. However, our results suggest that at most 75% of the input sediment to this experiment was trapped in the minibasin (Table 2). Estimates for the sediment fraction trapped in the mid and low flux experiments are 85% and 98%, respectively (Table 2). Note that reported values of trapped sediment fraction (Table 2) are estimated due to a visibly small and unmeasurable amount of sediment loss to perimeter drains. Reported values suggest that near complete sediment trapping does not occur until flow influx drops to approximately one-quarter of that proposed from earlier theory. The elongated minibasins have sediment trapping fractions similar to the mid flux circular case, suggesting that minibasin planar geometry does not strongly influence sediment trapping potential.

Experiment	F_S
Circular Mid-Flux	85%
Circular Low-Flux	98%
Circular High-Flux	75%
Elongated L = 0.5W	85%
Elongated L = 2W	85%

Table 2. Estimates of the fraction of sediment trapped in each experimental minibasin (F_S).

DISCUSSION

Time to Equilibrium Flow Conditions in Minibasins

The time necessary for flow properties to stabilize in minibasins has implications for the structure of minibasin filling turbidites. For minibasins with quasi-steady (properties changing slowly over time approaching a steady state) input fluxes that require significant time to reach equilibrium within the enclosed topography, turbidites will record the flow development in their lamination (i.e., strata layering at scales of mm's to cm's) and sedimentary structures. In contrast, flows that rapidly reach equilibrium should deposit more homogeneous beds. *Lamb et al.* [2004] also noted that the shape of turbidites in minibasins differ for sustained flows in comparison to surge like flows that never reach equilibrium.

Prior work explored the time to flow equilibrium in 2-D experiments. *Lamb et al.* [2004] proposed a method to estimate a setup time for equilibrium conditions, defined as the time for a migrating bore to traverse the extent of ponded flow in minibasins. This bore developed due to the reflection of the head of a turbidity current off the distal minibasin slope, similar to that observed in our experiments (Figs. 2&4). The speed of the migrating bore was estimated with the shallow water wave equation

$$c_b \cong \sqrt{RgC\Delta H_b}, \qquad \text{[EQ. 12]}$$

where ΔH_b is the height of the bore. If one estimates the extent of ponded flow as the full length of the minibasin, L, an equilibrium time can be estimated as

$$T_b = \frac{L}{c_b}. \qquad \text{[EQ. 13]}$$

We test this theory for our experiments, focusing first on the circular mid-flux condition. We use overhead imagery to estimate the time into this experiment that the migrating bore, spawned from reflection off the distal slope, reaches the proximal rim as

200±20 s. We apply the *Lamb et al.* [2004] formulation to estimate this time. To accomplish this, we use a range of plausible ΔH_b measured from the GoPro footage (0.01-0.02 m) and C measurements from the first profile of the experiment (C = 0.001 – 0.002). With this, we estimate the bore to reach the proximal slope at 124 – 212 s. However, we note that at this time the concentration field is not equilibrated, nor is the velocity field (Fig. 5). The second concentration profile (210 – 285 s) is significantly different from the third profile (405 – 480 s) and the velocity field does not stabilize until at least 600 s into the experiment.

The difference between the *Lamb et al.* [2004] theory and our observations at minibasin center can be explained. While the Lamb et al. [2004] theory produced a reasonable estimate for 2-D minibasins, we highlight several limitations to the theory, or at least simplifications to the formulation. One limiting factor is that it does not account for the time associated with the initial propagation of the current front across the minibasin, T_p, prior to the bore being spawned. This can be estimated as

$$T_p = \frac{L}{u_p} \qquad \text{[EQ. 14]}$$

where u_p is the depth averaged current velocity in the down-basin direction during the initial flow traverse (i.e., before generation of bore). Next, theory that predicts bore speeds [*Bonnecaze et al.*,1993] considers the thickness and velocity of the current during this initial propagation, here defined as H_p and u_p, respectively, as well as the thickness of the inflated flow post reflection, H_r

$$c_b = -u_p + \sqrt{RC\,\frac{g}{2}\frac{H_r}{H_p}\left(H_r + H_p\right)} \qquad \text{[EQ. 15]}$$

Applying EQ. 15 to our mid-flux circular experiment and considering the time for the initial propagation of the current across the basin, yields an updated estimate for the time necessary for equilibrium to be reached of 182 s into the experiment. This time reasonably matches our observation from overhead imagery of when the bore reaches the proximal rim of the minibasin (200 ± 20 s), but still does not match the time when equilibrium velocity conditions were reached in this experiment (~650±30 sec).

We suggest that the discrepancy between the predictions from the theory of Lamb et al. [2004] and our observations can be explained by laterally evolving concentration and velocity fields, which result in laterally evolving pressure gradients. We recast the problem in light of these observations and hypothesize that time to equilibrium scales with that to replace ambient fluid in minibasins with turbid flow. For a condition in which the height of the ponded cloud is equal to the minibasin depth, this time, T_f, scales as

$$T_f = \frac{V_b}{(Q_{in} F_T)}. \qquad \text{[EQ. 16]}$$

Note that we multiply our influx by the fraction of flow trapped in the minibasin (F_T), which is assumed to be equal to the fraction of sediment trapped in the minibasins (F_s), to account for flux that does not aid replacement of ambient fluid. Applying EQ. 16 to the mid-flux flow condition yields a T_f of 521 sec, similar to the time at which equilibrium velocity conditions are reached.

As minibasin volume, V_b, and Q_{in} are identical in the aspect ratio series, estimates of T_f are all identical. However, we observe quasi equilibrium conditions approximately ~675 s into the L/W = 2 experiment (when H_{umax}/D stabilizes) and 400 s into the L/W = 0.5 experiment (also when H_{umax}/D stabilizes). This suggests a secondary control on time to equilibrium that correlates with the planform aspect ratio, or the ratio of length to width, of a minibasin. Results from the discharge series are more complex. We calculate T_f of 898 s and 290 s for the low and high flux conditions, respectively. Results from the low flux experiment can be interpreted to reach equilibrium at a range of times, depending on the metric used. Timeseries of depth averaged velocity and H_{umax}/D stabilize ~500 s into the experiment, but measurements of Ri_B and p show oscillations that start to develop at ~900 s and continue for the duration of the experiment. Concentration values also show a substantial uptick between the second and third profile collection in the low flux condition, suggesting a flow that is still evolving. Results from the high flux condition reach equilibrium at ~400 sec when the depth average velocity stabilizes. Taken as a whole, we find that our minibasin filling time, T_f, better scales with the time to equilibrium conditions compared with the bore migration time, T_b, proposed by *Lamb et al.* [2004], but further work could better quantify secondary influences.

We apply EQ. 15 to the Brazos-Trinity system of linked minibasins (Fig. 1), focusing on Basins II and IV. We assume Fr_D critical conditions entering each minibasin, use feeder channel/canyon widths and depths, and a range of concentration values (1 – 5 %), to estimate Q_{in} to each minibasin. We then use minibasin volumes, measured for conditions that precede the last episode of significant sediment delivery (24.3-15.3 ka), estimated with minibasin dimensions reported in *Pirmez et al.* [2012] to estimate T_f. This yields values of 1 – 2 days and 5 – 10 days for Basins II and IV, respectively. We note that turbidites in Basin IV do not onlap high onto minibasin slopes, suggesting volume of equilibrated turbid clouds in Basin IV were significantly less than if estimated from the rim elevation of the enclosed minibasin, meaning shorter filling times than our estimates.

Regardless, these estimates of time to equilibrium flow are significantly longer than the ~1 hr suggested by *Lamb et al.* [2004] through application of EQs 12 & 13 to these same minibasins. Measured [*Talling et al.*, 2022; *Xu et al.*, 2004] and estimated flow durations [*Jobe et al.*, 2018] in nature rarely exceed 10 days, and are more commonly on the order of a day. This suggests a significant percent of the active flow time in these minibasins is associated with unsteady/evolving flow, rather than equilibrium conditions. Further, under non-equilibrium flow conditions, a more heterogenous structure of minibasin filling turbidites is anticipated, attributable to variations in shear velocity, sediment suspension, and transport.

3-D Structure of Inlet and Ponded Flow

Overhead imagery of the propagation of the head of turbidity currents entering the experimental minibasins captures the initial lateral structure of turbidity currents (Fig. 2, Movies S1-5). Structure of the inlet flow is later captured with imagery of the dye release (Fig. 7) and with the basin-wide velocity field map (Fig. 11), during equilibrium conditions. We highlight that for all conditions, except the $L = 2W$ experiment, the initial flow traverse (i.e., time taken for head of the turbidity current to flow from proximal to distal minibasin slopes) and structure of the dye front indicate that the inlet flow does not widen to fill the full lateral extent of the minibasins. Rather, maps of the average red intensity measured over the second half of the experiments have sharp gradients between regions of low and high $\overline{r^*}$ that we interpret as boundaries between inlet and ponded flow conditions. The sharp gradients separating these regions suggest sharp shear boundaries with limited mixing across the boundaries (Fig. 7). Higher velocities and turbulent mixing in the inlet flow likely led to greater bed reworking in these regions, relative to portions of the minibasins covered with ponded flow. As such, we suggest that field scale minibasins might have turbidites with structure characterized by tongue-like regions with strong spatial heterogeneity, surrounded laterally and distally by more homogenous bed texture resulting from pure suspension fallout. The greater proximal reworking might also result in the development of channels, which transition to unconfined flows; analogous to what is seen in Brazos-Trinity Basin IV [*Prather et al.*, 2012].

The extent that inlet flow conditions reach into minibasins likely has implications on interpretations of the time to equilibrium. Most of our observations to define when equilibrium is reached come from the minibasin center. We note that the low flux experiment and the $L = 2W$ experiment, wherein interpreting equilibrium time was difficult, featured an inlet region that did not extend to minibasin center. Uncertainty in timing of equilibrium conditions is likely set by the downstream circulation cell. Specifically, for the $L = 2W$ experiment, the low lateral circulation allows penetration of an up-basin flow near the bed, but this vertical circulation is not strong or stable and thus results in pulsing up-basin flow.

Sediment delivered to ponded flow gets laterally distributed throughout minibasins via circulation cells highlighted here (Fig. 11), but also in greater detail in *Reece et al.* [2024]. Velocity magnitude in these cells is significantly less than in the inlet flow, but sufficient to result in deposits that evenly blanket the lateral slopes (Figs. 13&14). While the strength of circulation appears to scale with input discharge, we note that the average horizontal circulation, calculated with EQ. 9, in the $L = 0.5W$ experiment was 59% greater than the $L = 2W$ experiment, even though their input discharges were identical. Combined with our observation of an elevated velocity maximum in the $L = 2W$

experiment, which sat above a weak return flow, suggests that minibasin aspect ratio controls the amount of circulation partitioned along the horizontal vs. vertical flow planes. This has implications for the shear stress applied to the bed by the current, and we document a very gradual increase in velocity with height above the bed in the $L = 2W$, compared to the $L = 0.5W$ experiment. As such, stress on the bed should decrease as basins become long relative to their width, resulting in less bed reworking (i.e., process by which sedimentary particles on the seafloor are moved or redistributed by fluid flow) and more homogenous deposits.

General Implications of Topographic Obstacles

The dynamics of the interactions between turbidity currents and topography reported here have implications beyond enclosed minibasins. A key observation from our work is the dramatic alteration of the vertical flow structure, relative to unconfined flows, that results from flows hitting a topographic obstacle (Figs. 5, 6, 9). In general, this results in elevating the u_{max} flow height (Fig. 10) and decreasing near bed shear stress. The magnitude of this u_{max} height increase, relative to unconfined conditions, is controlled by input discharge and minibasin aspect ratio. The effect due to minibasin aspect ratio appears significant and is perhaps unintuitive. We observed flows in our $L = 2W$ minibasin had u_{max} elevations at the minibasin rim and pulsing return flow near the bed during equilibrium conditions. This aspect ratio represents the 86th percentile of L/W, within the natural spectrum.

Beyond minibasins, we anticipate a similar enhanced elevation of u_{max} could result as flows encounter landslide dams in submarine channels, akin to those recently documented in the Congo submarine channel [*Pope et al.*, 2022b]. While the elevation of

u_{max} should reduce near bed shear stresses in the ponded flow behind the dams, it might result in especially high shear stresses over the dam sill point. Here, u_{max} might reside at or above the dam rim elevation, much like our $L = 2W$ experiment. This could aid erosion of landslide dams, thus reducing the time in which particulate organic carbon and fine particles can be inhibited from downstream transport. For large landslide dams, with sills at the elevation of a canyon or channel rim, an elevated high velocity core could increase the shear stress on canyon or channel walls and enhance the likelihood of avulsion. In contrast, our $L = 0.5W$ had a flow structure that was most like unconfined flows. This suggests that flows hitting obstacles that lack lateral confinement (e.g., shale ridges), might have a less dramatic alteration to their flow structure than ponded flows that strongly feel their lateral side walls. This should allow flows to maintain relatively high shear stresses in regions up dip of these obstacles.

Minibasin Sediment Trapping Potential

Theory emanating from earlier experiments on turbidity current – minibasin interactions suggested that the trapping potential of flows entering minibasins could be estimated with EQ 2 [*Lamb et al.*, 2006; *Toniolo et al.*, 2006b]. The concept here is analogous to a decanting process; where, after a flow inflates to an equilibrium condition, the detrainment flux will equal the flow's top surface area multiplied by the still fluid settling velocity of the suspended sediment size, w_s (here 0.28 mm/s). The experiments reported here were designed with this theory and utilized the still fluid fall velocity of the median grain size. This resulted in predictions of $Q_{in}/Q_{d,max}$ between 0.95 – 0.23 for all experiments, and as such all experiments were predicted to trap 100% of their sediment in the minibasins. In contrast, we observed significant leakage of flow and sediment out of the minibasins (Figs. 13-14). *Lamb et al.* [2006] noted that for natural flows that have a range of grain sizes, the trapping potential of the fine particles in transit will be less than the coarse material. Therefore, we explore how a distribution of grain sizes impacts our estimates of sediment trapping potential and if modeling this distribution can account for the discrepancy between modeled and measured values. We start by comparing how the difference between input current flux (Q_{in}) and detrainment flux (w_sA) varies over the range of particle diameters introduced in our experiments (Fig. 3). When this number is negative, the ability to detrain flow is greater than the flow introduced and as such, a flow comprised of that sediment size should be 100% trapped in the minibasin. In contrast, when this number is positive, the influx exceeds the detrainment capacity and a flow comprised of that grain size would partially leak over the minibasin rim. For the distribution introduced in our experiments, the grain size percentile corresponding to the transition between fully trapped and partially leaking flow shrinks as the input flux decreases (Fig. 15A). This suggests that the high flux experimental minibasin would trap 100% of the coarsest 40% of particle sizes, while the low flux experimental minibasin would be able to trap 100% of the coarsest 95% of particle sizes. We take this one step further and explore how the number of grain size bins modeled impacts predictions of the fraction of input sediment trapped in minibasisns. This is modeled as

$$F_T = 1 - \left(\frac{1}{NQ_{in}}\sum_{i=1}^{N}\begin{cases} Q_{in} - w_{s,i}A & \text{if} \quad (Q_{in} - w_{s,i}A) \geq 0 \\ 0 & \text{if} \quad (Q_{in} - w_{s,i}) < 0 \end{cases}\right), \qquad \text{[EQ. 17]}$$

where *N* represents the number of grain size classes modeled. For example, modeling a flow comprised of two grain size classes involves the summation of the trapping potential of the 25th and 75th percentile grain diameters, while modeling a flow comprised of three grain size classes includes the summation of the trapping potential of the 16th, 50th, and

82nd percentiles, etc. We calculate trapping fractions using up to 10 grain size bins and find that results generally stabilize with use of 5 or more bins (Fig. 15B). However, we find that our measured fraction of sediment trapped in the experimental minibasins is still lower than our modeled values. We emphasize that our measured trapping fractions are likely overestimates due to loss of sediment out of the mapped region, which would only expand this discrepancy.

We suggest that the discrepancy between modeled and measured trapping fractions arises due to the effective sediment fall velocity (i.e., actual fall velocity of particles in a fluid, considering factors such as upward flow velocities) being reduced from the still fluid fall velocity by the detrainment flux. Take for example, a case in which the input discharge is equal to the still fluid fall velocity of the suspended sediment multiplied by the planform area of the minibasin (i.e., a case that should trap 100% of input sediment based on the theory of Lamb et al. [2006]). Assuming all fluid entering the minibasin is lost through vertical detrainment and dividing the input discharge by the basin area results in a vertical detrainment velocity, w_d, equal to -w_s. We can then estimate an effective fall velocity, $w_{s,e}$, as

$$w_{s,e} = w_s + w_d. \qquad \text{[EQ. 18]}$$

In the scenario we provide above, the still fluid sediment fall velocity would exactly balance the detrainment velocity and particles would cease to fall. However, this would shut down the detrainment flux and the particles would start accelerating to their terminal velocity again. Ultimately, we envision a balance between the detrainment flux and the still fluid sediment settling velocity such that $w_s >> w_{s,e} >> 0$. We estimate this balance in our circular experiments in the following manner. To start, we estimate an equilibrium detrainment flux equal to the input flux multiplied by the fraction of flow trapped in a minibasin. For simplicity, we assume the flow trapping fraction is equal to the sediment trapping fraction. As such, fluid that is not lost to sediment charged overspill must be detrained from the flow's top surface. This detrainment flux can be converted to a detrainment velocity by dividing out the minibasin area. Using these estimates for detrainment velocities and the still fluid sediment settling velocity of the D_{50} introduced to the experiments, yields $w_{s,e}$ of 0.22, 0.18, and 0.11 mm/sec in the low, mid, and high flux experiments, respectively. We divide each $w_{s,e}$ by w_s to find the relative reduction in sediment fall velocity due to fluid detrainment, yielding $w_{s,e}/w_s$ values of 0.80, 0.66, and 0.39 for the low, mid, and high flux experiments, respectively. The key finding here is that the detrainment flux influences the ability of particles to fall to the bed and as such reduces the sediment trapping potential of minibasins. Reduction in $w_{s,e}$ from w_s is dependent on the input flux, with higher input fluxes having a greater reduction in fall velocity due to greater detrainment. Reduction in $w_{s,e}$ from w_s is non-trivial as we note that our high input flux experiment was designed to capture all input sediment but likely suffered a reduction in fall velocity of over 50% due to detrainment. Ultimately, we suggest that predicting the trapping potential of minibasins with high precision requires modeling multiple grain size classes present in a flow and accounting for the reduction in effective fall velocity resulting from a detraining fluid. The suggestion implies that minibasins are not as effective at trapping sediment as predicted from prior work [*Lamb et al.*, 2006; *Toniolo et al.*, 2006b].

Previous outcrop observations have documented the expulsion of mud-grade sediment particles from ponded minibasins during the earliest stages of deposition

[*Marini et al.*, 2016]. These field observations provide evidence for fluid detrainment induced expulsion of fine-grained sediment, bridging the gap between the laboratory results presented here and collected stratigraphic data.

These findings have specific implications not only for minibasin trapping of fine particles but also for particulate extraction rates in other settings, including wastewater treatment, as discussed by *Askari Lasaki et al.* [2023]. The efficiency of wastewater treatment plants is limited by this detrainment phenomenon. In such scenarios, the low still-water fluid sediment fall velocities are largely offset by the detrainment flux, suggesting that gravity filtering systems in these plants should address the effect of fluid detrainment to improve their efficiency. Similarly, in minibasins, microplastics and particulate organic carbon, which have low fall velocities, are likely to be preferentially expelled from enclosed minibasins relative to coarser material and can propagate further down regional slopes before ultimate deposition. Further research is necessary to establish a relationship for predicting this reduction in effective fall velocity based solely on input flow parameters.

CONCLUSIONS

Turbidity currents flowing down continental margins often encounter complex topography, including enclosed depressions termed minibasins. While prior studies used physical experiments to examine how turbidity currents interact with two-dimensional minibasins, little is known about these interactions in three-dimensional settings. For the first time, here experimental turbidity current interactions are quantified across a range of three-dimensional minibasins designed with geometries that scale to real-world geological features. This suite of experiments demonstrates the influence of input flow discharge and minibasin shape on the evolving three-dimensional flow field and the capacity of minibasins to induce sedimentation. The key findings include:

1) The time necessary for flows to approach equilibrium conditions is equal to the volume of ponded flow divided by the input flow discharge. Application to the characteristic Brazos-Trinity minibasin system of the GoM indicates that flows might often need several days to equilibrate, indicating that the texture of basin filling turbidites may be dominated by time-evolving flow conditions. This implies that structureless basin-filling turbidites will be rare and linked to infrequent and long-duration events.
2) The shape of minibasins has a strong control on the three-dimensional dynamics of ponded turbidity currents. In all experiments, the development of horizontal circulation cells is observed which distribute fluid and sediment throughout minibasins. Critically, the ability of currents to circulate along a horizontal plane is reduced as minibasins become two-dimensional, e.g., long relative to their width. This reduces flow velocities near the bed and can even result in weak up-basin near bed flow in long but narrow minibasins. An associated reduction in near bed shear stresses further influences the degree of heterogeneity in minibasin filling turbidites.
3) The experiments reported here were designed to trap the experimental flows and all their suspended sediment. This design utilized theory developed from observations of two-dimensional experiments that equated a minibasin trapping potential to the product of basin area and the still fluid fall velocity of the suspended sediment. However, significant stripping of flow and sediment is observed in all but our

lowest influx condition. This is attributed to differences in trapping potential over a distribution of particle sizes introduced to a basin and a reduction in effective sediment fall velocity from the fluid that vertically detrains from minibasins. Reduction in trapping potential will be most severe for small and low-density particles, for example particulate organic carbon and microplastics.

ACKNOWLEDMENTS

This project was supported by student grants to Reece from The Geological Society of America, American Association of Petroleum Geology, and by SEPM, Society for Sedimentary Geology; faculty grants to Straub from The Tulane Carol Lavin Bernick Fund, ExxonMobil, The U.S. - Israel Energy Center funded through the Binational Industry Research and Development Foundation; and Dorrell was funded by the Natural Environment Research Council NE/S014535/1.

AUTHOR CONTRIBUTIONS

J.K.R. and K.M.S. conceived the initial idea of the study. R.M.D. developed the experimental sediment mixture. J.K.R. and K.M.S. lead the development of experimental matrix with input from R.M.D. Experimental protocol designed by K.M.S. with input from J.K.R. Experiments were run by J.K.R. with help from K.M.S. All authors contributed to the data analysis and interpretations. J.K.R. wrote the initial draft of the manuscript with edits and additional contributions provided by K.M.S. and R.M.D.

LIST OF FIGURES

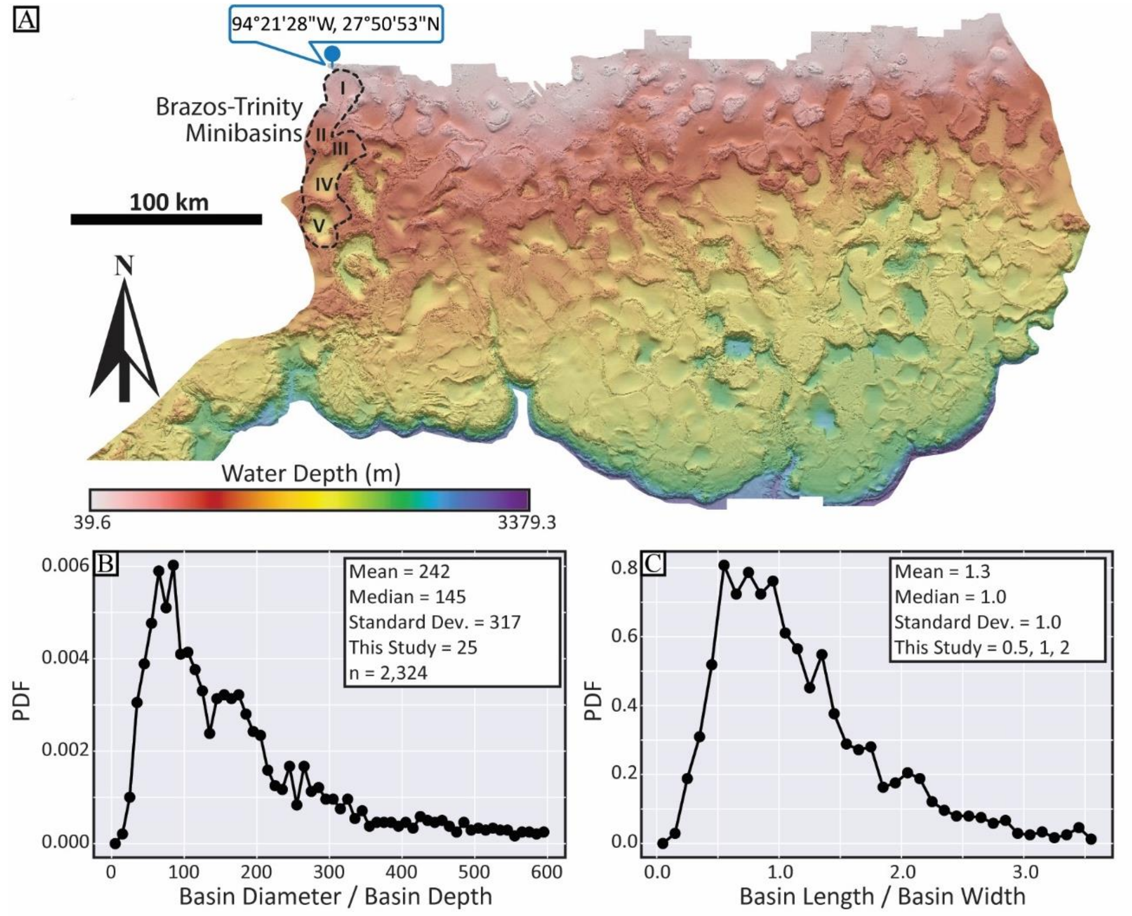

Figure 1. Map of the Fill and Spill region [Steffens et al., 2003] of the northern GoM and distributions that define geometries of enclosed minibasins. (A) Modified version of the high resolution GoM BOEM bathymetry dataset [BOEM, 2017] trimmed to the Fill and Spill region with the margin of the Brazos-Trinity minibasin system shown with dashed line. (B) Distribution of minibasin diameter to depth, where minibasins are defined as local seafloor depressions with a surface area more than 1 km^2. C) Distribution of minibasin length to width, where length is measured from north-south (regional primary flow direction) and width is measured from east to west.

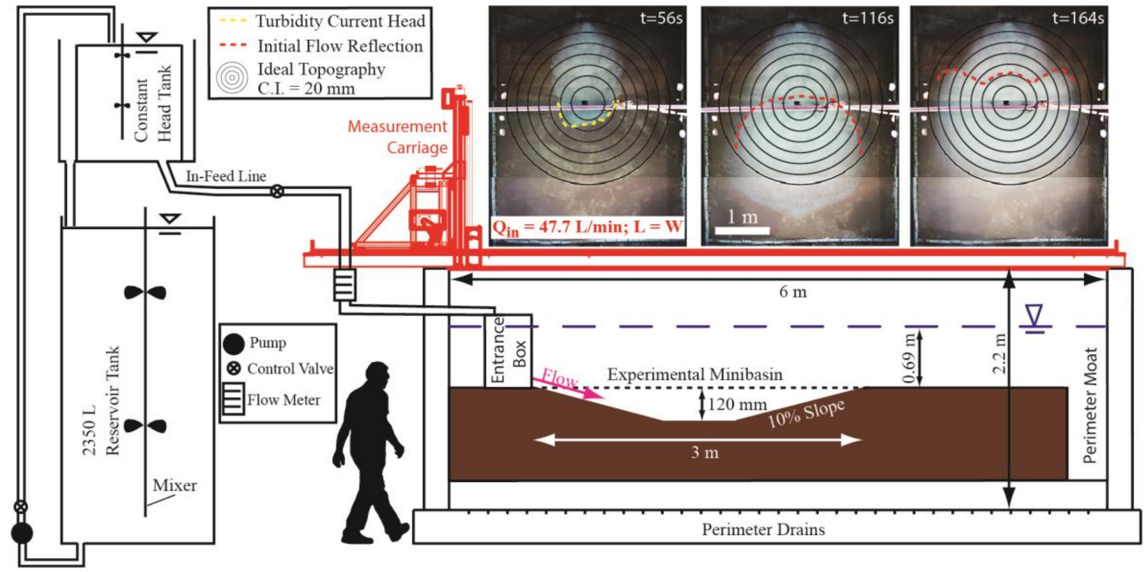

Figure 2. Schematic of experimental setup and images taken from overhead to illustrate early stages of turbidity current development. Flux rate of slurry release to basin was controlled with a series of valves and monitored by a flow meter. False floor in basin with minibasin carved into 300 mm sand is shown in brown, which is surrounded by a drainage moat. Dashed blue line shows elevation of water surface above bed. Schematic not to scale. Images highlight the initial propagation of a turbidity current head (denoted by yellow dashed line) and front of reflected flow (red dashed line). Circular solid black lines are ideal contours of topography.

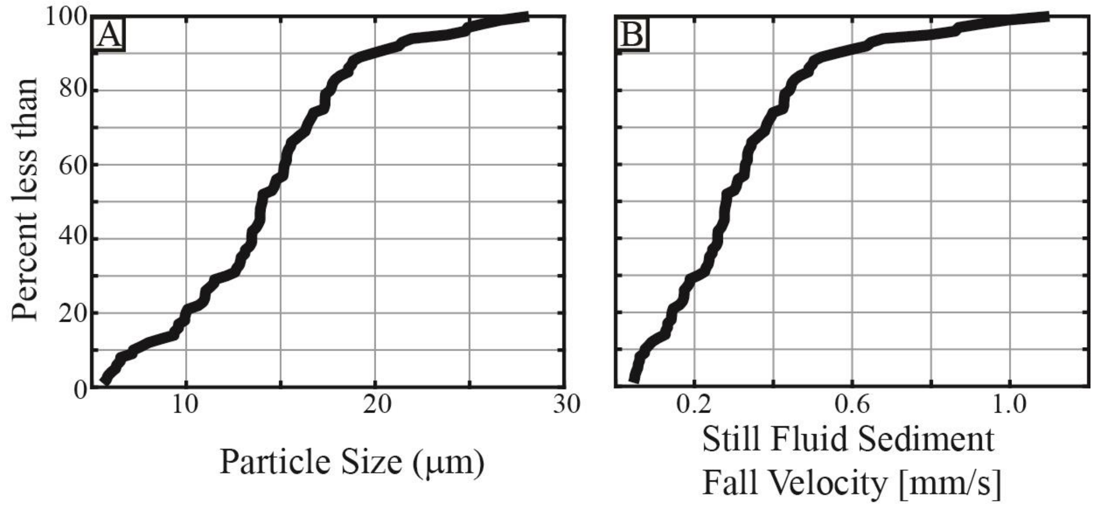

Figure 3. Distributions that describe the size of particles and their corresponding still fluid fall velocity of sediment introduced to experiments. Still fluid fall velocity is calculated with the Ferguson and Church [2004] method.

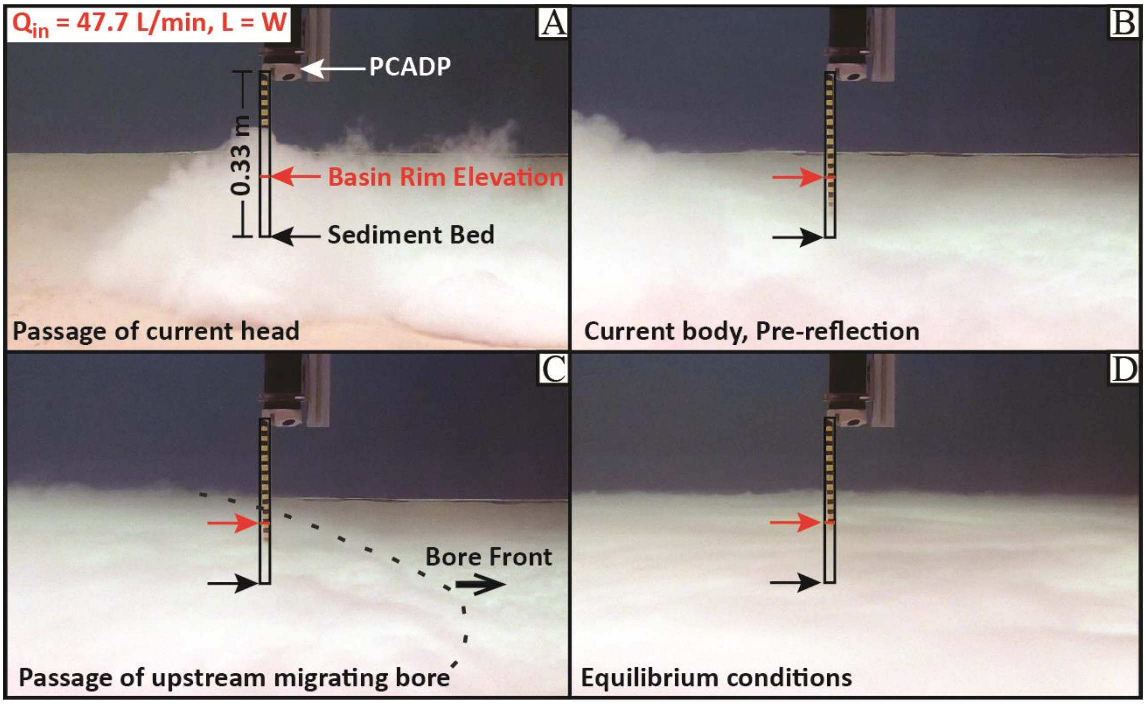

Figure 4. Images used to define the evolution of turbidity currents collected with a GoPro camera installed over the river left basin moat. Data from the mid-flux circular basin condition. 0.33 m rod used to measure height of turbid cloud is outlined in black to aid comparison between images. The thin horizontal red line over the measurement rod denotes elevation of basin rim. Images capture (A) the passage of a thick current head, (B) current body pre-reflection, (C) passage of upstream migrating bore, and (D) equilibrium conditions with placid ponded flow.

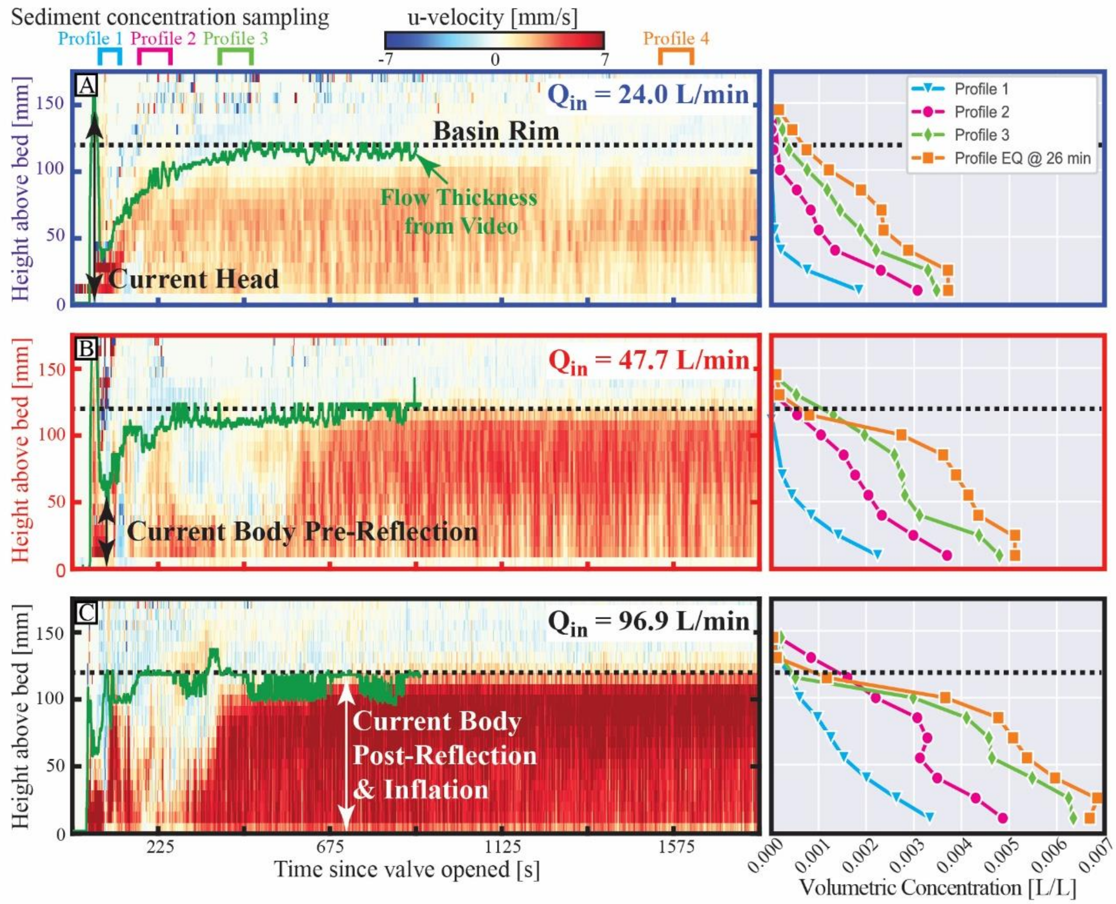

Figure 5. Data used to define the temporally evolving structure of turbidity currents measured at minibasin centers for the discharge series: A) low-flux condition, B) mid-flux condition, and C) high-flux condition. Panels on the left show timeseries of u-component velocity field measured over the minibasin center. Dashed black lines denote elevation of minibasin rim. Green solid lines show timeseries of elevation of the top of the turbid cloud, measured from GoPro footage. We limit this elevation timeseries to the first half of each experiment as dye injection altered parameters used to automate this measurement. Panels on the right show evolving concentration profiles at minibasin centers for four time periods with profile colors that can be linked to time of extractions labeled above the velocity timeseries. We note that flow took between 15-25 seconds to pass through siphon lines, which is corrected for here using the mean time of 20 seconds.

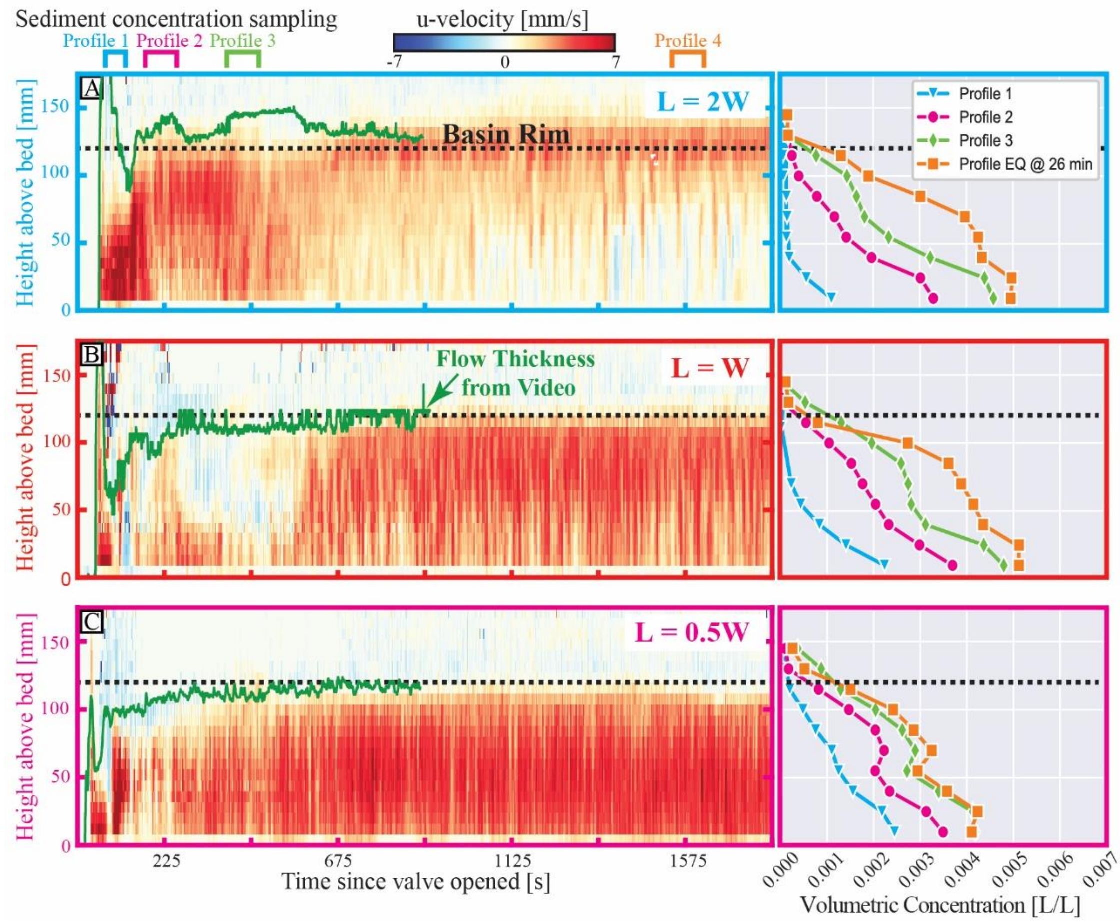

Figure 6. Data used to define the temporally evolving structure of turbidity currents measured at minibasin centers for the planform aspect-ratio series: A) L = 2W condition, B) L = W condition, and C) L = 0.5W condition. Panels on left show timeseries of u-component velocity field measured over minibasin centers. Dashed black lines denote elevation of minibasin rim. Green solid lines show timeseries of elevation of the top of the turbid cloud, measured from the GoPro footage. Panels on the right show evolving concentration profiles at minibasin centers for four time periods with profile colors that can be linked to time of extractions labeled above the velocity timeseries. We note the flow took between 15-25 seconds to pass through siphon lines, which is corrected for here using the mean time of 20 seconds.

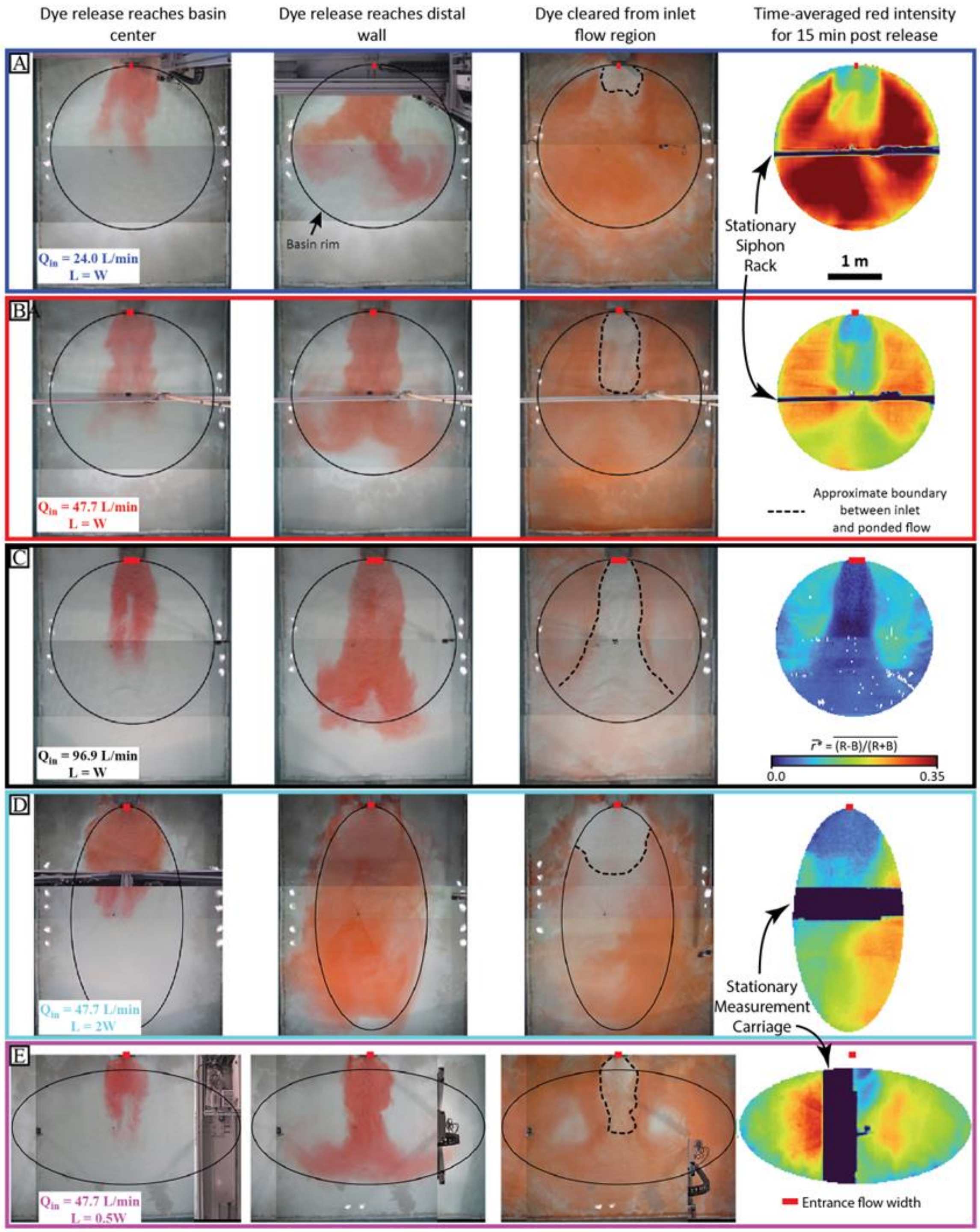

Figure 7. Overhead still frames and results of image analysis of dye release, in which release occurred at the half-way mark of each experiment to highlight equilibrium conditions. Images capture dye front reaching minibasin center (1st column), dye front reaching distal minibasin slope (2nd column), and dye flushed from inlet flow region (3rd column), while the red dye intensity temporally averaged over the second half of an experiment is shown in the 4th column. Solid black lines over still images mark the

location of the minibasin rims, dashed lines reflect approximate boundary that separates inlet from ponded flow. Due to movement of measurement cart, and placement of siphon rack, still images do not always come from the same flow events used to measure the average red dye intensity fields.

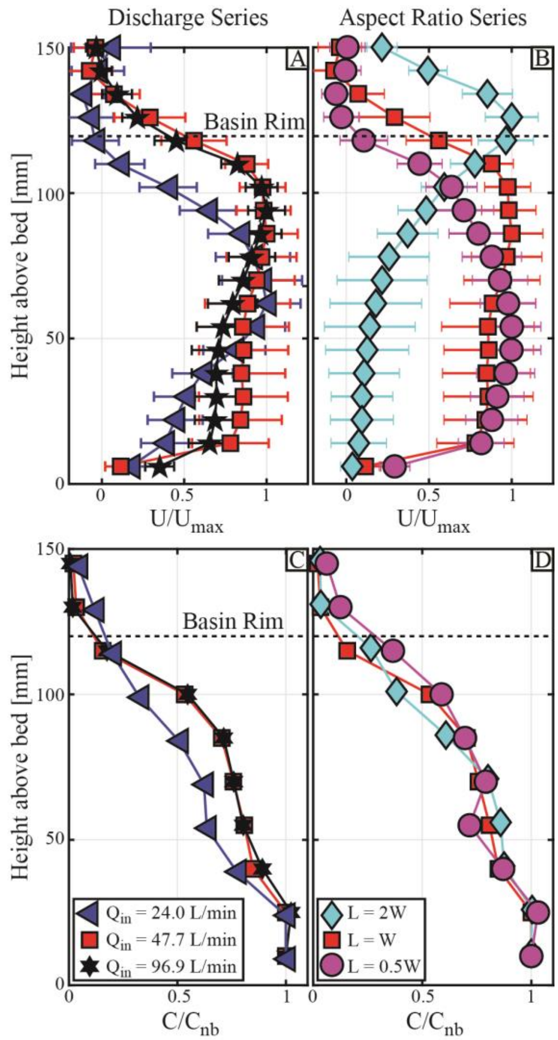

Figure 8. Normalized profiles of velocity (A-B) and concentration (C-D) at equilibrium conditions for the discharge (A&C) and aspect ratio (B&D) series. Velocity profiles are normalized by the maximum velocity measured in each profile, while concentrations are normalized by near bed conditions. Velocity profiles represent temporally averaged conditions for the period over which the fourth concentration profile was extracted (1,560 – 1,652 sec into each experiment). Concentration profiles come from this same period. Horizontal whiskers around velocity measurements denote the 25th and 75th percentile of instantaneous velocity measurements during averaging window. Dashed black lines indicate elevation of the minibasin rim.

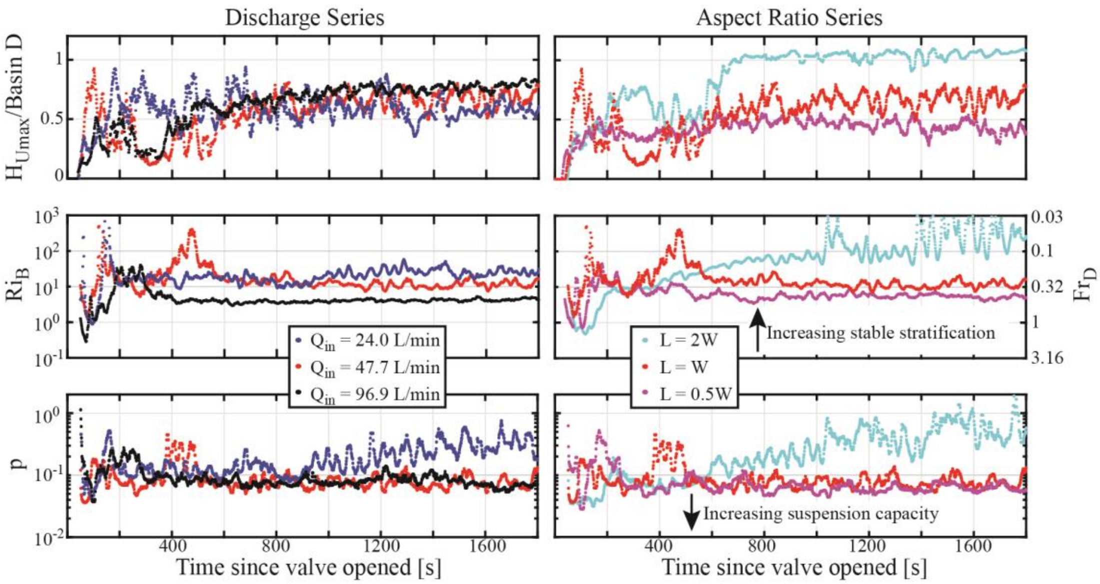

Figure 9. Timeseries of dimensionless numbers that quantify the evolving fluid and sediment transport fields in the discharge (left column) and aspect ratio (right column) series. Top row details height of the velocity maximum relative to basin depth, middle row details the Bulk Richardson number that quantifies stratification of flow relative to shear, and lower row details Rouse number that describes the distribution of sediment suspension.

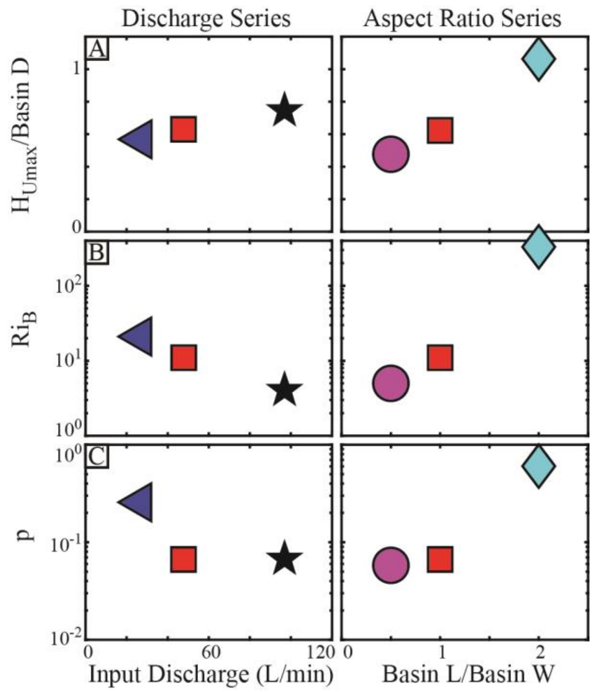

Figure 10. Temporally averaged values of dimensionless numbers that quantify the equilibrium fluid and sediment transport fields in the discharge (left column) and aspect ratio (right column) series. Averaging was done over the time when the fourth concentration profile was extracted (1,560 – 1,652 sec into each experiment).

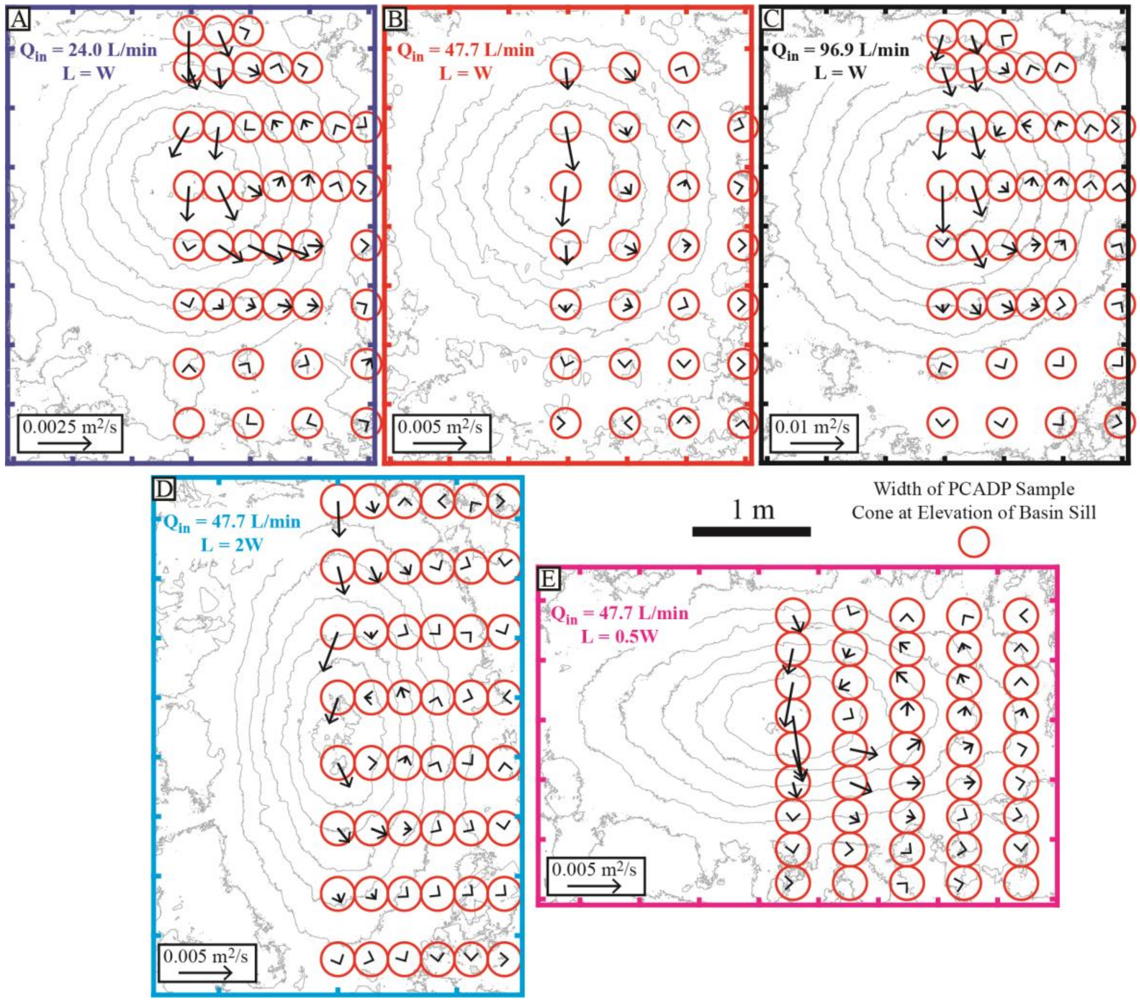

Figure 11. Maps of vector fields that quantify the depth integrated u (down basin) and v (cross basin) velocity components for each experimental condition. Thin gray lines are contours of topography collected prior to turbidity current release. Note differences in scaling of quivers in the discharge series, done to aid comparison of velocity field structures between conditions. Red circles indicate width of PCADP sample cone at minibasin rim elevation in each experiment.

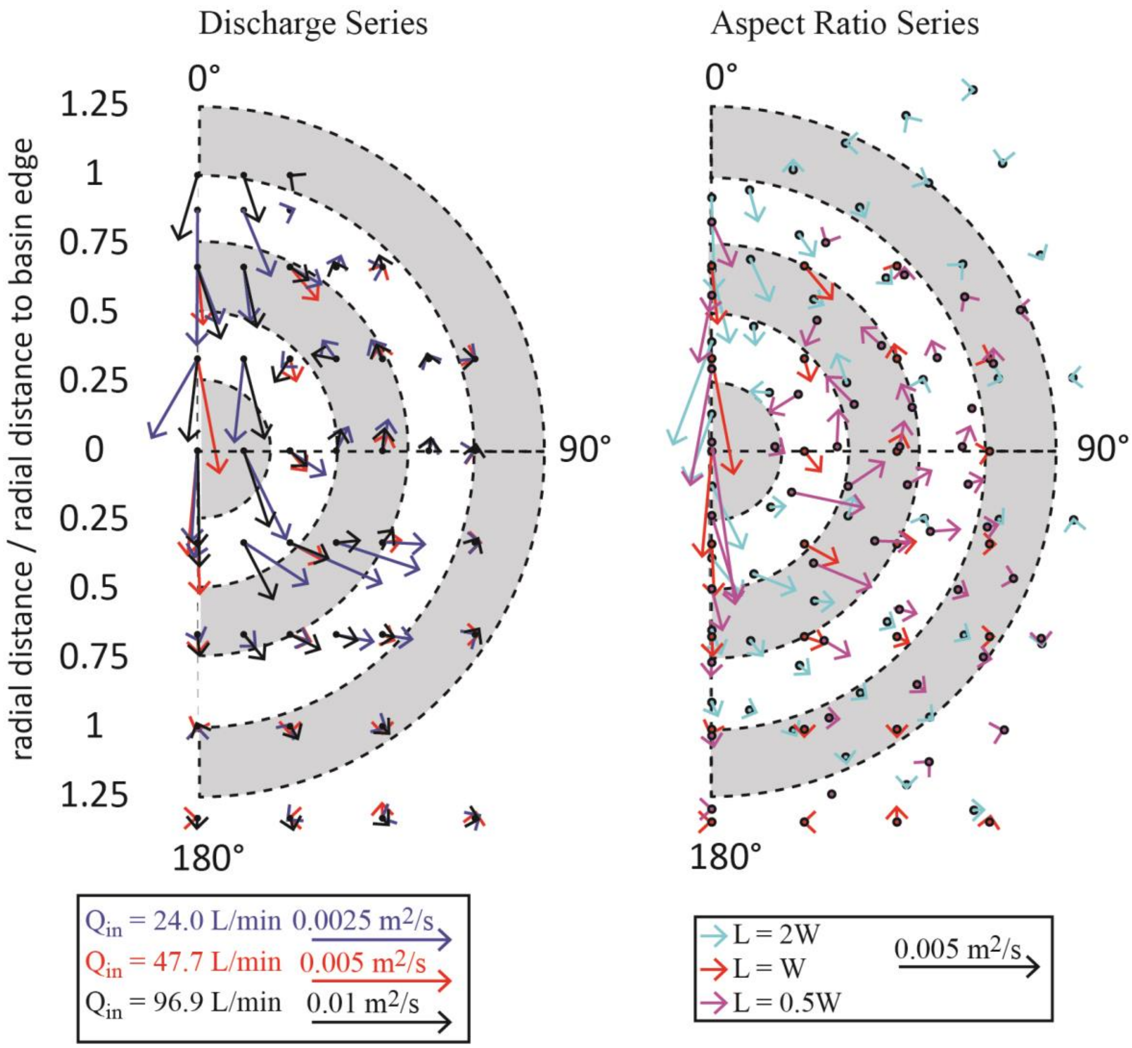

Figure 12. Map of vector field that quantifies the depth integrated u (down basin) and v (cross basin) velocity components for each experimental condition placed into a polar coordinate system. The differences in scaling of quivers across the discharge series, was done to aid comparison of velocity field structures between conditions.

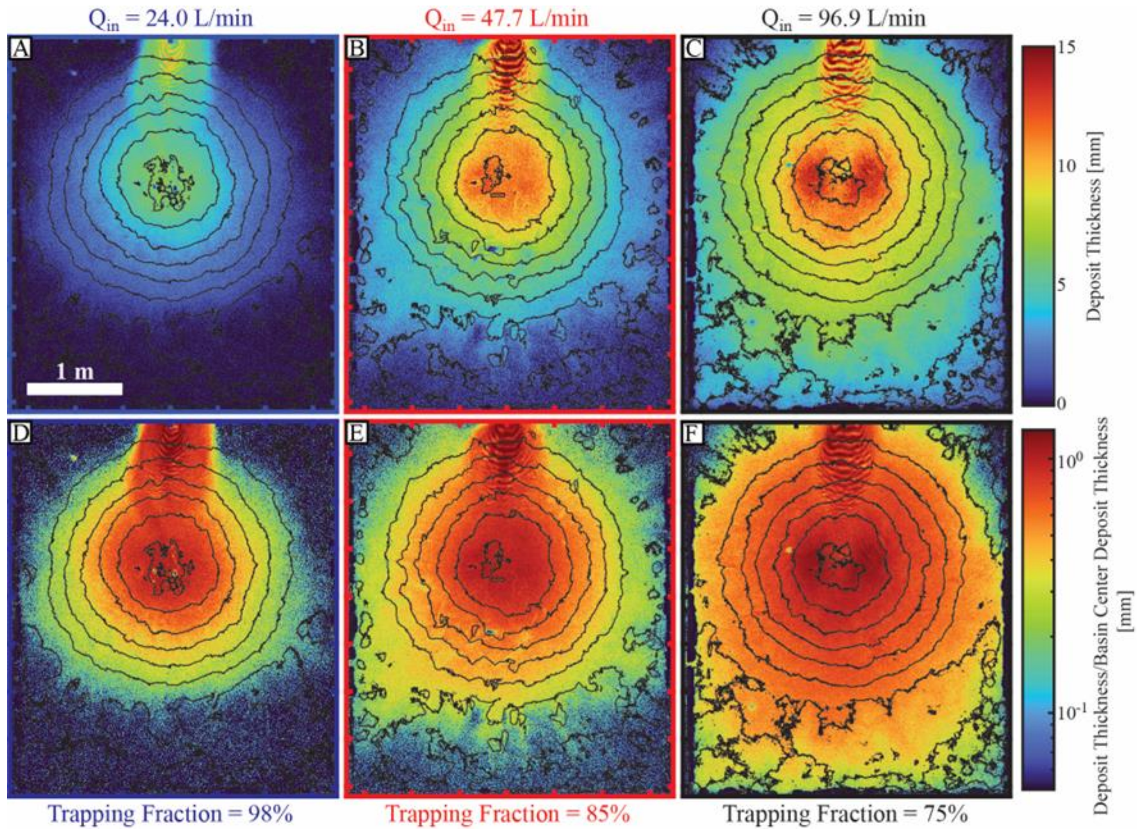

Figure 13. Isopach maps for the discharge series. Top row (A-C) are maps of deposition resulting from two flow events released into each minibasin. Contour lines define the initial topography of each experiment with a contour interval of 20 mm increasing from the minibasin center elevation. Bottom row (D-F) has isopach maps normalized by deposit thickness at minibasin centers. Note that the colormap is logarithmic to highlight structure of turbidites on minibasin slopes.

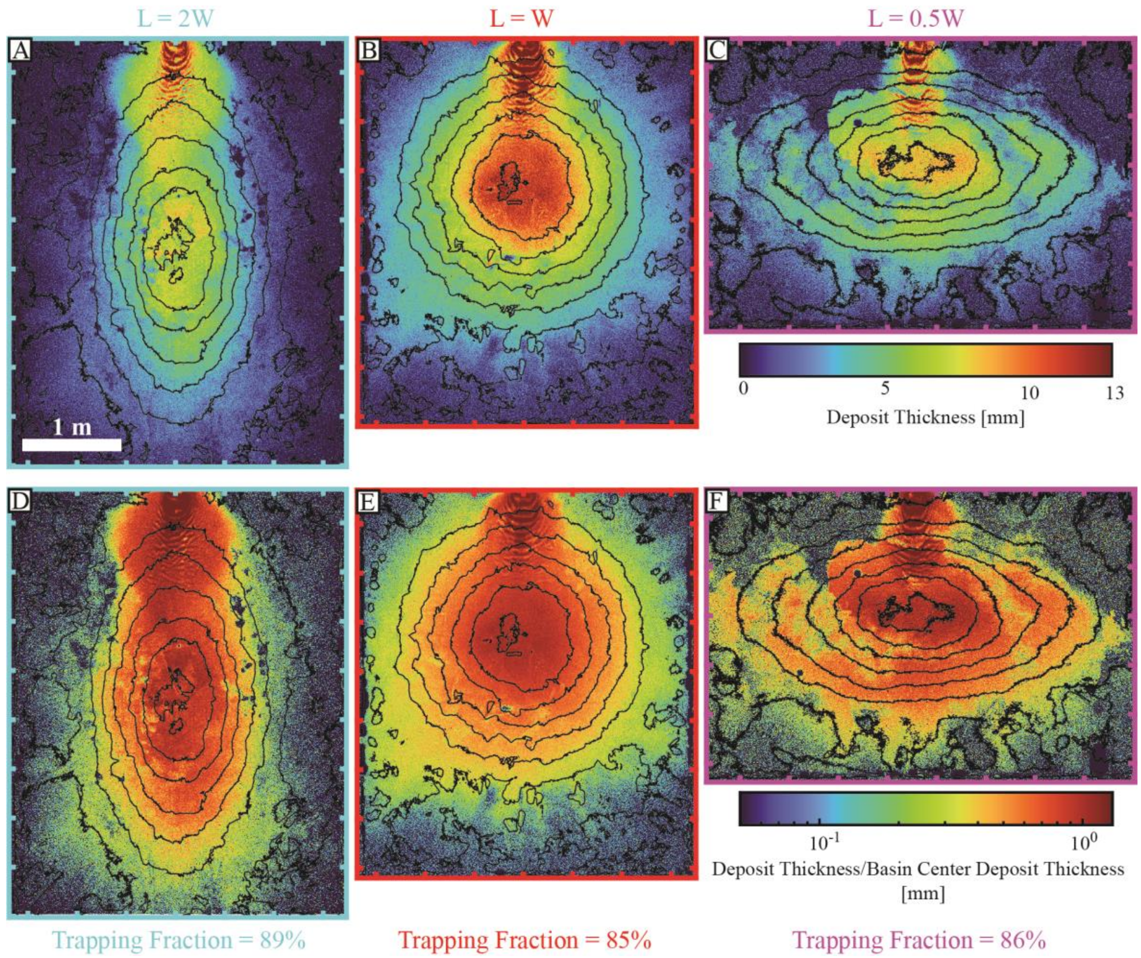

Figure 14. Isopach maps for the aspect ratio series. Top row (A-C) are maps of deposition resulting from two flow events released into each minibasin. Contour lines define the initial topography of each experiment with a contour interval of 20 mm increasing from the minibasin center elevation. Bottom row (D-F) has isopach maps normalized by deposit thickness at minibasin centers. Note that the colormap is logarithmic to highlight structure of turbidites on minibasin slopes.

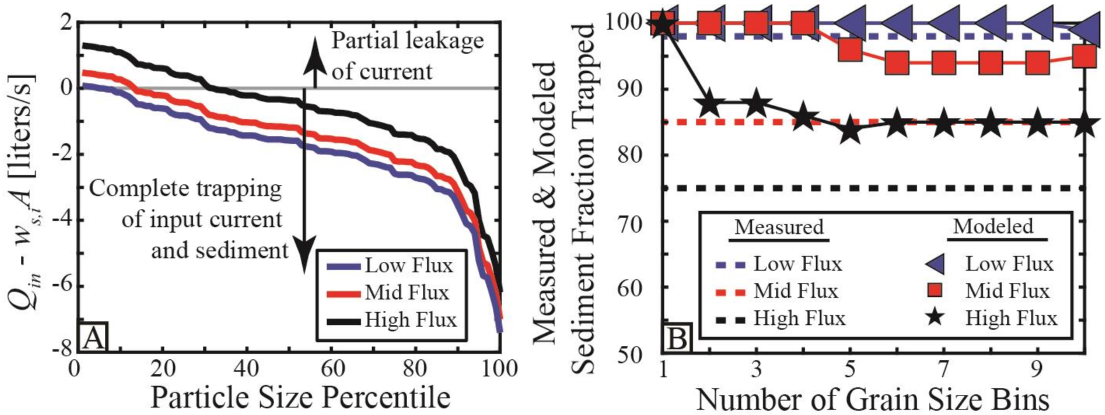

Figure 15. Quantifying the influence of a distribution of particle sizes on the trapping capacity of the experimental minibasins. A) Model for each experiment of the expected difference between an input current flux to a basin and the expected detrainment flux for each percentile of the particle size distribution. When this difference is positive, some current and sediment is expected to leak out of the experimental minibasin. B) Measurements (dashed lines) and models (symbols) of the fraction of sediment introduced to an experiment that gets trapped in the minibasin. Models explore the implication of utilizing information about the grain size distribution when estimating a trapping fraction through the use of equation 17.

LIST OF REFERENCES

Alexander, L., and P. Flemings (1995). Geologic evolution of a Pliocene–Pleistocene salt-withdrawal minibasin: Eugene Island Block 330, offshore Louisiana. *AAPG bulletin*, **79**(12), 1737-1756.

Altinakar, M., W. Graf, and E. Hopfinger (1996). Flow structure in turbidity currents, *Journal of Hydraulic Research*, **34**(5), 713-718.

Andresen, K., M. Huuse, N. Schødt, L. Clausen, and L. Seidler (2011). Hydrocarbon plumbing systems of salt minibasins offshore Angola revealed by three-dimensional seismic analysis. *AAPG bulletin*, **95**(6), 1039-1065.

Askari Lasaki, B., P. Maurer, and H. Schönberger (2023). A fundamental study on the extraction of particulate organic carbon from municipal wastewater treatment plants. *Water*, **15**(10), 1861.

Badalini, G., B. Kneller, and C. Winker (2000). Architecture and Processes in the Late Pleistocene Brazos-Trinity Turbidite System, Gulf of Mexico Continental Slope, *GCSSEPM 20th Annual Research Conference Deep-Water Reservoirs of the World*, 16-34.

Bastianon, E. (2018). Numerical Modeling of Submarine Minibasin Flow and Morphodynamics, Ph.D. thesis, 152 pp., University of South Carolina, Columbia, South Carolina, USA.

Bastianon, E., E. Viparelli, A. Cantelli, and J. Imran (2021). 2D numerical simulation of the filling process of submarine minibasins: Study of deposit architecture, *Journal of Sedimentary Research*, ***91***(4), 399-414.

Beaubouef, R., and V. Abreu (2006). Basin 4 of the Brazos-Trinity slope system: Anatomy of the terminal portion of an intra-slope lowstand systems tract, *Gulf Coast Association of Geological Societies Transactions*, **56**(1), 39-49.

Beaubouef, R. (2004). Deep-water leveed-channel complexes of the Cerro Toro Formation, Upper Cretaceous, southern Chile. *AAPG bulletin*, **88**(11), 1471-1500.

BOEM. Northern GoM Deepwater Bathymetry Grid from 3D Seismic [Data file]. Retrieved from https://www.boem.gov/oil-gas-energy/mapping-and-data/map-gallery/northern-gom-deepwater-bathymetry-grid-3d-seismic. (2017).

Bonnecaze, R., H. Huppert, and J. Lister (1993). Particle-driven gravity currents, *Journal of Fluid Mechanics*, **250**(1), 339-369.

Catuneanu, O. (2019). Scale in sequence stratigraphy, *Marine and Petroleum Geology*, **106**(1), 128-159.

Dinc, G., J. Callot, and J. Ringenbach (2022). Shale mobility: From salt-like shale flow to fluid mobilization in gravity-driven deformation, the late Albian–Turonian White Pointer Delta (Ceduna Subbasin, Great Bight, Australia). *Geology*, **51**(2), 174-178.

Dorrell, R., M. Patacci, and W. McCaffrey (2018). Inflation of Ponded, Particulate Laden Density Currents, *Journal of Sedimentary Research*, **88**(11), 1276-1282.

Ellison, T., and J. Turner (1959). Turbulent entrainment in stratified flows, *Journal of Fluid Mechanics*, **6**(3), 423-448.

Esposito, C., D. Di Leonardo, M. Harlen, and K. Straub (2018). Sediment storage partitioning in alluvial stratigraphy: The influence of discharge variability, *Journal of Sedimentary Research*, **88**(1), 717-726.

Ferguson, R., and M. Church (2004). A simple universal equation for grain settling velocity, *Journal of Sedimentary Research*, **74**(6), 933-937.

Fukuda, S., M. de Vet, E. Skevington, E. Bastianon, R. Fernández, and X. Wu (2023). Inadequacy of fluvial energetics for describing gravity current autosuspension, *Nature Communications*, **14**(1), 2288.

Ge, Z., R. Gawthorpe, A. Rotevatn, L. Zijerveld, C. Jackson, and A. Oluboyo (2020). Minibasin depocentre migration during diachronous salt welding, offshore Angola, *Basin Research*, **32**(5), 875-893.

Hudec, M., and M. Jackson (2007). Terra infirma: Understanding salt tectonics, *Earth-Science Reviews*, **82**(1-2), 1-28.

Hudec, M., M. Jackson, and F. Peel (2013). Influence of deep Louann structure on the evolution of the northern Gulf of Mexico, *AAPG bulletin*, **97**(10), 1711-1735.

Jobe, Z., N. Howes, B. Romans, and J. Covault (2018). Volume and recurrence of submarine-fan-building turbidity currents, *The Depositional Record*, **4**(2), 160-176.

Lamb, M., T. Hickson, J. Marr, B. Sheets, C. Paola, and G. Parker (2004). Surging versus continuous turbidity currents: flow dynamics and deposits in an experimental intraslope minibasin, *Journal of Sedimentary Research*, **74**(1), 148-155.

Lamb, M., H. Toniolo, and G. Parker (2006). Trapping of sustained turbidity currents by intraslope minibasins, *Sedimentology*, **53**(1), 147-160.

Maharaj, V. (2012). The effects of confining minibasin topography on turbidity current dynamics and deposit architecture, Ph.D. thesis, 608 pp., University of Texas, Austin, Texas, USA.

Marini, M., M. Patacci, F. Felletti, and W. McCaffrey (2016). Fill to spill stratigraphic evolution of a confined turbidite mini-basin succession, and its likely well bore expression: The Castagnola Fm, NW Italy, *Marine and Petroleum Geology*, **69**(1), 94-111.

Massimi, P., A. Quarteroni, F. Saleri, and G. Scrofani (2007). Modeling of salt tectonics. *Computer methods in applied mechanics and engineering*, **197**(1-4), 281-293.

Mitchell, W., A. Whittaker, M. Mayall, and L. Lonergan (2021). New models for submarine channel deposits on structurally complex slopes: Examples from the Niger Delta system, *Marine and Petroleum Geology*, **129**(1), 105040.

Mohriak, W., P. Szatmari, and S. Anjos (2012). Salt: geology and tectonics of selected Brazilian basins in their global context, *Geological Society, London, Special Publications*, **363**(1), 131-158.

Mousouliotis, A., S. Pechlivanidou, K. Albanakis, A. Georgakopoulos, and B. Medvedev (2021). Deciphering salt tectonic deformation patterns in the Eastern Mediterranean: Insights from the Messinian evaporite in the Herodotus Basin, *Marine and Petroleum Geology*, **133**(1), 105317.

Parker, G., M. Garcia, Y. Fukushima, and W. Yu (1987). Experiments on turbidity currents over an erodible bed, *Journal of Hydraulic Research*, **25**(1), 123-147.

Patacci, M., P. Haughton, and W. Mccaffrey (2015). Flow behavior of ponded turbidity currents, *Journal of Sedimentary Research,* **85**(8), 885-902.

Pirmez, C., R. Beaubouef, S. Friedmann, and D. Mohrig (2000). Equilibrium profile and baselevel in submarine channels: examples from Late Pleistocene systems and implications for the architecture of deepwater reservoirs. Paper presented at the *GCSEPM Foundation 20th Annual Research Conference, Deep-Water Reservoirs of the World*, Houston, TX.

Planchon, O., and F. Darboux (2002). A fast, simple and versatile algorithm to fill the depressions of digital elevation models, *Catena*, **46**(2-3), 159-176.

Pope, E., M. Cartigny, M. Clare, P. Talling, D. Lintern, A. Vellinga, et al. (2022a). First source-to-sink monitoring shows dense head controls sediment flux and runout in turbidity currents, *Science Advances*, **8**(20), eabj3220.

Pope, E., M. Heijnen, P. Talling, R. Jacinto, A. Gaillot, M. Baker, et al. (2022b). Carbon and sediment fluxes inhibited in the submarine Congo Canyon by landslide-damming, *Nature Geoscience*, **15**(10), 845-853.

Prather, B. (2003). Controls on reservoir distribution, architecture and stratigraphic trapping in slope settings, *Marine and Petroleum Geology*, **20**(6-8), 529-545.

Prather, B., C. Pirmez, C. Winker, M. Deptuck, D. Mohrig, B. Van Hoorn, and R. Wynn (2012). Stratigraphy of linked intraslope basins: Brazos-Trinity system western

Gulf of Mexico, *Application of the principles of seismic geomorphology to continental-slope and base-of-slope systems: Case studies from seafloor and near-seafloor analogues: SEPM, Special Publication*, edited by Bradford E. Prather, Mark E. Deptuck, David Mohrig, Berend Van Hoorn, Russell B. Wynn, **99**(1), 83-109.

Reece, J., R. Dorrell, and K. Straub (2024). Circulation of hydraulically ponded turbidity currents and the filling of continental slope minibasins, *Nature Communications*, **15**(1), 2075.

Rouse, H. (1939). Experiments on the mechanics of sediment transport. Paper presented at the *5th International Congress of Applied Mechanics*, Hoboken, NJ.

Sequeiros, O., B. Spinewine, R. Beaubouef, T. Sun, M. García, and G. Parker (2010). Characteristics of velocity and excess density profiles of saline underflows and turbidity currents flowing over a mobile bed, *Journal of Hydraulic Engineering*, **136**(7), 412-433.

Sequeiros, O., B. Spinewine, M. Garcia, R. Beaubouef, T. Sun, and G. Parker (2009). Experiments on wedge-shaped deep sea sedimentary deposits in minibasins and/or on channel levees emplaced by turbidity currents. Part I. Documentation of the flow, *Journal of Sedimentary Research*, **79**(8), 593-607.

Shcherbina, A., E. D'Asaro, and S. Nylund (2018). Observing finescale oceanic velocity structure with an autonomous Nortek acoustic Deoppler current profiler, *Journal of Atmospheric and Oceanic Technology*, **35**(2), 411-427.

Smith, R. (2004). Turbidite systems influenced by structurally induced topography in the multi-sourced Welsh Basin, *Geological Society, London, Special Publications*, **222**(1), 209-228.

Soto, J., M. Heidari, and M. Hudec (2021). Proposal for a mechanical model of mobile shales, Scientific Reports, 11(1), 23785.

Steffens, G., E. Biegert, H. Sumner, and D. Bird (2003). Quantitative bathymetric analyses of selected deepwater siliciclastic margins: receiving basin configurations for deepwater fan systems, *Marine and Petroleum Geology*, **20**(6-8), 547-561.

Straub, K., and D. Mohrig (2009). Constructional Canyons Built by Sheet-Like Turbidity Currents: Observations from Offshore Brunei Darussalam, *Journal of Sedimentary Research*, **79**(1-2), 24-39.

Stricker, S., S. Jones, N. Meadows, and L. Bowen (2018). Reservoir quality of fluvial sandstone reservoirs in salt-walled mini-basins: an example from the Seagull field, Central Graben, North Sea, UK, *Petroleum Science*, **15**(1), 1-27.

Sylvester, Z., A. Cantelli, and C. Pirmez (2015). Stratigraphic evolution of intraslope minibasins: Insights from surface-based model, *AAPG bulletin*, **99**(6), 1099-1129.

Talling, P., J. Allin, D. Armitage, R. Arnott, M. Cartigny, M. Clare, F. Felletti, J. Covault, S. Girardclos, and E. Hansen (2015). Key future directions for research on turbidity currents and their deposits, *Journal of Sedimentary Research*, **85**(2), 153-169.

Talling, P., M. Baker, E. Pope, S. Ruffell, R. Jacinto, M. Heijnen, S. Hage, S. Simmons, M. Hasenhündl, and C. Heerema (2022). Longest sediment flows yet measured show how major rivers connect efficiently to deep sea, *Nature Communications*, **13**(1), 4193.

Toniolo, H., G. Parker, V. Voller, and R. Beaubouef (2006a). Depositional turbidity currents in diapiric minibasins on the continental slope: experiments—numerical simulation and upscaling, *Journal of Sedimentary Research*, **76**(5), 798-818.

Toniolo, H., M. Lamb, and G. Parker (2006b). Depositional turbidity currents in diapiric minibasins on the continental slope: formulation and theory, *Journal of Sedimentary Research*, **76**(5), 783-797.

Tucker, C. (1979). Red and photographic infrared linear combinations for monitoring vegetation, *Remote sensing of Environment*, **8**(2), 127-150.

van Rensbergen, P., C. Morley, D. Ang, T. Hoan, and N. Lam (1999). Strucutural evolution of shale diapers from reactive rise to mud volcanism: 3D seismic data from the Baram delta, offshore Brunei, Darussalam, *Journal of the Geological Society of London*, **156**(1), 633-650.

Vendettuoli, D., M. Clare, J. Clarke, A. Vellinga, J. Hizzet, S. Hage, et al. (2019). Daily bathymetric surveys document how stratigraphy is built and its extreme incompleteness in submarine channels, *Earth and Planetary Science Letters*, **515**(1), 231-247.

Violet, J., B. Sheets, L. Pratson, C. Paola, R. Beaubouef, and G. Parker (2005). Experiment on turbidity currents and their deposits in a model 3D subsiding minibasin, *Journal of Sedimentary Research*, **75**(5), 820-843.

Wahab, A., D. Hoyal, M. Shringarpure, and K. Straub (2022). A dimensionless framework for predicting submarine fan morphology, *Nature Communications*, **13**(1), 7563.

Wang, L., and H. Liu (2006). An efficient method for identifying and filling surface depressions in digital elevation models for hydrologic analysis and modelling, *International Journal of Geographical Information Science*, **20**(2), 193-213.

Winker, C. (1996). High-resolution seismic stratigraphy of a late Pleistocene submarine fan ponded by salt-withdrawal mini-basins on the Gulf of Mexico continental slope. Paper presented at the *Offshore Technology Conference*, Houston, TX.

Winker, C., and J. Booth (2000). Sedimentary dynamics of the salt-dominated continental slope, Gulf of Mexico: Integration of observations from the seafloor, near-surface, and deep subsurface. Paper presented at the *GCSEPM Foundation 20th Annual Research Conference: Deep-water Reservoirs of the World*, Houston, TX.

Winkler, W., and P. Gawenda (1999). Distinguishing climatic and tectonic forcing of turbidite sedimentation, and the bearing on turbidite bed scaling: Palaeocene-Eocene of northern Spain, *Journal of the Geological Society*, **156**(4), 791-800.

Xu, J., M. Nobel, and L. Rosenfeld (2004). In-situ measurments of velocity structure within turbidity currents, *Geophysical Research Letters*, **31**(9), 1-4.

Zucker, E., Z. Gvirtzman, J. Steinberg, and Y. Enzel (2020). Salt tectonics in the Eastern Mediterranean Sea: Where a giant delta meets a salt giant, *Geology*, **48**(2), 134-138.

CHAPTER 4

Quantifying the statistical organization of ponded accommodation resulting from salt dynamics along the northern Gulf of Mexico continental margin

ABSTRACT

The morphology of continental margins reflects a dynamic interplay between the depositional mechanics of sediment transporting flows and the influence of existing topographic features. In particular, the northern Gulf of Mexico passive margin exemplifies a region whose current bathymetry is strongly influenced by active diapirism, or the upward movement of an underlying buoyant unit of salt, of the Louann Salt layer along the Mesozoic passive continental margin. Breached and intact salt domes create topographic highs, and salt removal to the domes creates topographic lows, with sediment supply exerting a strong control. These processes are responsible for most of the margin's accommodation below a graded profile. We quantify the statistics of ponded accommodation, which can exceed 100 m on the northern Gulf of Mexico margin and occupies three-dimensionally closed topographic lows. This analysis describes the topographic features that influence sediment deposition or erosion by turbidity currents, which is a crucial aspect of continental margin evolution. This is accomplished with a vast bathymetric dataset made public by the U.S. Bureau of Ocean and Energy Management. The depressions, which are often termed minibasins, can trap sediment transporting flows as they move down continental margins, resulting in thick deposits that act as geofluid reservoirs. We extract and measure the scales of depressions, which follow Pareto distributions. The distribution tails becoming heavier as we increase the dimensionality of the quantification (e.g., compare distributions of depression relief, area,

and volume). Comparing different subregions of the margin indicates that the weight of the distribution tail also increases with the thickness of the underlying salt, suggesting enhanced self-organization of bathymetry. While close to 10,000 depressions are identified, the manner of self-organization results in most of the ponded accommodation residing in a relatively few large depressions on the margin. Finally, the nested hierarchy of depressions, defined as depressions within depressions, is found to be greatest over regions with the thickest salt and the largest depressions.

INTRODUCTION

In both terrestrial and deep marine environments, a morphodynamic trinity exists, comprising topography, fluid flow (e.g., patterns of motion of the fluid), and sediment transport fields (i.e., the result of the interaction between topography and fluid flow). These interrelated components collectively control the evolution of sediment routing systems. In discussions of this trinity, topographic adjustments generally focus on sediment exchange with an alluvial bed, a deposit of sediment formed by a river or stream, that resides on a relatively fixed substrate [*Church*, 2006; *Jerolmack and Mohrig*, 2005; *McElroy and Mohrig*, 2009; *Naden*, 1987; *Simpson and Schlunegger*, 2003; *Smith and McLean*, 1977]. Each of the three components of this morphodynamic trinity directly influence the other two components; for example, a reduction in transport slope with downstream distance induces a reduction in flow velocity and thus sediment transport capacity, resulting in deposition and alteration of the slope. The gradient of many continental slopes is a direct product of this morphodynamic trinity, where the dominant sediment transporting flows are turbidity currents [*Pratson et al.*, 2007; *Pratson and Haxby*, 1996]. While some continental margins exhibit relatively simple concave up profiles, others display significant bathymetric complexity [*Mosher et al.*, 2017; *Pratson and Haxby*, 1996; *Thorne and Swift*, 1991]. This complexity often takes on a vertical dimension, characterized by nested depressions (depressions within depressions), a consequence of active tectonics or the presence of salt or shale substrates [*Prather et al.*, 1998]. The concept of a morphodynamic trinity takes on new meaning in settings underlain by salt or uncompacted shale as sediment loading, controlled by sediment supply, can cause ductile substrate deformation over geological timescales, which continues to influence the fluid and sediment transport fields. This deformation contributes to deviations from the geological concept known as *grade*, which in terms of sedimentary dynamics represents the equilibrium profile of a margin shaped by sediment-transporting flows in the absence of time-varying subsidence or uplift [*Prather*, 2003; *Gilbert*, 1877; *Mackin*, 1948]. This equilibrium state results from a balance of sedimentation processes with the production of *accommodation* to store sediment [*Pyles et al.*, 2011]. Here, *accommodation* is the space available to store sediment and is formally defined in a volumetric framework [*Jervey*, 1988; *Muto and Steel*, 2000]. Ultimately, quantifying accommodation is analogous to detailing the potential for change in an evolving continental margin. While the concepts of *grade* and *accommodation* have been around for decades, few studies characterize the statistics that describe how accommodation resulting from mobile substrates is organized on continental margins.

Following prior research [*Prather*, 2003], we recognize ponded accommodation as the space lying within three-dimensionally closed topographic lows on continental slopes whose cap is defined at the lowest spill point height. Ponded accommodation is highly effective in extracting sediment from turbidity currents as they have to traverse flat and/or adverse slopes, which decelerate flows and reduce sediment transport capacity [*Kneller et al.*, 2016; *Wells and Dorrell*, 2021]. Depressions resulting from topography created by diapirism that are large enough to influence the depositional mechanics of turbidity currents are often termed minibasins. Numerical and physical experimental studies suggest minibasins can cause collapse of turbidity currents as they traverse the flat centers, or in some cases induce hydraulic ponding and flow inflation [*Dorrell et al.*, 2018; *Patacci et al.*, 2015; *Lamb et al.*, 2004; *Toniolo et al.*, 2006]. Hydraulic ponding, a process where flows are trapped within depressions, initiates when turbidity currents reflect off distal basin walls, generating low densimetric Froude number flows with limited ambient fluid entrainment and usually requires depression relief, or the difference in elevation between the lowest point of a depression and its spill point, to be comparable to the thickness of a current [*Lamb et al.*, 2004; *Patacci et al.*, 2015; *van Andel and Komar*, 1969]. While ponded accommodation is rather efficient at inducing deposition, it is limited along many continental margins (e.g., 1, 2, and 5% of total accommodation found offshore NW Borneo, Nigeria, and Angola, respectively) [*Steffens et al.*, 2003]. However, offshore the central portion of the northern Gulf of Mexico (GoM) margin, which is underlain by a mobile salt substrate, ponded accommodation accounts for 55% of the total accommodation [*Steffens et al.*, 2003].

Here, the statistics of minibasins along the northern Gulf of Mexico are quantified to understand the scales of depressions that are important for this type of accommodation (i.e., does ponded accommodation predominantly exists in a few large minibasins or in smaller depressions, of which there are many). Additionally, the patterns of depressions of varying geometric scales offer insights into how the underwater terrain organizes itself (i.e., self-organization of bathymetry), and how this self-organization changes from water depths and four different subregions of the margin that are underlain by different thicknesses of salt. Imaging of strata, or deposited sedimentary layers, in minibasins suggest patterns of minibasin subsidence can be influenced by neighboring minibasins [*Hudec et al.*, 2009] if they develop in relatively close proximity to one another. This is supported by dynamics captured in numerical and physical experiments, in which strata can be rotated due to spatial variations in the salt flow field, inducing temporal and spatial gradients in minibasin floor subsidence [*Callot et al.*, 2016; *Fernandez et al.*, 2020; *Sylvester et al.*, 2015]. Given the spatial configuration of sediment loading, these interactions can even lead to depression merger or the joining together of depressions through time, resulting in aerially extensive minibasins. Together, these observations and experiments highlight interactions between minibasins and the self-organization of bathymetry above thick salt substrates. Finally, we document the complexity of depressions in four different subregions of the margin that are underlain by different thicknesses of salt by quantifying the number of nested levels, or the different hierarchical levels within a nested structure, they contain. Addressing these questions aids quantification of the roughness scales that turbidity currents must interact with as they move down the GoM margin. As highlighted by previous studies, these roughness elements slow the downslope progression of turbidity currents resulting in sediment deposition that fills accommodation, bringing the margin closer to *grade* [*Alexander and Morris*, 1994; *Gilbert*, 1877; *Mackin*, 1948; *Nasr-Azadani and Meiburg*, 2014; *Soutter et al.*, 2021]. Deposition then further drives the unique morphodynamic trinity of salt provinces as the resulting deposition has the potential to induce further salt withdrawal and minibasin subsidence.

Topographic Impacts of Mobile Salt Substrates

Gravity-driven salt diapirism plays a crucial role in shaping the geomorphology of the passive northern GoM continental margin [*Worrall and Snelson*, 1989]. In regions underlain by mobile salt substrates, differential sediment loading can cause ductile substrate deformation over geological timescales [*Gemmer et al.*, 2004; *Schultz-Ela et al.*, 1993]. This deformation results in the upward migration of salt bodies, leading to the formation of salt domes and canopies [*Peel*, 2014]. Additionally, horizontal salt movement can also be driven by pressure gradients, governed by the competition between Couette (viscous fluid flow, driven by a shear stress, between two surfaces moving at different rates) and Poiseuille (viscous fluid flow, driven by external pressure gradients, between two surfaces not moving at different rates) flows along compressional margins [*Ings and Beaumont*, 2010]. Ultimately, mobile salt generates topographic variations (e.g., minibasins) along the seafloor that influence the fluid and sediment transport fields of turbidity currents [*Peel*, 2014; *Reece et al.*, 2024].

Geologic Setting: Northern Gulf of Mexico

The history of the GoM basin, analogous to other passive margins and/or salt basins such as those found in the South Atlantic salt basins, Red Sea, and southern Moroccan/Scotian margins [*Rowan*, 2022], dates to the early Mesozoic era. During this time, fault bounded basins formed across what is now a 400 km wide zone, resulting from the rifting of the supercontinent Pangaea [*Pindell and Dewey*, 1982]. During the late Triassic to early Jurassic period, intercontinental rifting began between the Yucatan and

North America [*Bird et al.*, 2005]. During rifting, the northern GoM margin experienced extensional forces that led to crustal thinning, ultimately resulting in the formation of transitional crust. Salt deposition began around 160 million years ago (Ma), shortly after intercontinental rifting began, giving rise to the Louann Salt formation [*Bird et al.*, 2005]. Prior to deformation, the Louann Salt was estimated to be at least 3 to 4 km thick near its center [*Hudec et al.*, 2013b], corresponding to the present-day Fill and Spill region of the northern GoM minibasin province. The formation stratigraphically pinches out towards the eastern and western basin boundaries [*Hudec et al.*, 2013b; *Steffens et al.*, 2003; *Salvador*, 1991]. The Louann Salt is a significant geological feature, and the movement of this salt controls much of the region's modern topographic variations and complexity [*Andrews*, 1960; *Hudec et al.*, 2013a]. During the late Jurassic, the Yucatan block rotation began, followed soon after by sea-floor spreading, basin subsidence, and generation of oceanic crust [*Bird et al.*, 2005]. Rifting ceased in the Cretaceous, and crustal lows and highs were formed along the GoM margin due to variations in extensional forces [*Eddy et al.*, 2014; *Eddy et al.*, 2018; *Ewing*, 2009; *Van Avendonk et al.*, 2015].

After the rifting phase, a second period of regional uplift occurred during the Late Cretaceous, coinciding with heightened tectonic activity and thermal doming resulting from mantle upwelling just north of the updip limit of salt in present-day Arkansas [*Ewing*, 2009]. These tectonic events, in conjunction with sediment influx from the hinterland, played a crucial role in shaping the evolution of Louann Salt into its current configuration [*Jackson and Seni*, 1983]. Density contrasts between the encapsulated salt and the surrounding clastic sediment matrix generated buoyant forces, facilitating upward salt mobility [*Martinez*, 1991]. Salt migration was not purely vertical, but also occurred laterally [*Ings and Beaumont*, 2010]. This lateral migration was driven by a combination of salt evacuation beneath zones of sediment deposition [*Gemmer et al.*, 2004], associated pressure differentials [*Ings and Beaumont*, 2010], and gravitational forces that moved much of the salt down dip towards the Sigsbee Escarpment [*Humphris Jr.*, 1979].

Many rivers transport sediment from the terrestrial to the ocean along the northern GoM margin. The largest and most significant being the Mississippi River, which transports a sediment load of 210 million metric tons per year to the northern GoM [*Blum and Roberts*, 2009; *Milliman and Syvitski*, 1992]. A summation of the modern loads of the largest nine rivers suggests an approximate delivery of 234 million metric tons per year to the northern GoM [*Milliman and Syvitski*, 1992]. Much of this sediment is deposited on the continental shelf but may be delivered through turbidity currents to the continental slope, with significant episodes of slope sediment deposition occurring over the last 160 Ma [*Galloway*, 2008]. These depositional episodes played a large role in mobilizing the Louann Salt, loaded by deposition of sediments ranging in grain sizes from clays to sands, and the basin being characterized as gravitationally active [*Colling et al.*, 2001; *Mattson et al.*, 2020; *West*, 1989]. At present, much of the Louann Salt is allochthonous, or moved from original state and emplaced above stratigraphically younger strata [*Wu et al.*, 1990], and is relatively thin along the northern portion of the continental margin. The Louann Salt thickens in the direction of the Sigsbee Escarpment, which is the leading edge of the prograding salt [*Slowey et al.*, 2003]. As the Louann Salt flowed and deformed, it influenced the formation of structures such as salt domes (i.e., salt masses intruded upward into overlying strata) and salt canopies [*Jackson et al.*, 1990;

Jackson and Talbot, 1989]. These structures, in turn, create localized accommodation for sediment deposition that are often the target for hydrocarbon exploration [*Wood and Giles*, 1982].

Regional mapping shows that most of the mature minibasins, or those basins that are fully filled, are ‘salt welded’, indicating that they cannot sink further into the underlying salt because pressure gradients have caused all the salt beneath subsiding minibasins to be evacuated [*Colling et al.*, 2001; *Galloway*, 2008; *Hudec et al.*, 2013a; *Ings and Beaumont*, 2010]. Salt welds required several kilometers of sediment accumulation in depressions to force the evacuation (of kilometer thicknesses) of salt [*Jackson and Cramez*, 1989]. These mature salt welded minibasins dominantly occur in the central portion of the minibasin province of the northern GoM, here termed the Fill and Spill region. Additionally, mapping the top of salt within this Fill and Spill region suggests that salt welded minibasins occur more often on the continental slope, closer to the continental break, than towards the Sigsbee Escarpment [*Colling et al*., 2001].

Subregion Characterization

The primary goal of this study is to characterize distributions of minibasin geometry (i.e., planform diameter, relief, area, and volume), derived from movement of the Louann Salt, and the complexity of nested depressions. To achieve this, we quantify and compare accommodation statistics in four subregions of the northern GoM margin. This study leverages prior research that defined these subregions through analysis of a drainage density map [*Steffens et al.*, 2003]. This map was produced by a drainage path analysis that routes pseudo-flow down steepest paths of descent [*Steffens et al.*, 2003]. These four subregions correlate with Louann Salt substrate thicknesses and are presented here by decreasing underlying salt thicknesses: Fill and Spill, Complex Corridors, and Unconfined Linear Pathways (Fig. 1) [*Steffens et al.*, 2003]. Here, the seafloor character of these subregions is attributed to underlying salt dynamics driven by differential sediment loading [*Gemmer et al.*, 2004], and pressure gradients resulting from lateral salt sheet movement in a compressional toe-of-slope environment [*Ings and Beaumont*, 2010]. The mobile Louann Salt largely generates the variability observed on the GoM margin's seafloor [*Hudec et al.*, 2013a], serving as the foundational first-order factor influencing the formation of drainage pathways identified and interpreted in prior research [*Steffens et al.*, 2003]. The Fill and Spill subregion is defined by drainage pathways that are generally < 20 km long before terminating in local depressions [*Steffens et al.*, 2003]. These paths often cluster within and near individual salt withdrawal intra-slope basins. Flanking the Fill and Spill subregion is the Complex Corridors West and Complex Corridors East subregions. These are characterized by more continuous but complex drainage corridors, with maximum dip extents of ~60 km; similar to Smith's (2004) 'connected tortuous corridors'. East of the Mississippi Canyon, *Steffens et al.* [2003] defined an Unconfined Linear Pathway subregion that contains dip-oriented drainage paths, or drainage paths following the regional slope gradient, up to ~130 km in length. This drainage texture, or pattern of drainage features on the landscape, occurs in a graded unconfined slope setting with little or no salt substrate.

Subregion Characterization – Adjusted Boundaries

To account for the specific impact of Steffens et al. [2003] defined boundary locations, this study also investigates how adjusting boundary locations between the four sub-regions (Fill and Spill, Complex Corridors West and East, and Unconfined Linear

Pathways) alters the statistical analyses of minibasin geometries (i.e., planform diameter, relief, area, and volume). For the first scenario, the Fill and Spill regional boundaries are expanded by 50 km (>> typical minibasins diameters) to ensure the sampling of additional minibasins outside of the original boundary, while all other regions are shrunken. For the second scenario, the Fill and Spill regional boundaries are shrunken by 50 km, while all other regions are expanded. These two boundary scenarios are used along with the normal boundary locations to assess the impact of specifically drawn regional boundary lines. Note, the Fill and Spill region was isolated specifically due to its size and center location, sharing boundaries with all other regions and making it a prime candidate to alter all boundaries for additional analyses. Ultimately, analyzing the suite of regional boundaries addresses the potential interpretative error introduced previously by Steffens et al. [2003] with the original normal sized sub-regions.

Water Depth Characterization

This study additionally explores how variation in water depth impacts minibasin geometry (i.e., planform diameter, relief, area, and volume). Specifically, the four ranges of water depths include: 57 to 1000 m, 1001 to 1600 m, 1601 to 2000 m, and 2001 to 3379 m. Note, these depth ranges are not uniform, but rather were selected to visually capture a similar number of minibasin samples for comparison purposes across the northern GoM dataset. The same analysis used for the sub-region characterization (Fill and Spill, Complex Corridors West and East, and Unconfined Linear Pathways) was used to quantify and compare accommodation statistics in the four water depth ranges of the northern GoM margin. This analysis aims to explore minibasin geometry and the potential impact of down margin gravitational and compressional variations of flowing salt towards the Sigsbee escarpment, with water depths greater than 3000 m.

DATA AND METHODS

BOEM Bathymetry Dataset

This study leverages a bathymetric dataset of 1.4 billion cells that are 12.19 x 12.19 m (Fig. 1) [*BOEM*, 2017]. This dataset was created by the Bureau of Ocean and Energy Management (BOEM) using a mosaic of 3-D seismic surveys (i.e., studies using seismic waves to image subsurface structures) over a 233,099 km^2 region and has an average vertical error of 1.3 percent of water depth, W_D, which ranges from 40 to 3380 m [*BOEM*, 2017]. Additionally, the average horizontal error is reported as 15.24 m [*BOEM*, 2017]. The dataset was used to extract minibasin reliefs (i.e., maximum depths), planar surface areas, and volumes of depressions across the entire northern GoM margin and then for each of the four subregions (Fig. 1). Prior quantification of ponded accommodation on the northern GoM margin by Steffens et al. [2003] used a bathymetric map with a 200-250 m node spacing, thus a resolution ~16-20 times coarser than the BOEM dataset.

Primary Depression Extraction and Geometries

The full BOEM bathymetric dataset was used to quantify distributions of depression geometric scales. An *ArcGIS Pro Sink* geoprocessing function [*Mark*, 1988] was employed to identify and extract sinks (topographic lows) within the raster dataset. Sinks were identified by detecting topographic lows and expanding upward and outward in search of a spill point. Specifically, this study extracted sinks from the raster dataset with areas greater than 62,500 m^2 and maximum reliefs exceeding 1 m. The area cutoff value, which corresponds to a region that is 250 m in width and length, was set to avoid apparent depressions that result from pixel-to-pixel error in the BOEM map. The 5 m relief cutoff value is less than the absolute vertical resolution of much of the dataset, reported as 1.3% of water depth [*BOEM*, 2017]. However, some of this error is associated with merging seismic datasets collected in different years by different geophysical companies, resulting in cross-survey offsets. As a result, accuracy varied between surveys, but within survey precision is generally well below 1.3% [*BOEM*, 2017]. As most depressions are contained within the footprint of individual seismic surveys, geometric statistics or the measurements related to the shape and size of features, can generally be accurately estimated for depressions with reliefs less than the reported absolute bathymetric error. Post-extraction analysis suggests consistent probability scaling of depression geometry begins for depressions larger than our 5 m limit, which we take as an indication of precision in defining geometry statistics.

The *ArcGIS Pro Sink* function identifies maximum depths within neighboring cells that have higher elevations. Next, a filling process occurs to determine the maximum area of each identified depression, which is set by the planar area contained below the depression spill point [*Planchon and Darboux*, 2002]. Outputs from this sink extraction process are polygons that cover the surface area of each local depression [*Mark*, 1988]. Lastly, bathymetric data underlying each of the polygons was saved as a raster file, allowing bathymetry to be analyzed for volumetric calculations below each surface area polygon. Extracted depressions were then sorted into one of the four subregions defined by Steffens et al. [*2003*]. The four regions were replicated in *ArcGIS Pro* as polygons that overlap the extent of the BOEM bathymetry dataset (Fig. 1) allowing depressions to be tied to polygons (i.e., subregions). Geometric statistics are generated for: 1) maximum relief, defined as the greatest vertical relief between the depression floor and spill point, 2) planar nominal diameter, defined as the average diameter of the horizontal surface resulting from a filled depression, 3) planar surface area, defined as the area of the horizontal surface resulting from a filled depression, and 4) ponded volume, defined as the volume between the seafloor and the horizontal surface resulting from a filled depression.

Depression Density Calculations

To compare the abundance of depressions between subregions, a depression count was made for each of the four subregions. A comparison of depression density, *DD*, between regions was accomplished with three methods. The first normalized depression counts, n_D, by the planar area of a subregion, $A_{subregion}$

$$DD_{normalized} = \frac{n_D}{A_{subregion}}, \quad \text{[EQ. 1]}$$

and as such did not factor in the planar area of individual depressions. The second method calculated the fraction of a region covered by enclosed depressions, R_{fc}, by summing all depression planar surface areas in a subregion, A_p, and dividing by the subregion's planar area, $A_{subregion}$,

$$R_{fc} = \frac{\sum_{i=1}^{n} A_{p_i}}{A_{subregion}}. \quad \text{[EQ. 2]}$$

Ponded Accommodation

A final method to compare the density of depressions in subregions calculates the average thickness (m) of ponded accommodation in a subregion, PA_{at}, by summing the ponded accommodation of all depressions in a subregion, *PA*, and normalizing by the subregion's planar area.

$$PA_{at} = \frac{\sum_{i=1}^{n} PA_i}{A_{subregion}}. \quad \text{[EQ. 3]}$$

This approach involves certain simplifying assumptions, such as the identified boundaries between subregions, which may introduce uncertainty into the results because subregions vary in spatial extent.

Next, to quantify the importance of large vs. small depressions in the total ponded accommodation of a region, plots of the fraction of a subregion's ponded accommodation (a function of primary depression volumes, V_D) residing in depressions that exceed a given maximum relief, R,

$$F_A(R > r) = \frac{\sum_{i=1}^{n} V_{D_i}(R>r)}{\sum_{i=1}^{n} V_{D_i}}, \quad \text{[EQ. 4]}$$

nominal planar diameter, D,

$$F_A(D > d) = \frac{\sum_{i=1}^{n} V_{D_i}(D>d)}{\sum_{i=1}^{n} V_{D_i}}, \quad \text{[EQ. 5]}$$

area, A,

$$F_A(A > a) = \frac{\sum_{i=1}^{n} V_{D_i}(A>a)}{\sum_{i=1}^{n} V_{D_i}}, \quad \text{[EQ. 6]}$$

and/or volume, V,

$$F_A(V > v) = \frac{\sum_{i=1}^{n} V_{D_i}(V>v)}{\sum_{i=1}^{n} V_{D_i}}, \quad \text{[EQ. 7]}$$

are generated. This analysis was also conducted for the full northern GoM dataset. Nominal planar diameter of depressions was calculated as

$$D = 2\sqrt{\frac{A}{\pi}}, \quad \text{[EQ. 8]}$$

where A is the planar surface area of a depression.

Nested Depression Hierarchy

A nested-level hierarchy analysis was utilized to quantify the propensity for depressions to be nested within larger depressions, which is a proxy for topographic complexity. This analysis was completed for all four subregions of the northern GoM. A *Python* package named *lidar*, developed for terrestrial settings, was used to delineate nested level depressions from the *ArcGIS Pro Sink* raster output using a 5 m minimum depth, and a 5 m slicing interval (i.e., vertical spacing between successive layers used in analysis) [*Wu*, 2021; *Wu et al.*, 2019]. This algorithm follows a similar methodology to Le and Kumar [*2014*]. First, base level depressions (lowest depressions in the hierarchy) are identified by the lowest elevation cells relative to their surrounding cells and tracked up to a localized rim with one cell acting as a spill point. Depressions below this spill point are considered Level 1 depressions (Fig. 2). It is important to note that spill points designate the top of all depression nested levels. Two Level 1 depressions that share a common spill point merge above into a Level 2 depression (Fig. 2). Further, Level 2 depressions that share a spill point with other Level 2 or Level 1 depressions continue to grow up the hierarchy chain to become Level 3 depressions (Fig. 2). The depression with the highest level of hierarchy is referred to as the 'primary depression'. This process continues until a regional spill point is reached, in which flow emanating from the depression would descend the regional slope until another primary depression is reached (Fig. 2).

RESULTS

Total Ponded Accommodation and Basin Floor Slopes in Northern GoM

Volumes from all extracted basins in the bathymetry dataset were summed to find the margins total ponded accommodation. This was calculated to be 1.62 x 10^{13} m^3 for the northern GoM margin.

Basin Floor Slopes as a Proxy for Salt Dynamics in Northern GoM

Basin floor slopes are used as a proxy to assess the extent of regional and localized variations of salt flow forces acting on minibasins. A 3 x 3 cell moving window was used in an *ArcGIS Pro Slope* geoprocessing function to calculate the seafloor gradient within all ponded accommodation in the northern GoM margin and found that depressions generally have sloping basin floors with most gradients less than 2 degrees (Fig. 3). The gradient of the seafloor in depressions are similar across all subregions of the GoM margin, indicating all regions are impacted equally by the relative recent timing of regional salt dynamics. Notably, higher slope gradients typically occur around the perimeter of minibasins in the Fill and Spill region, confirming the presence of more mature salt-welded minibasins and a more pronounced impact of local salt-withdrawal on this region.

Depression Densities

The Fill and Spill region has the largest number of primary depressions with a total count of 7207, in a subregion with an area of 107,142 ± 498 km^2 (Fig. 4), thus an approximate density of 0.054 depressions/km^2. Depression density decreases in the Complex Corridors Regions to the west (n = 1185; 0.039 depressions/km^2) and east (n = 154; 0.009 depressions/km^2) of the Fill and Spill region. The Unconfined Linear Pathways region has 429 primary depressions, and the lowest depression density of 0.005 depressions per km^2 (Fig. 4). Utilizing the planar areas of all depressions, the fraction of each subregion covered by depressions is estimated. This follows a similar, but accentuated, trend as the depression density. 78% of the Fill and Spill region is covered by depressions, decreasing to 5 and 2 % in the West and East Complex Corridors regions, respectively. Finally, only 0.5% of the Unconfined Linear Pathway Region is covered by depressions (Fig. 4C).

Statistics of Depressions and Their Ponded Accommodation

Probability of exceedance, or the likelihood of surpassing a certain threshold, was calculated for maximum relief, nominal planar diameter, area, and volume of depressions. This was done first for the entire northern GoM, and then for each of the four subregions, and for each of the four water depth classifications (Figs. 5, 6, & 7). In all distributions, data follow an approximate log-log linear decay over most of the parameter space, which spans several decades for each geometric variable. This log-log linear decay transitions to an approximate exponential decay for extremely large depressions, when considering the margin as a whole, the Fill and Spill region, or for all water depth ranges analyzed. However, the log-log linear decay is not perfect. For example, when considering the whole margin, a kink exists in the decay of all four geometric parameters (e.g., near 50 m for the depression relief distribution), with a higher power-law slope transitioning to a lower slope as depression scale increases, suggesting enhanced organization of large, relative to small, depressions at the scale breaks. While we observe evidence of this kink, we are unaware of a distribution class that contains two power-law scaling regimes and a truncation parameter. As such, this analysis characterizes the distribution shape using both a Pareto distribution and a truncated

Pareto for all datasets. Future research could focus on quantifying these scale breaks and clarifying their underlying causes.

Power-law distributions, which follow a log-log linear decay in the probability of exceedance of a random variable, are a common occurrence in a wide array of natural phenomena, including earthquake magnitudes, sizes of cities, daily fluctuations in the size of financial market indexes, and biological populations [*Bak and Tang*, 1989; *Clauset et al.*, 2009; *Gabaix et al.*, 2003; *Kagan*, 2010; *Newman*, 2005; *White et al.*, 2008]. These statistical distributions can indicate underlying processes or mechanisms that give rise to rare but impactful entities or events [*Pinto et al.*, 2012]. The Pareto is a common power-law distribution, which is characterized by a probability of exceedance of the form

$$P(X > x) = \left(\frac{\gamma}{x}\right)^{\alpha}, \qquad \text{[EQ. 9]}$$

where x is the random variable, γ is the minimum possible value of the random variable, and α is the exponent of the power-law decay and is also known as the tail index [*Newman*, 2005].

Results for the margin as a whole, the Fill and Spill Region, and for all water depth ranges, suggest that at exceptionally large scales the probability of exceedance decreases with an exponential trend (Figs. 5, 6, & 7), suggesting a finite size influence on the shape of the distribution. This trend can be well described by a truncated Pareto distribution of the form

$$P(X > x) = \frac{\gamma^{\alpha}(x^{-\alpha} - \nu^{-\alpha})}{1-(\gamma/\nu)^{\alpha}}, \qquad \text{[EQ. 10]}$$

where ν is the truncation parameter or the upper bound on the random variable, α is the tail index and γ is the lower bound on the random variable x [*Aban et al.*, 2006; *Ganti et al.*, 2011].

Free parameters that define the Pareto and truncated Pareto fits to all distributions were found using the maximum likelihood estimation method [*Aban et al., 2006*] (Figs. 5, 6, & 7). All estimated parameters for Pareto and truncated Pareto fits for the entire northern GoM dataset are reported in Table 1. Additionally, Table 2 reports all estimated parameters for Pareto and truncated Pareto fits across normal, expanded, and shrunken sized subregions, as well as four water depth ranges.

The Fill and Spill region is the only subregion whose distributions show clear exponential decay at large parameter values and thus seem to follow truncated Pareto distributions (Fig. 6). However, we also fit data from the other regions with truncated Pareto distributions for completeness (Fig. 6).

A comparison of the tail index as a function of the dimensionality of the depression scale (maximum relief or nominal planar diameter [L], area [L^2], and ponded volume [L^3]) and subregion show the following trends. Generally, as the dimensionality of the scale increases, the tail index decreases (Fig. 8). Tail indexes range from 1.06-2.05 for maximum depression diameters, which drops to 0.84-1.76 for depression reliefs, then down to 0.53-1.02 for depression areas, and then to 0.33-0.82 for depression volumes. Next, for all geometric scales, the Fill and Spill region has the lowest tail indexes, which increase as one traverses into the Complex Corridors Regions, and then into the Unconfined Linear Pathway subregion (Fig. 8).

The tail index of a Pareto distribution carries significance for our ability to characterize the mean state of a random variable. When $\alpha > 2$, the distribution possesses a statistical mean, and when $\alpha > 3$, there exists a statistical variance [*Newman*, 2005]. However, when $\alpha < 2$, a distribution lacks a statistical mean [*Deluca and Corral*, 2013], as the possibility of sampling a parameter of near infinite size is statistically significant. Distributions with tail indexes < 2 are often discussed as having 'heavy tails', as extremely high parameter values are more probable than in a normal distribution [*Kolmogorov*, 2018]. Truncated Pareto distributions with tail indexes < 2 also are considered to possess a heavy-tail, even though the distribution prevents the sampling of near infinite values [*Deluca and Corral*, 2013]. A key result here is the presence of $\alpha < 2$ in almost all dimensionality scales of the northern GoM depressions, which also occurs in all subregions and water depth ranges (Figs. 5-8). The only exception is a lone value for the ULP region's depression planar nominal diameter that has a value just exceeding 2 (Figs. 6 & 8). Tail indexes reported above, and within figures that compare tail indexes across subregions, are from the standard Pareto distribution fits. However, we note that tail indexes generated from truncated Pareto fits are always less than those estimated from Pareto distributions (Fig. 9). Given that some of our distributions appear well fit by truncated Paretos, this further supports the characterization of most all geometric datasets as heavy-tailed (Fig. 9).

Ponded Accommodation Statistics

The average thickness of ponded accommodation in the four subregions highlights the ability of mobile salt beneath the Fill and Spill Region to generate significant space to store sediment. The Fill and Spill region is on average covered by

136 m of ponded accommodation, which falls to between 0.2 – 1.0 m over the Complex Corridors regions and further down to only 0.03 m over the Unconfined Linear Pathways subregion (Fig. 4D).

Plots of the fraction of ponded accommodation housed in depressions exceeding a given scale (either maximum relief, planar diameter, area, or volume) highlight the importance of large depressions to the total ponded accommodation on this margin (Fig. 10). Trends for all four parameters, for the full margin and/or individual subregions, follow a very slow decay with increasing depression scales (Figs. 10 & 11), but with very rapid fall-off at large depression scales. To highlight the importance of large depressions, we find that 90% of the ponded accommodation on the northern GoM margin resides in volumetrically the largest 147 of the 8153 identified depressions. These depressions all have maximum reliefs greater than 273 ± (1.3% x W_D) m.

Regional: Nested Complexity

Quantification of depression nested complexity by region highlights potential relationships between depression scales and topographic complexity. The Fill and Spill region, which had the largest depression scales and heaviest distribution tails, stands out as the most complex. The depression with the most complexity in this region has 37 nested depression scales, a result that highlights that larger depressions typically have more hierarchical levels (Fig. 12A). The Complex Corridors West region, which holds the second-highest degree of nested depression complexity, had a maximum of 11 level depression scales in a single primary depression. The Complex Corridors East region is characterized by a maximum of 5 level depression scales. The Unconfined Linear

Pathways region has the least complexity of all subregions, with a maximum of 3 level depression scales.

Distributions of nested levels in depressions by subregion also follow power-law decay in probability of exceedance (Fig. 12A). Like distribution statistics for depression geometric scales, the tail-indexes of the nested level distributions in the Fill and Spill and Complex corridors have heavy tails (tail indexes between 1.12-1.53) (Fig. 12B) and the lowest tail-index is found in the Fill and Spill subregion. Confirmation of distribution class is difficult for the Unconfined Linear Pathway subregion, as we observe a maximum of 3 nested levels, but the tail index for this region might be as high as 2.26.

DISCUSSION

Basin Scale Ponded Accommodation

Large topographic depressions have the capacity to trap turbidity currents on their downslope traverse of continental margins [*Lamb et al.*, 2006]. This results in a unique set of flow dynamics within minibasins and ultimately the accumulation and retention of sediment, nutrients, and pollutants [*Dorrell et al.*, 2018; *Galy et al.*, 2007; *Kane et al.*, 2020; *Lamb et al.*, 2006; *Masson et al.*, 2010; *Stetten et al.*, 2015; *Talling et al.*, 2024]. Results reveal that a significant portion of the ponded accommodation is concentrated in a small subset of the very largest depressions. For example, 90% of the ponded accommodation on the margin resides in the deepest 147 depressions, which all have reliefs more than 273 ± (1.3% x W_D) m. This depression scale is likely sufficient to trap the largest turbidity currents that move down the GoM margin.

Prior literature states that seafloor depressions and associated ponded accommodation can affect turbidity currents by either promoting the total collapse of a current or initiating a hydraulic ponding process within enclosed topography [*Patacci et al.*, 2015; *Toniolo et al.*, 2007; *Toniolo et al.*, 2006b]. A collapse of a turbidity current can occur if the reduction in sediment transport capacity leads to sufficient sediment deposition from the flow as it traverses a low, flat, or adverse slope [*Lamb et al.*, 2004]. This reduces the gravitational driving force, which can stall and collapse a flow [*Dorrell et al.*, 2018; *Kneller and Buckee*, 2000]. A hydraulic ponding process may develop if flows traverse the minibasin floor and reflect off the distal basin slope. This reflection can induce a flow transition from Froude critical, where flow velocity equals the wave velocity, to subcritical conditions, allowing sediment laden suspension flows to inflate and circulation cells to distribute sediment throughout minibasins [*Patacci et al.*, 2015; *Reece et al.*, 2024]. The ponding process promotes the deposition of sediment from the low densimetric Froude flows. Ponding is thought to occur for flows that are capable of traversing the floor of minibasins and which have comparable thickness to the minibasin relief [*Lamb et al.*, 2006; *Toniolo et al.*, 2007]. Results suggest that much of the ponded accommodation (i.e., minibasins) on the northern GoM margin should be capable of inducing either flow collapse or hydraulic ponding of turbidity currents, even for the expected thickest currents traversing down the margin (Figs. 1, & 10A). While no active turbidity currents in GoM minibasins have been measured, turbidity currents have been recorded in other settings; e.g., in the Monterey Canyon [*Xu et al.*, 2004] and in the Zaire submarine channel [*Talling et al.*, 2022]. Recorded flows at these sites have not exceeded 60 m. Self-formed and aggradation channels along other margins, e.g., Amazon [*Pirmez and Imran*, 2003] and Bengal [*Kolla et al.*, 2012] submarine GoM margin, self-formed and aggradational channels up to 40 m deep have been observed entering or traversing minibasins [*Badalini et al.*, 2000]. Experiments suggest that turbidity currents can have thicknesses that are 1.3 times the depth of the channel that is guiding them still act as channelized flows [*Mohrig and Buttles*, 2007]. Taken together, measurements of active flows, imaging of modern and ancient channels, and results from experiments suggest that most, if not all, flows interacting with GoM minibasins would have had thicknesses less than the relief of depressions that house most of the ponded accommodation on the margin. Thus, most of the ponded accommodation in the northern GoM has the potential to either cause turbidity currents to collapse or hydraulically pond.

Topographic Self-Organization

A self-organized interplay between sediment loading, minibasin development, and salt remobilization crafts the bathymetry of the northern GoM [*Colling et al.*, 2001]. Self-organized systems are ones linked to the spontaneous emergence of a large-scale ordered pattern through small-scale interactions between components of a system [*Ashby*, 1947; *Hallet*, 1990; *Sornette*, 2006]. For salt-provinces, the pattern is the field of large-scale depressions (minibasins) that developed from differential loading of an initial salt sheet, where even minor spatial variations in loading or variations in initial salt thickness could set off a positive feedback loop where a change leads to further similar changes [*Marković and Gros*, 2014]. As a result, some depressions grow faster than others, resulting in depression capture and spatially variable rates of salt convection and expulsion. An attribute of self-organized systems is their resiliency to perturbations, linked to an ability to self-repair. This is attributed to external drives and internal dynamics competing on similar time scales [*Marković and Gros*, 2014]. In the northern GoM, the external driver can be thought of as glacio-eustatic sea-level changes, resulting in depositional episodes on the slope ("depisodes" of *Galloway et al.*, 2000) that are sufficiently separated in time to allow for the salt to deform in response [*Hudec and Jackson*, 2007]. This self-organization has been linked to the coalescence of hierarchically-scaled adjacent minibasins [*Colling et al.*, 2001]. While interaction of minibasins with one another has been hypothesized from subsurface imaging and explored in numerical and physical experiments [*Callot et al.*, 2016; *Fernandez et al.*, 2020], quantitatively linking these interactions to self-organization of the bathymetry is limited. However, self-organized systems often display power-law scaling of elements or dynamics in the system, where the weight of the distribution tail is linked to the degree of self-organization [*Marković and Gros*, 2014]. For minibasins, this can be thought of as follows: Coalescing of small-scale depressions into larger depressions redistributes probability within a distribution of minibasin size from small to large scales, in essence adding weight to the distribution tail. As such, the Pareto tail-index should inversely scale with the strength of self-organization in bathymetry due to the dynamics of salt in response to sediment loading.

We observe a change in self-organization spatially from East to West across the northern GoM, but do not see this same change in relation to water depths (Figs. 6, 7, 8, & 12; Table 2). More specifically, results herein document an increase in self-organization over the Fill and Spill subregion relative to neighboring subregions. This is found though the exceptionally low distribution tail-indexes over the Fill and Spill region, relative to all other regions (Figs. 6, 8a, & 12B; Table 2). These observations indicate that minibasins are indeed interacting with one another and merging to form channels, have reliefs exceeding 100 m, suggesting some flows that are at least this thick. Along the northern

larger depressions, a phenomenon supported by findings from offshore Angola that show minibasins interactions in numerous two-way travel time structure maps and seismic sections [*Ge et al*., 2019]. Previous studies have also noted the presence of ‘twin’ minibasins adjacent to each other overlying locations of thick salt [*Ings and Beaumont*, 2010], providing potential evidence of initial conditions prior to minibasins merging. These types of observations from present day seafloor structure maps and subsurface seismic slices of minibsains offer only a snapshot in time, but together provide an evolutionary record of the dynamic merging behavior in mobile substrate minibasins with substantial underlying salt thicknesses. The merging of minibasins is closely tied to locations with thick underlying salt, likely due to the potential these conditions provide for localized salt movement and ultimately larger minibasin dimensions. Thiner salt areas have minimal localized salt movement and thus limited potential for minibasin growth. The merging of minibasins is a traditional tell-tale sign of self-organizing behavior [*Marković and Gros*, 2014], and results suggest a likely response to initial underlying salt thickness. Enhanced depression interaction and merging over the region with the greatest underlying salt thickness has direct implications for increasing the sediment trapping potential of minibasins, furthering the positive feedback loop. Not only are the tail-indexes less over the Fill and Spill subregion, but this region also has the largest and most complex depressions (Figs. 6 and 12A).

Unlike the Fill and Spill region, it is worth noting that results indicate a potential non-Pareto distribution for the geometric depression scales of the Unconfined Linear

Pathways region (Figs. 1 & 6). Rather, the Unconfined Linear Pathways distributions are somewhat convex upward when viewed in log-log space, suggesting possible exponential distributions (Fig. 6).

The size of minibasins, for either the Fill and Spill subregion or the margin as a whole, appear to be limited by a finite size effect (Figs. 5 & 6). The upper limit on minibasin size is captured by the truncation parameters (v) (Tables 1 & 2). We hypothesize that this finite size effect is set by the size of turbidite lobes, or submarine deposits formed by turbidity currents, that load the margin, coupled to sufficient subsurface salt that can be evacuated to generate a depression in response. For example, a global compilation of geometric data that describes turbidite lobes in both unconfined and confined regions [*Pettinga et al.*, 2018] show similar maximum lobe area of approximately 10^9 m^2, which is also approximately the truncation parameter for depression area in our database. Assuming that depression side wall slopes are relatively similar for small and large depressions (our data suggests side wall slopes do have a weak tendency to steepen as depression size increases), then the area truncation scale would also limit the depression relief, nominal diameter, and volume distributions. This hypothesis is supported by physical experiments, where surface depression size rarely significantly exceeds the planform size of a sediment load placed on a proxy salt sheet [*Callot et al.*, 2016].

Significance of Minibasin Size and Nested Complexity

Findings suggest that there is a correlation between minibasin size and nested complexity in the northern GoM, which is most noticeable in the Fill and Spill region (Figs. 1, 6, 11, & 12). As the size of primary depressions increases, we observe an increase in the complexity of the depressions as suggested by the number of nested levels (Fig. 12). This suggests that turbidity currents must interact with multiple roughness scales within the largest minibasins. This increased complexity implies that sediment transport involves flows running up adverse slopes, those slopes that oppose the primary direction of flow, frequently translating kinetic energy (associated with motion) into potential energy (associated with position or configuration), thus losing their sediment transport capacity within many primary minibasins [*Dorrell et al.*, 2018; *Patacci et al.*, 2015]. Adding more complexity (e.g., numerous counter slopes) leads to enhanced ponding of turbidity currents, and thus sedimentation processes, compared to cases where primary depressions consist of a single level of complexity (Figs. 2 & 12) [*Oshaghi et al.*, 2013].

CONCLUSIONS

This investigation of the northern GoM bathymetry quantifies the total volume of ponded accommodation on the margin as well as distributions that describe the scales of depressions that house this accommodation, with implications for the depressions to trap turbidity currents and insights to the self-organization in salt provinces. This study reveals the following key findings:

1) The northern GoM margin houses a total ponded accommodation of approximately 1.62×10^{13} m^3.
2) Results find that 90% of the ponded accommodation in the northern GoM resides in the volumetrically largest 147 of the 8153 identified depressions, with maximum reliefs greater than 273 ± (1.3% x W_D) m. Thus, most of the ponded accommodation

in the northern GoM is capable of trapping and hydraulically ponding the full range of turbidity current sizes that might flow down the northern GoM margin.

3) Self-organization of bathymetry in the northern GoM bathymetric dataset is further supported by heavy-tailed distributions that describe the geometry of depressions on the margin. The weight of distribution tails, as quantified through best-fit tail-indexes, is greatest over the Fill and Spill region, which is underlain by the thickest salt deposits. This suggests a strong interaction of depressions over time, including depression growth through mergers. At the regional scale, these distributions are truncated, which suggests a finite size effect. We hypothesize that the maximum scale of turbidite lobes sets the truncation scales of minibasins on this margin.

4) The Fill and Spill region in the northern GoM reveals a clear association between minibasin size and nested complexity, with the largest minibasins exhibiting the greatest nested complexity. Turbidity currents entering the largest minibasins thus encounter a range of roughness scales, many of which are sufficient to induce hydraulic ponding of flows and reduce sediment transport capacity.

LIST OF FIGURES

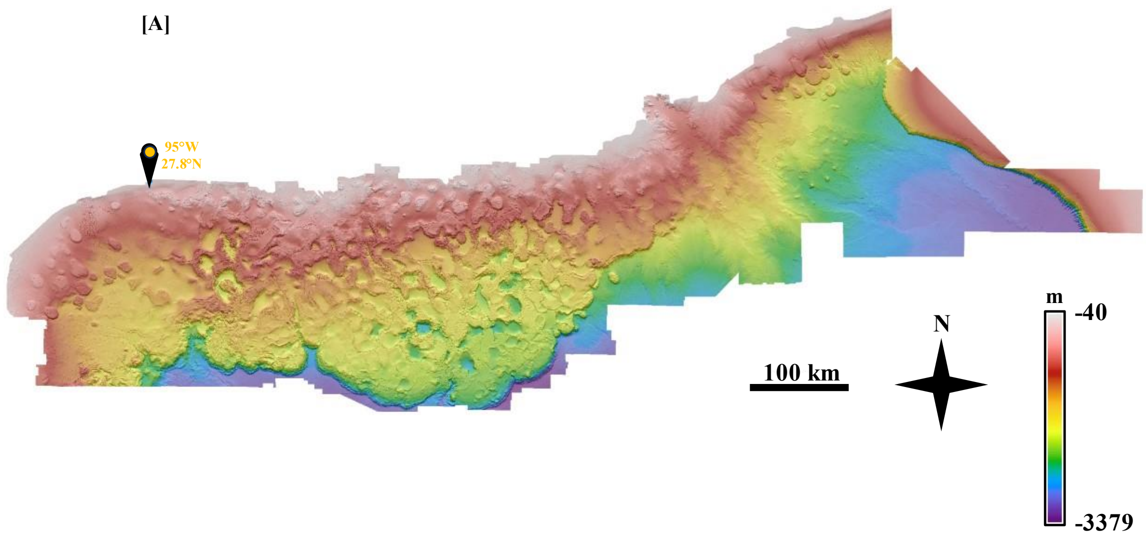

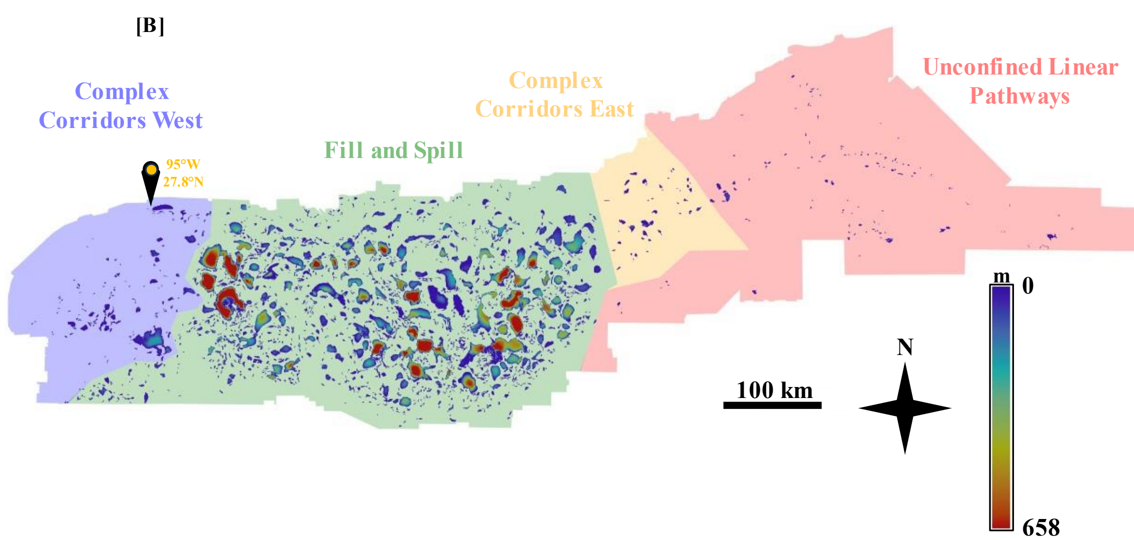

Figure 1. [A] BOEM's northern Gulf of Mexico deepwater bathymetry dataset, displayed with WGS84 projection [BOEM, 2017]. The dataset is a grid created from 3D seismic surveys and is comprised of 1.4 billion 12.19-by-12.19 m cells. Shaded relief overlays colored bathymetry and is vertically exaggerated by a factor of five. [B] ArcGIS Pro extracted local depressions with their shaded relief (polygons) in the northern GoM using BOEM's bathymetry dataset [BOEM, 2017]. The dataset covers much of the northern GoM continental margin with much of it underlain by the Louann Salt mobile substrate.

Four regions (colored) follow those outlined by Steffens et al., 2003, as they overlap with the BOEM bathymetry dataset.

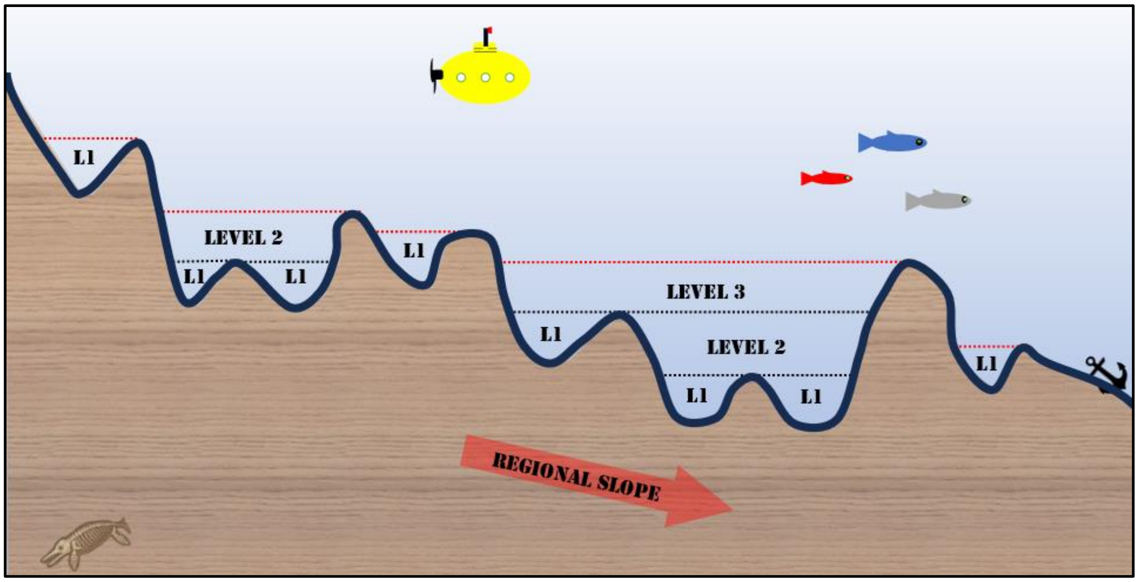

Figure 2. Schematic diagram showing topographic nested level hierarchy of seafloor depressions. Gray dotted lines represent spill point heights for each level. Red dotted lines indicate primary depressions that contain lower nested level depressions. Level 3 is the highest level in this schematic with the lowest hierarchy the base Level 1 depressions. Regional slope is from left to right and is annotated as a red arrow on the schematic diagram. Note: Level 1s are abbreviated as 'L1' on the diagram.

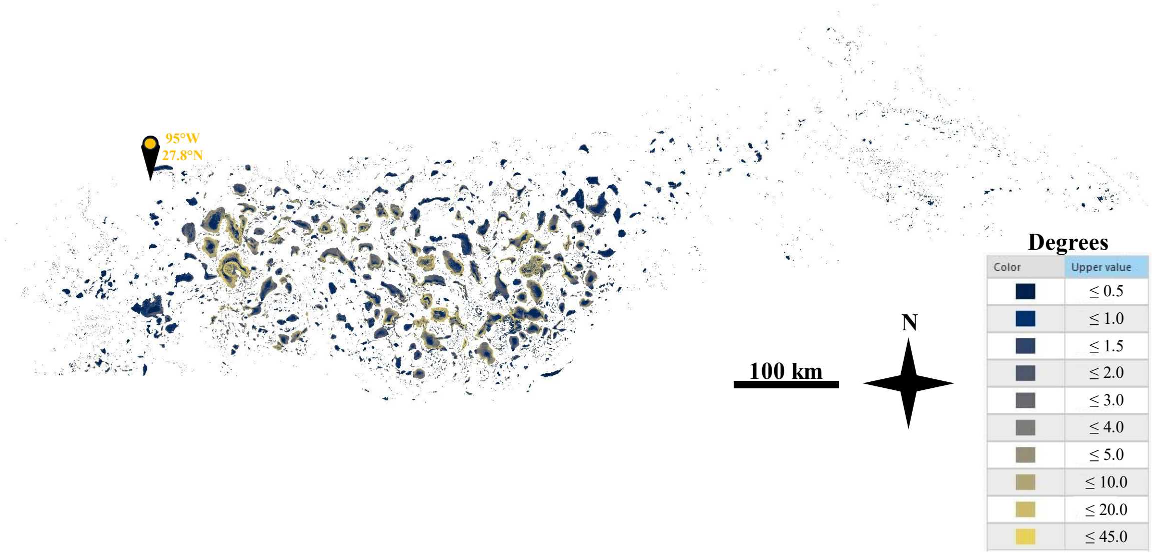

Figure 3. Slope map for all extracted seafloor depressions in the northern Gulf of Mexico margin, displayed with a WGS84 projection. Cooler colors represent lower degrees of slope and warmer colors depict higher degrees of slope. An ArcGIS Pro Slope geoprocessing function was used with a 3 x 3 cell moving window to calculate degrees of slope for all topography contained within seafloor depressions.

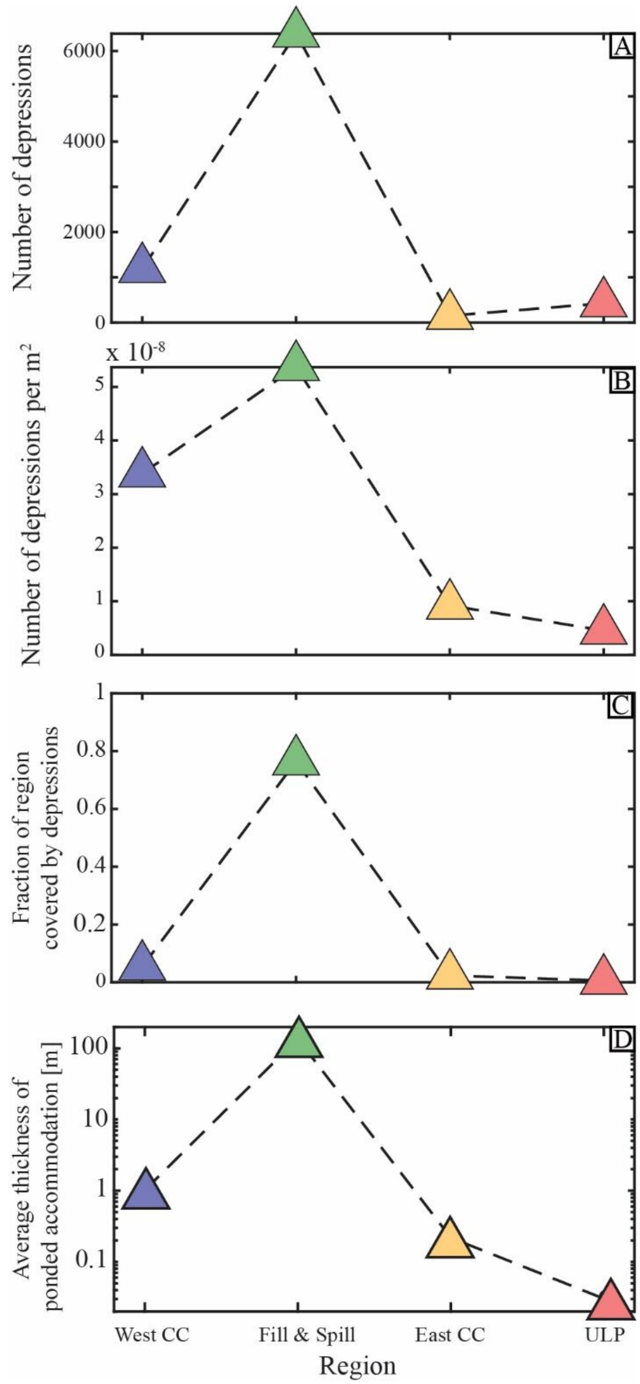

Figure 4. Plots showing regional variations of [A] number of depressions extracted, [B] number of depressions per m^2, and [C] fraction of region covered by depressions and [D] Average thickness of ponded accommodation in a region.

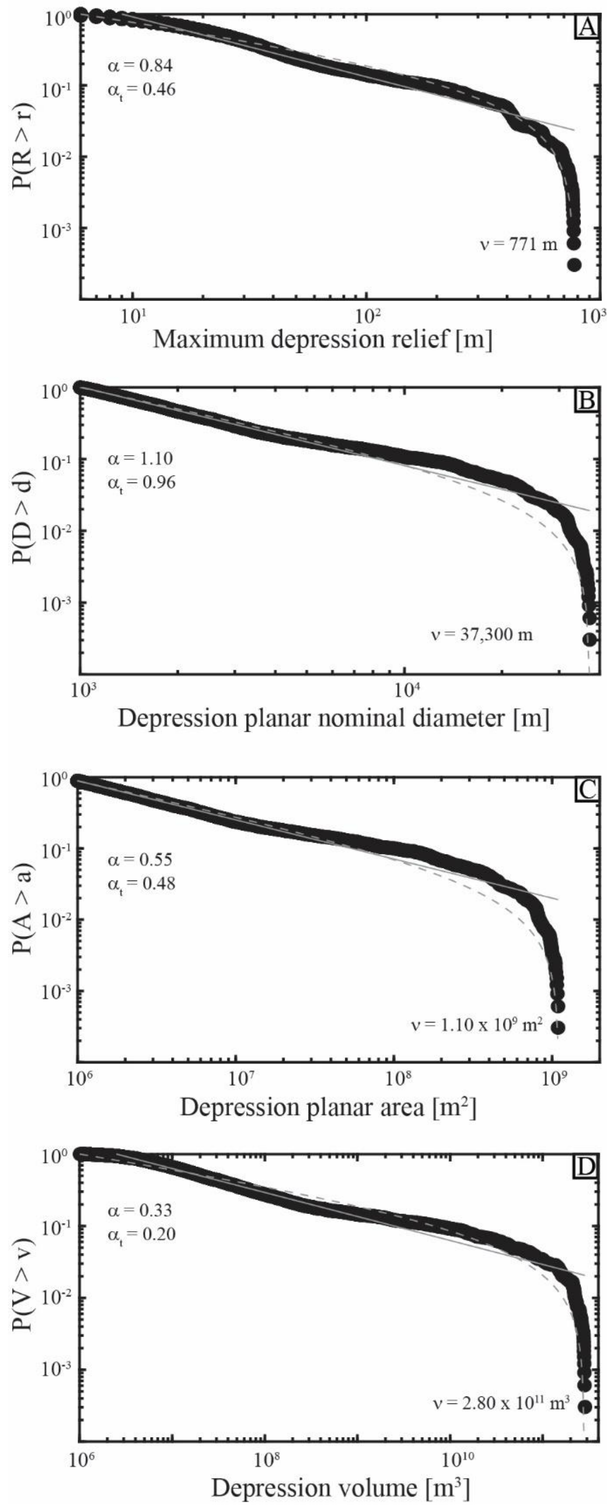

Figure 5. Plots showing probability of exceedance for depressions greater than a specific value for full northern GoM depression dataset, where [A] is maximum depression relief, [B] is nominal planar depression length, [C], is depression planar area, and [D] is depression volume. Note, the dataset is plotted in log-log space, and both the fitted

theoretical Pareto (solid lines) and truncated Pareto distributions (dashed lines) are overlayed.

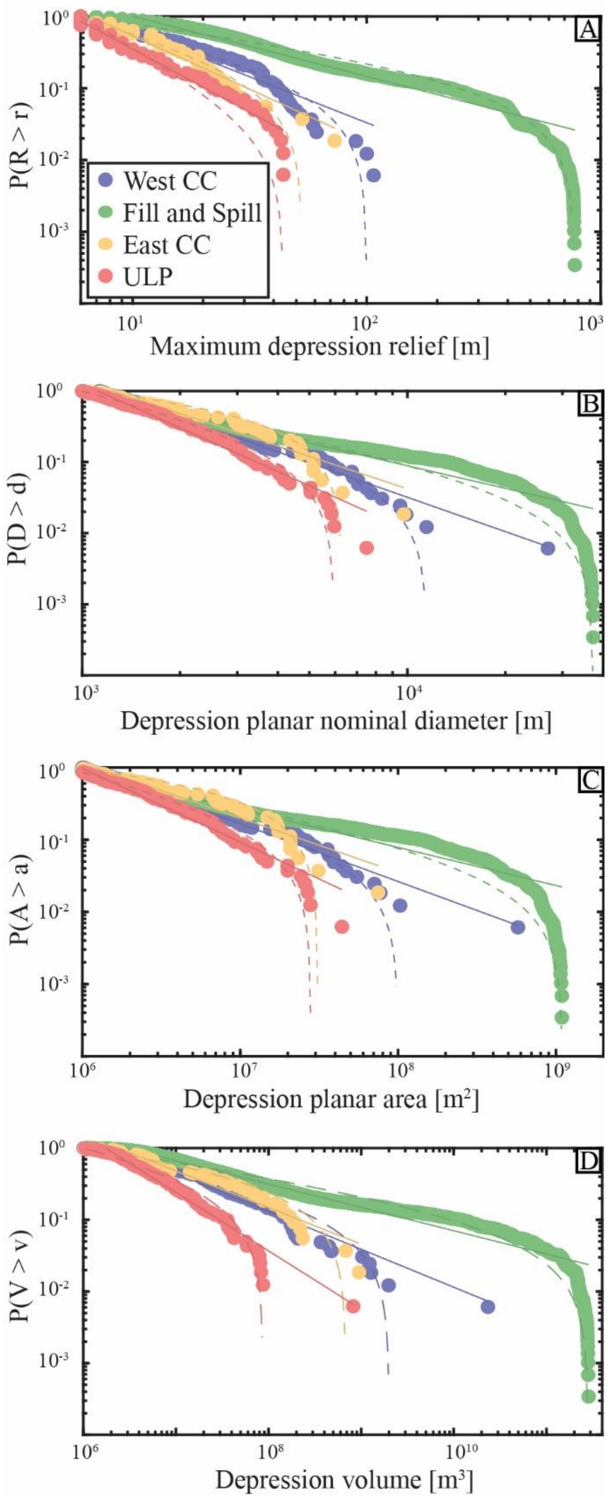

Figure 6. Plots showing probability of exceedance for depressions greater than a specific value for subregions, where [A] is maximum depression relief, [B] is nominal planar depression length, [C] is depression planar area, and [D] is depression volume. Note, regional datasets are plotted in log-log space. Note, the dataset is plotted in log-log space,

and both the fitted theoretical Pareto (solid lines) and truncated Pareto distributions (dashed lines) are overlayed.

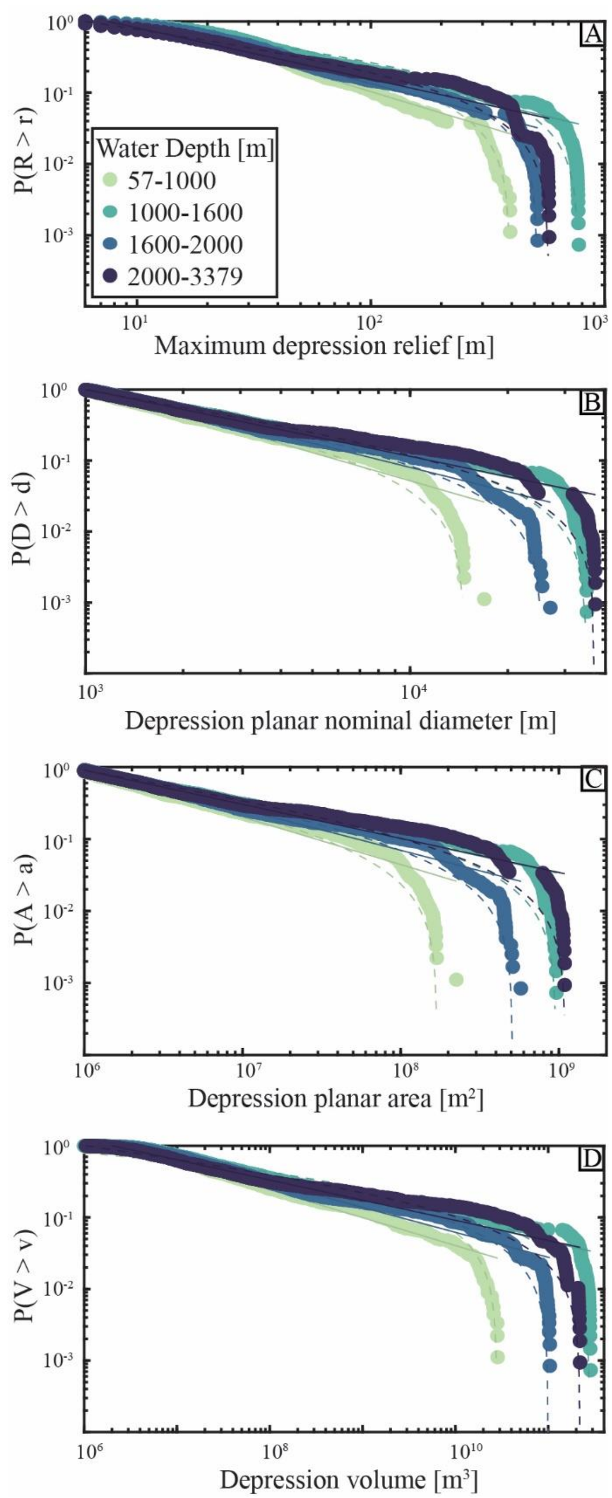

Figure 7. Plots showing probability of exceedance for depressions greater than a specific value for water depth, where [A] is maximum depression relief, [B] is nominal planar depression length, [C] is depression planar area, and [D] is depression volume. Note, water depth datasets are plotted in log-log space. Note, the dataset is plotted in log-log

space, and both the fitted theoretical Pareto (solid lines) and truncated Pareto distributions (dashed lines) are overlayed.

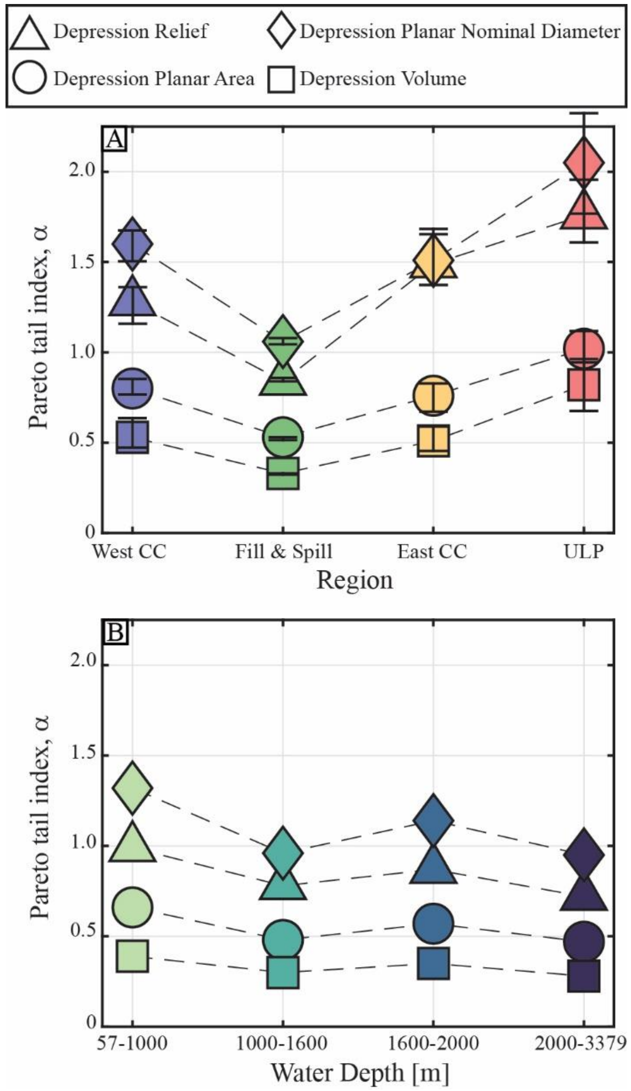

Figure 8. Power-law tail index (α) plots for all regional datasets across three depression dimensions, which include relief, nominal planar diameter, planar area, and volume. Note whiskers on error bars in subplot A represent minimum and maximum tail indexes for subregions based on either the analysis of the expanded or shrunken subregions.

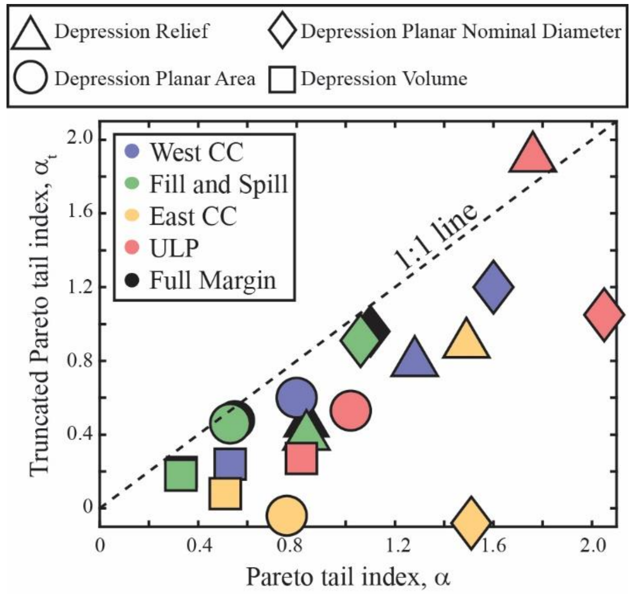

Figure 9. Plot comparing Pareto tail index and truncated Pareto tail index values for the full GoM margin dataset and four subregional datasets for depression relief, planar nominal diameter, planar area, and volume.

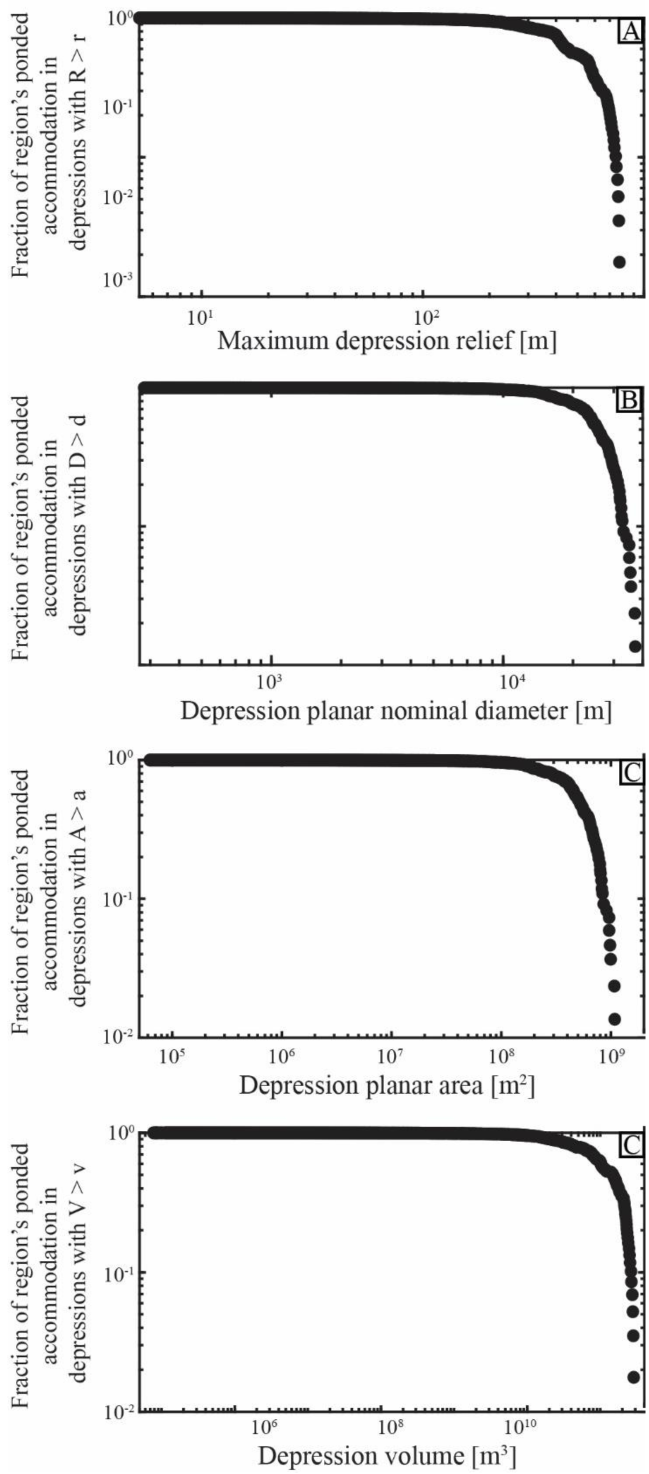

Figure 10. Dimensional plots showing fraction of region's ponded accommodation in depressions greater than a specific value for the full northern GoM dataset, where [A] is maximum depression relief, [B] is nominal planar depression length, [C] is depression planar area, and [D] is depression volume.

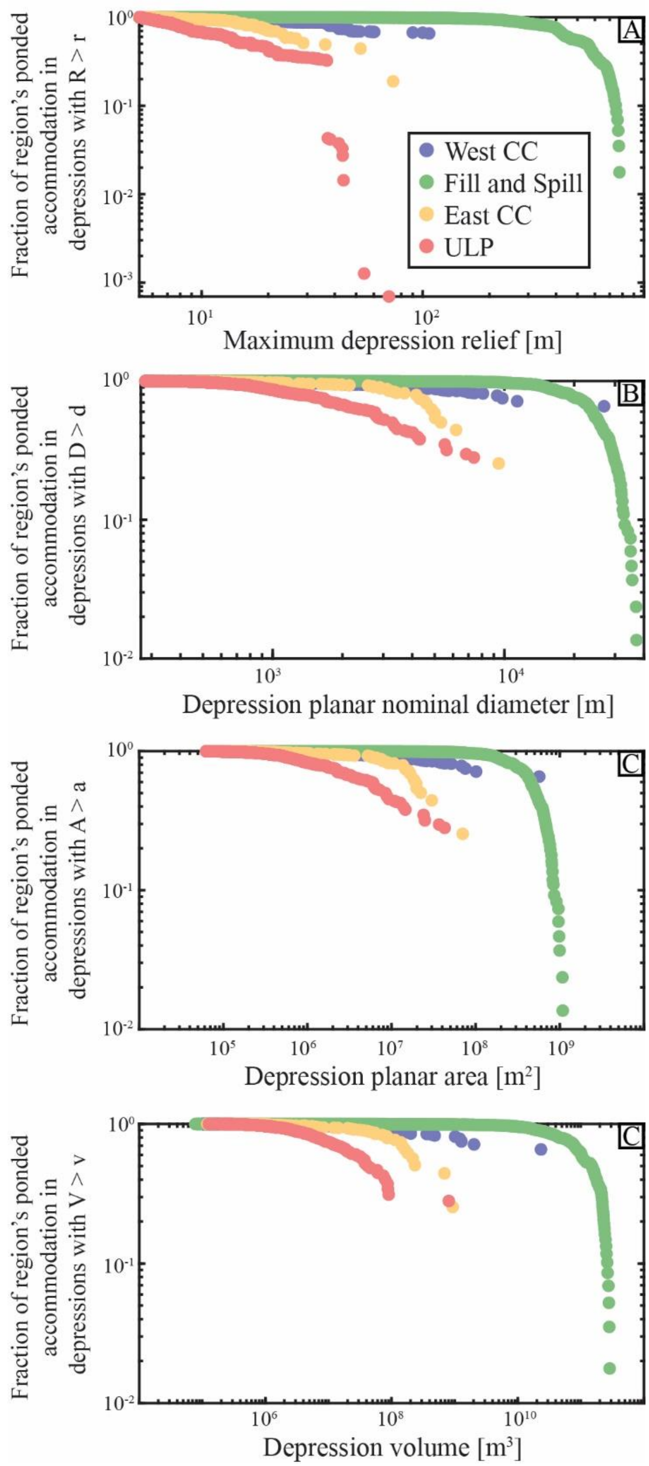

Figure 11. Dimensional plots showing fraction of region's ponded accommodation in depressions greater than a specific value for four regional datasets in study, [A] is maximum depression relief, [B] is nominal planar depression length, [C] is depression planar area, and [D] is depression volume.

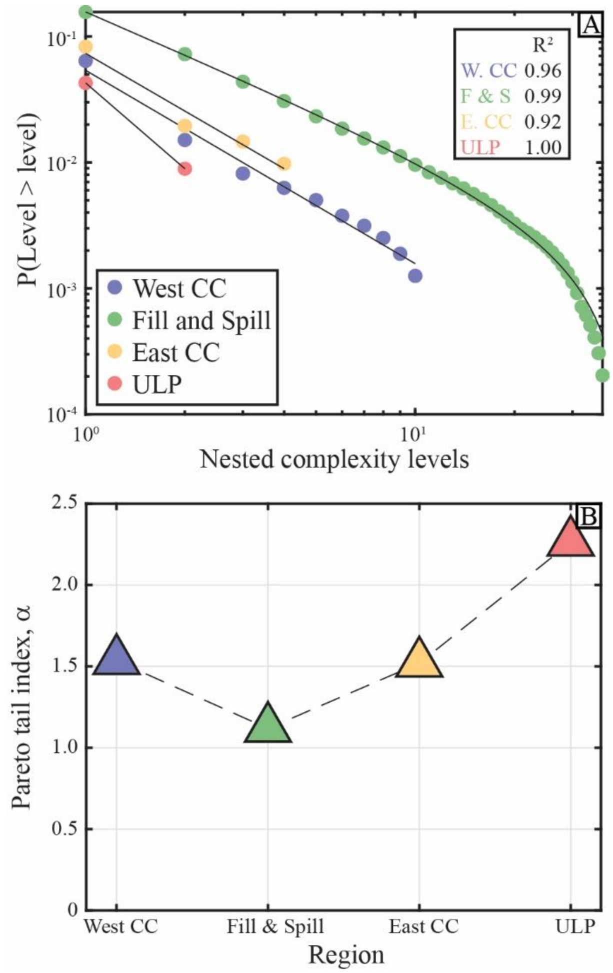

Figure 12. Plots show [A] probability of exceedance of nested depression levels and [B] tail indexes of probability of exceedance distributions for the four regions in the study.

	A	V	D	L
α	5.49×10^{-1}	3.34×10^{-1}	8.42×10^{-1}	1.10×10^{0}
γ	1.76×10^{-1}	1.37×10^{2}	6.37×10^{0}	2.02×10^{3}
Residual	9.08×10^{-1}	9.01×10^{-1}	8.69×10^{-1}	9.08×10^{-1}
$\alpha_{truncated}$	4.78×10^{-1}	1.98×10^{-1}	4.58×10^{-1}	9.57×10^{-1}
$\gamma_{truncated}$	7.86×10^{5}	1.01×10^{6}	6.00×10^{0}	1.00×10^{3}
υ	1.10×10^{9}	2.80×10^{11}	7.71×10^{2}	3.73×10^{4}

All Regions Dataset

Table 1. Table showing estimated parameters for Pareto and truncated Pareto fits for the entire northern GoM dataset. A = Area, V = Volume, D = Depth, and L = Length. Row variables are defined in text.

	A	V	D	L	A	V	D	L	A	V	D	L	A	V	D	L
α	8.01×10^{-1}	5.30×10^{-1}	1.28×10^{0}	1.60×10^{0}	5.28×10^{-1}	3.25×10^{-1}	8.39×10^{-1}	1.06×10^{0}	7.57×10^{-1}	5.10×10^{-1}	1.49×10^{0}	1.51×10^{0}	1.02×10^{0}	8.15×10^{-1}	1.76×10^{0}	2.05×10^{0}
γ	6.78×10^{4}	2.28×10^{3}	1.20×10^{1}	8.23×10^{4}	1.31×10^{3}	1.25×10^{2}	6.95×10^{0}	1.49×10^{3}	3.96×10^{4}	1.78×10^{3}	1.67×10^{1}	4.76×10^{4}	1.34×10^{6}	1.23×10^{5}	2.03×10^{1}	1.72×10^{6}
Residual	9.71×10^{-1}	9.22×10^{-1}	8.36×10^{-1}	9.71×10^{-1}	8.93×10^{-1}	8.88×10^{-1}	8.58×10^{-1}	8.93×10^{-1}	8.20×10^{-1}	8.62×10^{-1}	9.05×10^{-1}	8.20×10^{-1}	9.23×10^{-1}	9.25×10^{-1}	9.38×10^{-1}	9.23×10^{-1}
$\alpha_{truncated}$	6.02×10^{-1}	2.44×10^{-1}	7.93×10^{-1}	1.20×10^{0}	4.57×10^{-1}	1.81×10^{-1}	3.87×10^{-1}	9.13×10^{-1}	-3.78×10^{-2}	8.00×10^{-2}	8.93×10^{-1}	-8.45×10^{-2}	5.27×10^{-1}	2.67×10^{-1}	1.90×10^{0}	1.05×10^{0}
$\gamma_{truncated}$	9.90×10^{5}	9.89×10^{5}	5.96×10^{0}	1.12×10^{3}	7.85×10^{5}	1.05×10^{6}	6.00×10^{0}	1.00×10^{3}	8.08×10^{5}	9.33×10^{5}	5.89×10^{0}	1.01×10^{3}	7.78×10^{5}	1.03×10^{6}	5.98×10^{0}	9.96×10^{2}
υ	1.00×10^{8}	2.00×10^{9}	1.00×10^{2}	1.15×10^{4}	1.10×10^{9}	2.80×10^{11}	7.71×10^{2}	3.73×10^{4}	3.10×10^{7}	6.80×10^{8}	5.30×10^{1}	6.31×10^{3}	2.80×10^{7}	8.70×10^{7}	4.40×10^{1}	5.96×10^{3}
	Normal West CC				Normal Fill and Spill				Normal East CC				Normal ULP			
α	8.59×10^{-1}	6.54×10^{-1}	1.35×10^{0}	1.72×10^{0}	5.29×10^{-1}	3.28×10^{-1}	8.50×10^{-1}	1.06×10^{0}	8.13×10^{-1}	5.59×10^{-1}	1.53×10^{0}	1.63×10^{0}	1.05×10^{0}	8.15×10^{-1}	1.76×10^{0}	2.09×10^{0}
γ	1.19×10^{5}	1.41×10^{4}	1.47×10^{1}	1.46×10^{5}	1.36×10^{3}	1.32×10^{2}	6.93×10^{0}	1.54×10^{3}	8.16×10^{4}	3.41×10^{3}	1.65×10^{1}	9.93×10^{4}	1.82×10^{6}	1.19×10^{5}	2.02×10^{1}	2.34×10^{6}
Residual	9.64×10^{-1}	9.23×10^{-1}	7.25×10^{-1}	9.64×10^{-1}	8.93×10^{-1}	8.93×10^{-1}	8.64×10^{-1}	8.93×10^{-1}	7.84×10^{-1}	8.18×10^{-1}	8.20×10^{-1}	7.84×10^{-1}	9.35×10^{-1}	9.34×10^{-1}	9.35×10^{-1}	9.35×10^{-1}
$\alpha_{truncated}$	6.08×10^{-1}	1.65×10^{-1}	3.02×10^{-1}	1.21×10^{0}	4.48×10^{-1}	1.80×10^{-1}	4.16×10^{-1}	8.95×10^{-1}	-4.12×10^{-1}	-1.37×10^{-1}	3.63×10^{-1}	-8.52×10^{-1}	5.50×10^{-1}	2.83×10^{-1}	1.89×10^{0}	1.10×10^{0}
$\gamma_{truncated}$	7.80×10^{5}	1.23×10^{6}	5.90×10^{0}	9.97×10^{2}	7.85×10^{5}	9.98×10^{5}	6.00×10^{0}	1.00×10^{3}	8.89×10^{5}	8.04×10^{5}	5.76×10^{0}	1.06×10^{3}	7.78×10^{5}	1.03×10^{6}	5.98×10^{0}	9.96×10^{2}
υ	4.70×10^{7}	2.00×10^{8}	4.80×10^{1}	7.75×10^{3}	1.10×10^{9}	2.80×10^{11}	7.71×10^{2}	3.72×10^{4}	1.70×10^{7}	1.70×10^{8}	2.90×10^{1}	4.71×10^{3}	2.80×10^{7}	8.70×10^{7}	4.40×10^{1}	5.97×10^{3}
	Shrink West CC				Expand Fill and Spill				Shrink East CC				Shrink ULP			
α	7.74×10^{-1}	4.93×10^{-1}	1.15×10^{0}	1.55×10^{0}	5.47×10^{-1}	3.37×10^{-1}	8.69×10^{-1}	1.09×10^{0}	6.57×10^{-1}	4.24×10^{-1}	1.24×10^{0}	1.31×10^{0}	8.71×10^{-1}	5.26×10^{-1}	1.20×10^{0}	1.74×10^{0}
γ	3.61×10^{4}	1.37×10^{3}	1.19×10^{1}	4.35×10^{4}	1.72×10^{3}	1.52×10^{2}	7.52×10^{0}	1.96×10^{3}	9.37×10^{3}	5.02×10^{2}	1.11×10^{1}	1.10×10^{4}	1.71×10^{5}	1.97×10^{3}	8.18×10^{0}	2.12×10^{5}
Residual	9.95×10^{-1}	9.61×10^{-1}	8.56×10^{-1}	9.95×10^{-1}	9.02×10^{-1}	8.89×10^{-1}	8.38×10^{-1}	9.02×10^{-1}	9.19×10^{-1}	9.36×10^{-1}	9.21×10^{-1}	9.19×10^{-1}	9.55×10^{-1}	9.78×10^{-1}	9.50×10^{-1}	9.55×10^{-1}
$\alpha_{truncated}$	7.54×10^{-1}	3.24×10^{-1}	7.11×10^{-1}	1.51×10^{0}	4.69×10^{-1}	1.84×10^{-1}	3.62×10^{-1}	9.37×10^{-1}	2.79×10^{-1}	1.59×10^{-1}	7.64×10^{-1}	5.56×10^{-1}	6.09×10^{-1}	3.60×10^{-1}	1.21×10^{0}	1.22×10^{0}
$\gamma_{truncated}$	7.90×10^{5}	9.93×10^{5}	5.98×10^{0}	1.00×10^{3}	7.85×10^{5}	1.05×10^{6}	5.99×10^{0}	1.00×10^{3}	7.76×10^{5}	1.00×10^{6}	5.93×10^{0}	9.94×10^{2}	7.81×10^{5}	1.04×10^{6}	5.98×10^{0}	9.98×10^{2}
υ	8.40×10^{8}	2.30×10^{11}	5.86×10^{2}	3.27×10^{4}	1.10×10^{9}	2.20×10^{11}	5.77×10^{2}	3.72×10^{4}	1.20×10^{8}	3.50×10^{9}	9.60×10^{1}	1.23×10^{4}	1.80×10^{8}	1.90×10^{10}	2.08×10^{2}	1.51×10^{4}
	Expand West CC				Shrink Fill and Spill				Expand East CC				Expand ULP			
α	6.59×10^{-1}	3.90×10^{-1}	9.95×10^{-1}	1.32×10^{0}	4.80×10^{-1}	2.98×10^{-1}	7.78×10^{-1}	9.60×10^{-1}	5.68×10^{-1}	3.49×10^{-1}	8.72×10^{-1}	1.14×10^{0}	4.73×10^{-1}	2.82×10^{-1}	7.22×10^{-1}	9.47×10^{-1}
γ	8.30×10^{3}	3.18×10^{2}	1.01×10^{1}	9.70×10^{3}	6.99×10^{2}	8.79×10^{1}	6.40×10^{0}	7.85×10^{2}	2.45×10^{3}	1.90×10^{2}	7.40×10^{0}	2.80×10^{3}	6.27×10^{2}	5.96×10^{1}	4.28×10^{0}	7.03×10^{2}
Residual	8.70×10^{-1}	8.70×10^{-1}	8.30×10^{-1}	8.70×10^{-1}	8.60×10^{-1}	8.60×10^{-1}	8.30×10^{-1}	8.60×10^{-1}	8.80×10^{-1}	8.80×10^{-1}	8.50×10^{-1}	8.80×10^{-1}	8.60×10^{-1}	8.30×10^{-1}	8.00×10^{-1}	8.60×10^{-1}
$\alpha_{truncated}$	4.81×10^{-1}	5.68×10^{-2}	3.99×10^{-1}	9.62×10^{-1}	3.69×10^{-1}	1.37×10^{-1}	2.86×10^{-1}	7.37×10^{-1}	4.19×10^{-1}	1.65×10^{-1}	3.63×10^{-1}	8.38×10^{-1}	3.77×10^{-1}	1.64×10^{-1}	4.14×10^{-1}	7.54×10^{-1}
$\gamma_{truncated}$	7.86×10^{5}	1.64×10^{5}	5.99×10^{0}	1.00×10^{3}	7.85×10^{5}	9.96×10^{5}	5.99×10^{0}	1.00×10^{3}	7.84×10^{5}	1.07×10^{6}	5.99×10^{0}	1.00×10^{3}	7.84×10^{5}	1.04×10^{6}	5.99×10^{0}	1.00×10^{3}
υ	1.70×10^{8}	2.80×10^{10}	3.93×10^{2}	1.47×10^{4}	9.60×10^{8}	2.80×10^{11}	7.71×10^{2}	3.50×10^{4}	5.10×10^{8}	1.00×10^{11}	5.15×10^{2}	2.55×10^{4}	1.10×10^{9}	2.20×10^{11}	5.77×10^{2}	3.72×10^{4}
	Water Depth = 57 to 1000 m				Water Depth = 1001 to 1600 m				Water Depth = 1601 to 2000 m				Water Depth = 2001 to 3379 m			

Table 2. Table showing estimated parameters for Pareto and truncated Pareto fits across normal, expanded, and shrunken sized subregions, as well as four water depth ranges, for the entire northern GoM dataset. A = Area, V = Volume, D = Depth, and L = Length. Row variables are defined in text.

AUTHOR CONTRIBUTIONS

J.K.R. and K.M.S. conceived the initial idea of the study. J.K.R. collected all data. Both authors contributed to the data analysis and interpretations. J.K.R. wrote the initial draft of the manuscript with edits provided by K.M.S..

LIST OF REFERENCES

Aban, I., M. Meerschaert, and A. Panorska (2006). Parameter estimation of the trucated Pareto distribution, *Journal of the American Statistical Association*, **101**(473), 270-277.

Alexander, J., and S. Morris (1994). Observations on experimental, nonchannelized, high-concentration turbidity currents and variations in deposits around obstacles, *Journal of Sedimentary Research*, **64**(4a), 899-909.

Andrews, D. (1960). The Louann Salt and its relationship to Gulf Coast salt domes, *Gulf Coast Association of Geological Societies Transactions*, **10**(1), 215-240.

Ashby, W. (1947). Principles of the self-organizing dynamic system, *Journal of General Psychology*, **37**(2), 125-128.

Badalini, G., B. Kneller, and C. Winker (2000). Architecture and Processes in the Late Pleistocene Brazos-Trinity Turbidite System, Gulf of Mexico Continental Slope, *GCSSEPM, 20th Annual Research Conference Deep-Water Reservoirs of the World*, 16-34.

Bak, P., and C. Tang (1989). Earthquakes as a self-organized critical phenomenon, *Journal of Geophysical Research: Solid Earth*, **94**(B11), 15635-15637.

Bird, D., K. Burke, S. Hall, and J. Casey (2005). Gulf of Mexico tectonic history: Hotspot tracks, crustal boundaries, and early salt distribution, *AAPG bulletin*, **89**(3), 311-328.

Blum, M., and H. Roberts (2009). Drowning of the Mississippi Delta due to insufficient sediment supply and global sea-level rise, *Nature Geoscience*, **2**(1), 488-491.

BOEM. Northern GoM Deepwater Bathymetry Grid from 3D Seismic [Data file]. Retrieved from https://www.boem.gov/oil-gas-energy/mapping-and-data/map-gallery/northern-gom-deepwater-bathymetry-grid-3d-seismic. (2017).

Callot, J., J. Salel, J. Letouzey, J. Daniel, and J. Ringenbach (2016). Three-dimensional evolution of salt-controlled minibasins: Interactions, folding, and megaflap development, *AAPG Bulletin*, **100**(9), 1419-1442.

Church, M. (2006). Bed material transport and the morphology of alluvial river channels, *Annual Reviews of Earth and Planetary Sciences*, **34**(1), 325-354.

Clauset, A., C. Shalizi, and M. Newman (2009). Power-law distributions in empirical data, SIAM Review, **51**(4), 661-703.

Colling, E., R. Alexander, and R. Phair (2001). Regional mapping and maturity modeling for the northern deep water Gulf of Mexico, in *Petroleum Systems of Deep-Water Basins-Global and Gulf of Mexico Experience*, edited by R.H. Fillon, N.C. Rosen, P. Weimer, A. Lowrie, H. Pettingill, R.L. Phair, H.H. Roberts, H.H. van Hoom, **21**(1), 87-110.

Deluca, A., and Á. Corral (2013). Fitting and goodness-of-fit test of non-truncated and truncated power-law distributions, *Acta Geophysica*, **61**(1), 1351-1394.

Dorrell, R., M. Patacci, and W. McCaffrey (2018). Inflation of Ponded, Particulate Laden Density Currents, *Journal of Sedimentary Research*, **88**(11), 1276-1282.

Eddy, D., H. Van Avendonk, G. Christeson, I. Norton, G. Karner, C. Johnson, and J. Snedden (2014). Deep crustal structure of the northeastern Gulf of Mexico: Implications for rift evolution and seafloor spreading, *Journal of Geophysical Research: Solid Earth*, **119**(9), 6802-6822.

Eddy, D., H. Van Avendonk, G. Christeson, and I. Norton (2018). Structure and origin of the rifted margin of the northern Gulf of Mexico. *Geosphere*, **14**(4), 1804-1817.

Ewing, T. (2009). The ups and downs of the Sabine Uplift and the northern Gulf of Mexico Basin: Jurassic basement blocks, Cretaceous thermal uplifts, and Cenozoic flexure, *Gulf Coast Association of Geological Societies Transactions*, **59**(1), 253-269.

Fernandez, N., M. Hudec, C. Jackson, T. Dooley, and O. Duffy (2020). The competition for salt and kinematic interactions between minibasins during density-driven subsidence: observations from numerical models, *Petroleum Geoscience*, **26**(1), 3-15.

Gabaix, X., P. Gopikrishnan, V. Plerou, and H. Stanley (2003). A theory of power-law distributions in financial market fluctuations, *Nature*, **423**(6937), 267-270.

Galloway, W. (2008). Depositional Evolution of the Gulf of Mexico Sedimentary Basin. In K. J. Hsü, A. D. Miall (Eds.), *Sedimentary Basins of the World*: *The Sedimentary Basins of the United States and Canada*, **5**(1), 505-549. The Netherlands: Elsevier.

Galy, V., C. France-Lanord, O. Beyssac, P. Faure, H. Kudrass, and F. Palhol (2007). Efficient organic carbon burial in the Bengal fan sustained by the Himalayan erosional system, *Nature*, **450**(7168), 407-410.

Ganti, V., K. Straub, E. Foufoula-Georgiou, and C. Paola (2011). Space-time dynamics of depositional systems: Experimental evidence and theoretical modeling of heavy-tailed statistics, *Journal of Geophysical Research: Earth Surface*, **116**(F2), F02011.

Ge, Z., R. Gawthorpe, L. Zijerveld, and A. Oluboyo (2019). Controls on variations in minibasin geometries: Lower Congo Basin, offshore Angola, *EarthArXiv Preprint*, id. KX3UY.

Gemmer, L., S. Ings, S. Medvedev, and C. Beaumont (2004). Salt tectonics driven by differential sediment loading: Stability analysis and finite-element experiments, *Basin Research*, **16**(2), 199-218.

Gilbert, G. and J. Powell (Ed). (1880). *Report on the Geology of the Henry Mountains*, Washington, D.C.: US Government Printing Office, **2**(1), 1-170.

Hallet, B. (1990). Spatial self-organization in geomorphology: from periodic bedforms and patterned ground to scale-invariant topography, *Earth Science Reviews*, **29**(1-4), 57-75.

Hudec, M., and M. Jackson (2007). Terra infirma: Understanding salt tectonics, *Earth Science Reviews*, **82**(1-2), 1-28.

Hudec, M., M. Jackson, and F. Peel (2013a). Influence of deep Louann structure on the evolution of the northern Gulf of Mexico, *AAPG Bulletin*, **97**(10), 1711-1735.

Hudec, M., M. Jackson, and D. Schultz-Ela (2009). The paradox of minibasin subsidence into salt: Clues to the evolution of crustal basins, *Geological Society of America Bulletin*, **121**(1-2), 201-221.

Hudec, M., I. Norton, M. Jackson, and F. Peel (2013b). Jurassic evolution of the Gulf of Mexico salt basin, *AAPG Bulletin*, **97**(10), 1683-1710.

Humphris Jr., C. (1979). Salt movement on continental slope, northern Gulf of Mexico, *AAPG Bulletin*, **63**(5), 782-798.

Ings, S., and C. Beaumont (2010). Shortening viscous pressure ridges, a solution to the enigma of initiating salt ‘withdrawal’minibasins, *Geology*, **38**(4), 339-342.

Jackson, M., R. Cornelius, C. Craig, A. Gansser, J. Stöcklin, and C. Talbot (1990). Salt diapirs of the Great Kavir, central Iran, *GSA Memoirs*, **177**(1). Boulder, CO: Geological Society of America.

Jackson, M., and C. Cramez (1989). Seismic recognition of salt welds in salt tectonics regimes, *GCSSEPM 10th Annual Research Conference*, 66-71.

Jackson, M. and S. Seni (1983). Geometry and evolution of salt structures in a marginal rift basin of the Gulf of Mexico, east Texas, *Geology*, **11**(3), 131–135.

Jackson, M., and C. Talbot (1989). Salt Canopies, *GCSSEPM 10th Annual Research Conference*, 72-78.

Jerolmack, D., and D. Mohrig (2005). Interactions between bed forms: Topography, turbulence, and transport, *Journal of Geophysical Research: Earth Surface*, **110**(F2).

Jervey, M. (1988). Quantitative geological modeling of siliciclastic rock sequences and their seismic expression. In C. Wilgus, B. Hastings, C. Kendall, H. Posamentier, C. Ross and J. Van Wagoner (Eds), *Sea Level Changes – An Integrated Approach, Special Publication*, **42**(1). 47-69. Society of Economic Paleontologists and Mineralogists.

Kagan, Y. (2010). Earthquake size distribution: Power-law with exponent $\beta \equiv 1/2$?, *Tectonophysics*, **490**(1-2), 103-114.

Kane, I., M. Clare, E. Miramontes, R. Wogelius, J. Rothwell, P. Garreau, and F. Pohl (2020). Seafloor microplastic hotspots controlled by deep-sea circulation, *Science*, **368**(6495), 1140-1145.

Kneller, B., and C. Buckee (2000). The structure and fluid mechanics of turbidity currents: a review of some recent studies and their geological implications, *Sedimentology*, **47**(1), 62-94.

Kneller, B., M. Dykstra, L. Fairweather, and J. Milana (2016). Mass-transport and slope accommodation: Implications for turbidite sandstone reservoirs, *AAPG Bulletin*, **100**(2), 213-235.

Kolla, V., A. Bandyopadhyay, P. Gupta, B. Mukherjee, and D. Ramana (2012). Morphology and internal structure of a recent upper Bengal Fan-valley complex, in B. Prather, M. Deptuck, D. Mohrig, B. Van Hoorn, and R. Wynn (Eds.), *Application of the Principles of Seismic Geomorphology to Continental-Slope and Base-of-Slope Systems: Case Studies from Seafloor and Near-Seafloor Analogues*: SEPM, Special Publication **99**, 347–369.

Kolmogorov, A., and A. Bharucha-Reid (2018). *Foundations of the theory of probability: Second English Edition*. 1-86. Mineola, NY: Dover Publications, Inc.

Lamb, M., T. Hickson, J. Marr, B. Sheets, C. Paola, and G. Parker (2004). Surging versus continuous turbidity currents: flow dynamics and deposits in an experimental intraslope minibasin, *Journal of Sedimentary Research*, **74**(1), 148-155.

Lamb, M., H. Toniolo, and G. Parker (2006). Trapping of sustained turbidity currents by intraslope minibasins, *Sedimentology*, **53**(1), 147-160.

Mackin, J. (1948). Concept of the Graded River, *Geological Society of America Bulletin*, **59**(1), 463-512.

Mark, D. (1987). Network models in geomorphology. In M. G. Anderson (Ed.), *Modelling Geomorphological Systems*, New York: John Wiley and Sons, 73-97.

Martinez, J. (1991). Salt Domes: Underground mountains of salt near the U.S. Gulf Coast are a valuable resource, not only for the salt itself but also for other minerals and storage reservoirs, *American Scientist*, **79**(5), 420-431.

Marković, D., and C. Gros (2014). Power laws and self-organized criticality in theory and nature, *Physics Reports*, **536**(2), 41-74.

Masson, D., V. Huvenne, H. De Stigter, G. Wolff, K. Kiriakoulakis, R. Arzola, and S. Blackbird (2010). Efficient burial of carbon in a submarine canyon, *Geology*, **38**(9), 831-834.

Mattson, A., M. Gani, T. Roesler, N. Gani, and J. Ford (2020). 3D mapping of intruding salt bodies in the subsurface of the Gulf of Mexico using 3D seismic data, *Results in Geophysical Sciences*, **1**(1), 100004.

McElroy, B., and D. Mohrig (2009). Nature of deformation of sandy bed forms, *Journal of Geophysical Research: Earth Surface*, **114**(F3).

Milliman, J., and J. Syvitski (1992). Geomorphic/tectonic control of sediment discharge to the ocean: the importance of small mountainous rivers, *The Journal of Geology*, **100**(5), 525-544.

Mohrig, D., and J. Buttles (2007). Deep turbidity currents in shallow channels, *Geology*, **35**(2), 155-158.

Mosher, D., D. Campbell, J. Gardner, D. Piper, J. Chaytor, and M. Rebesco (2017). The role of deep-water sedimentary processes in shaping a continental margin: the Northwest Atlantic, *Marine Geology*, **393**(1), 245-259.

Muto, T., and R. Steel (2000). The accommodation concept in sequence stratigraphy: some dimensional problems and possible redefinition, *Sedimentary Geology*, **130**(1-2), 1-10.

Naden, P. (1987). Modelling gravel-bed topography from sediment transport, *Earth Surface Processes and Landforms*, **12**(4), 353-367.

Nasr-Azadani, M., and E. Meiburg (2014). Turbidity currents interacting with three-dimensional seafloor topography, *Journal of Fluid Mechanics*, **745**(1), 409-443.

Newman, M. (2005). Power laws, Pareto distributions and Zipf's law, *Contemporary Physics*, **46**(5), 323-351.

Oshaghi, M., H. Afshin, and B. Firoozabadi (2013). Experimental investigation of the effect of obstacles on the behavior of turbidity currents, *Canadian Journal of Civil Engineering*, **40**(4), 343-352.

Patacci, M., P. Haughton, and W. Mccaffrey (2015). Flow behavior of ponded turbidity currents, *Journal of Sedimentary Research*, **85**(8), 885-902.

Peel, F. (2014). How do salt withdrawal minibasins form? Insights from forward modelling, and implications for hydrocarbon migration, *Tectonophysics*, **630**(1), 222-235.

Pettinga, L., Z. Jobe, L. Shumaker, and N. Howes (2018). Morphometric scaling relationships in submarine channel–lobe systems, *Geology*, **46**(9), 819-822.

Pindell, J., and J. Dewey (1982). Permo-Triassic reconstruction of western Pangea and the evolution of the Gulf of Mexico/Caribbean region, *Tectonics*, **1**(2), 179-211.

Pinto, C., A. Lopes, and J. Machado (2012). A review of power laws in real life phenomena, *Communications in Nonlinear Science and Numerical Simulation*, **17**(9), 3558-3578.

Pirmez, C., and J. Imran (2003). Reconstruction of turbidity currents in Amazon Channel, *Marine and Petroleum Geology*, **20**(1), 823-849.

Planchon, O., and F. Darboux (2002). A fast, simple and versatile algorithm to fill the depressions of digital elevation models, *Catena*, **46**(2-3), 159-176.

Prather, B. (2003). Controls on reservoir distribution, architecture and stratigraphic trapping in slope settings, *Marine and Petroleum Geology*, **20**(6-8), 529-545.

Prather, B., J. Booth, G. Steffens, and P. Craig (1998). Classification, lithologic calibration, and stratigraphic succession of seismic facies of intraslope basins, deep-water Gulf of Mexico, *AAPG Bulletin*, **82**(5), 701-728.

Pratson, L., and W. Haxby (1996). What is the slope of the U.S. continental slope?, *Geology*, **24**(1), 3-6.

Pratson, L., C. Nittrouer, P. Wiberg, M. Steckler, J. Swenson, et al. (2009). Seascape evolution on clastic continental shelves and slopes. In C. Nittrouer, J. Austin, M. Field, J. Kravitz, J. Syvitski, P. Wiberg (Eds.), *Continental Margin Sedimentation: From Sediment Transport to Sequence Stratigraphy*, 339–73. Malden, MA: Blackwell.

Pyles, D., J. Syvitski, and R. Slatt (2011). Defining the concept of stratigraphic grade and applying it to stratal (reservoir) architecture and evolution of the slope-to-basin profile: An outcrop perspective, *Marine and Petroleum Geology*, **28**(3), 675-697.

Rowan, M. (2022). The ocean-continent transition of late synrift salt basins: extension and evaporite deposition in the southern Gulf of Mexico and global analogs. In C. Koeberl, P. Claeys, and A. Montanari (Eds.), *From the Guajira Desert to the Apennines, and from Mediterranean Microplates to the Mexican Killer Asteroid: Honoring the Career of Walter Alvarez*, **557**(1), 1- 28, Geological Society of America Special Paper.

Salvador, A. (1991). Origin and development of the Gulf of Mexico Basin, in A. Salvador (Ed.), *The Gulf of Mexico Basin, Volume J: The Geology of North America*. 131-180. Boulder, CO: Geological Society of America.

Schultz-Ela, D., M. Jackson, and B. Vendeville (1993). Mechanics of active salt diapirism, *Tectonophysics*, **228**(3-4), 275-312.

Simpson, G., and F. Schlunegger (2003). Topographic evolution and morphology of surfaces evolving in response to coupled fluvial and hillslope sediment transport, *Journal of Geophysical Research: Solid Earth*, **108**(B6).

Slowey, N., W. Bryant, D. Bean, A. Young, and S. Gartner (2003). Sedimentation in the Vicinity of the Sigsbee Escarpment during the Last 25,000 yrs. Paper presented at *Offshore Technology Conference, OTC*. Houston, TX.

Smith, J., and S. McLean (1977). Boundary layer adjustments to bottom topography and suspended sediment. In J. Nihoul (Ed.), *Elsevier Oceanography Series*, **19**(1), 123-151, Elsevier.

Smith, R. (2004). Silled sub-basins to connected tortous corridors: sediment distribution systems on topographically complex sub-aqueous slopes, in S. A. Lomas and P. Josevh (Eds.), *Confined Turbidite Systems*, 23-43. London: Geological Society.

Sornette, D. (2006). Critical Phenomena in Natural Sciences: Chaos, Fractals, Selforganization and Disorder: Concepts and Tools, Second Ed., Berlin: Springer Science & Business Media.

Soutter, E., D. Bell, Z. Cumberpatch, R. Ferguson, Y. Spychala, I. Kane, and J. Eggenhuisen (2021). The Influence of Confining Topography Orientation on Experimental Turbidity Currents and Geological Implications, *Frontiers in Earth Science*, **8**(1), 540633.

Steffens, G., E. Biegert, H. Sumner, and D. Bird (2003). Quantitative bathymetric analyses of selected deepwater siliciclastic margins: receiving basin configurations for deepwater fan systems, *Marine and Petroleum Geology*, **20**(6-8), 547-561.

Stetten, E., F. Baudin, J. Reyss, P. Martinez, K. Charlier, J. Schnyder, C. Rabouille, B. Dennielou, J. Coston-Guarini, and A. Pruski (2015). Organic matter characterization and distribution in sediments of the terminal lobes of the Congo deep-sea fan: Evidence for the direct influence of the Congo River, *Marine Geology*, **369**(1), 182-195.

Sylvester, Z., A. Cantelli, and C. Pirmez (2015). Stratigraphic evolution of intraslope minibasins: Insights from surface-based model, *AAPG Bulletin*, **99**(6), 1099-1129.

Talling, P., M. Baker, E. Pope, S. Ruffell, R. Jacinto, M. Heijnen, S. Hage, S. Simmons, M. Hasenhündl, and C. Heerema (2022). Longest sediment flows yet measured show how major rivers connect efficiently to deep sea, *Nature Communications*, **13**(1), 4193.

Talling, P., S. Hage, M. Baker, T. Bianchi, R. Hilton, and K. Maier (2024). The global turbidity current pump and its implications for organic carbon cycling, *Annual Review of Marine Science*, **16**(1), 105-133.

Thorne, J., and D. Swift (1991). Sedimentation on continental margins, II: application of the regime concept, in D. Swift (Ed.), *Shelf Sands and Sandstone Bodies: Geometry, Facies and Distribution*, 33-58. Malden, MA: Blackwell Science.

Toniolo, H., M. Lamb, and G. Parker (2006a). Depositional turbidity currents in diapiric minibasins on the continental slope: formulation and theory, *Journal of Sedimentary Research*, **76**(5), 783-797.

Toniolo, H., G. Parker, and V. Voller (2007). Role of ponded turbidity currents in reservoir trap efficiency, *Journal of Hydraulic Engineering*, **133**(6), 579-595.

Toniolo, H., G. Parker, V. Voller, and R. Beaubouef (2006b). Depositional turbidity currents in diapiric minibasins on the continental slope: experiments—numerical simulation and upscaling, *Journal of Sedimentary Research*, **76**(5), 798-818.

van Andel, T., and P. Komar (1969). Ponded sediments of the Mid-Atlantic Ridge between 22 and 23 North latitude, *Geological Society of America Bulletin*, **80**(7), 1163-1190.

van Avendonk, H., G. Christeson, I. Norton, and D. Eddy (2015). Continental rifting and sediment infill in the northwestern Gulf of Mexico. *Geology*, **43**(7), 631-634.

Wells, M., and R. Dorrell (2021). Turbulence processes within turbidity currents, *Annual Review of Fluid Mechanics*, **53**(1), 59-83.

West, D. (1989). Model for salt deformation on deep margin of central Gulf of Mexico basin, *AAPG Bulletin*, **73**(12), 1472-1482.

White, E., B. Enquist, and J. Green (2008). On estimating the exponent of power-law frequency distributions, *Ecology*, **89**(4), 905-912.

Wood, D., and A. Giles (1982). Hydrocarbon Accumulation Patterns in the East Texas Salt Dome Province: The University of Texas at Austin, Bureau of Economic Geology, *Geological Circular*, 82-6, p. 36.

Worrall, D., and S. Snelson (1989). Evolution of the northern Gulf of Mexico, with emphasis on Cenozoic growth faulting and the role of salt. In A. Bally, A. Palmer (Eds), *The Geology of North America - An Overview: Geological Society of America*, **A**(1), 97-138.

Wu, Q. (2021). lidar: A Python package for delineating nested surface depressions from digital elevation data, *Journal of Open Source Software*, **6**(59), 2965.

Wu, Q., C. Lane, L. Wang, M. Vanderhoof, J. Christensen, and H. Liu (2019). Efficient delineation of nested depression hierarchy in digital elevation models for hydrological analysis using level-set method, *JAWRA Journal of the American Water Resources Association*, **55**(2), 354-368.

Wu, S., A. Bally, and C. Cramez (1990). Allochthonous salt, structure and stratigraphy of the north-eastern Gulf of Mexico. Part II: Structure, *Marine and Petroleum Geology*, **7**(4), 334-370.

Xu, J., M. Noble, and L. Rosenfeld (2004). In-situ measurements of velocity structure within turbidity currents, *Geophysical Research Letters*, **31**(9), L09311.

BIOGRAPHY

John Kevin Reece received a Bachelor of Science in Geosciences and a Bachelor of Science in Retail Management from the University of South Carolina in 2011 and 2009, respectively. In addition, he earned a Master of Science degree in Geology from the University of Louisiana at Lafayette in 2017. He currently holds a numerical modeler position for Savannah River Mission Completion (SRMC) at the Savannah River Site in Aiken, South Carolina.